Design and optimization of open truss interlaced composite structures

by

Chengqian Liao

Thesis submitted to the University of Ottawa

in partial Fulfillment of the requirements for the

M.A.Sc Degree in

Mechanical Engineering

Department of Mechanical Engineering

Faculty of Engineering

University of Ottawa

Abstract

The advantages of polymer-matrix fibre-reinforced composites (PMFRCs) over metal alloys in terms of specific stiffness and strength are well documented. However, ongoing developments in additive manufacturing processes for metals have enabled the production of parts that rival or better PMFRC parts in terms of specific properties, once the part is considered as opposed to its constituent material. Furthermore, whilst powder-based additive manufacturing processes for metal alloys are used for targeted applications with less cost constraints, wire-based processes enable more affordable production of metal parts and challenge market penetration for some PMFRC parts produced using traditional processes. Efforts were made in producing continuous fibre PMFRC open structures such as isogrid and periodic truss structures. In parallel, yarn deposition technologies were brought to market. Most available yarn deposition technologies feature layered structures where yarns extend in parallel planes. Whilst such structures are highly reminiscent of traditional textile and prepreg laminates, they stand in contrast with the geometry of additively manufactured metal parts where the material is deposited along 3D paths that maximize specific structural performance for a given set of loading cases. This thesis discusses the optimization of non-periodic open structure continuous-fibre PMFRC parts where yarns extend along 3D paths that maximize the specific structural performance of the resulting part for specific load cases. The work focuses on optimizing the geometry of dry yarn structures using steepest ascent (SA) methods and calculating structural performance of the resulting PMFRC parts using finite element analysis (FEA).

Acknowledgements

I would like to express my sincere gratitude to my thesis supervisor, Dr. Francois Robitaille for the continuous support of my M.A.Sc study and research. Also, for providing me with the opportunity to work on a very interesting and novel research topic. I sincerely appreciate his patience, motivation, enthusiasm, and immense knowledge and appreciate all his contributions of time, ideas, and funding to make my M.A.Sc experience productive and stimulating.

I also thank Professor Michel R. Labrosse for helping me solve questions from the finite element analysis, and Jason Nguyen, an intelligent undergraduate student, for helping us finish manufacturing the prototypes of composite parts. The work conducted during my master's degree was extremely productive, and the team – at the time of writing this thesis, consisting of Fabian Basaldua-Robledo, Philippe Kanz and Lionel Tapsoba – was very helpful and enjoyable to work with.

Table of Contents

Abstract ii

Acknowledgements iii

List of Figures ix

List of Tables xv

Nomenclature xvii

Chapter 1. Introduction…..... 1

1.1. PMFRC components…..... 1

1.1.1. Prepreg autoclaving…..... 2

1.1.2. Automated fibre placement…..... 3

1.1.3. Resin transfer moulding…..... 4

1.1.4. Vacuum-assisted resin transfer moulding…..... 5

1.2. Industrial motivation…..... 6

1.2.1. Topology optimization and additive manufacturing…..... 8

1.2.2. Limitations of PMFRC…..... 10

1.3. Project overview and objectives…..... 12

1.3.1. Interlacing patterns of textile reinforcements…..... 12

1.3.2. Interlacing patterns for open structures…..... 14

1.4. Chapter summary…..... 15

Chapter 2. Literature Review….....18

2.1. Introduction….....18

2.2. Additive manufacturing technologies….....19

2.2.1. Binder jetting….....19

2.2.2. Directed energy deposition….....20

2.2.3. Material extrusion….....21

2.2.4. Material jetting….....22

2.2.5. Powder bed fusion….....23

2.2.6. Sheet lamination….....24

2.2.7. Vat photopolymerization….....25

2.3. Structural optimization by additive manufacturing….....25

2.4. Structural optimization in composites…….30

2.4.1. 3D woven textile fabrics….....31

2.4.2. Lattice structures ……36

2.4.2.1. Pyramidal and grid core structures….....37

2.4.2.2. Isotruss structures……39

2.4.2.3. WrapToR truss structures….....41

2.5. Chapter Summary….....42

Chapter 3. Computational Methodology 44

3.1. Dry reinforcement and steepest ascent algorithm ….....44

3.1.1. Yarn length to determine the mass of composite parts…….....44

3.1.2. Strain energy for equilibrating the dry yarn tensile truss….....49

3.1.3. Steepest ascent method for energy minimization in dry yarn tensile trusses….54

3.1.4. Applying SA algorithm to GSE computation.....55

3.1.4.1. Interlacing patterns ….....56

3.1.4.2. Determination of initial positions for interlacing points….....58

3.1.4.3. Determination of gradients for next step….....60

3.1.4.4. Rules for SA convergence and equilibrium verification….....62

3.1.4.5. Equilibrium verification….....63

3.2. Composite structure and FEA ….....64

3.2.1. FEA on bar-elements in a 3D domain….....64

3.2.2. Stiffness relationship in local coordinates system for bar element….....65

3.2.3. Transformation from local to global coordinate system.....….67

3.2.4. Stiffness matrix assemblage and force vectors….....71

3.2.5. Boundary conditions for nodal displacements and solutions.....…73

3.2.6. Axial forces and nodal displacements transform….....74

3.3. Chapter summary….....74

Chapter 4. Case Studies….....76

4.1. Example 1: case of 1 interlacing point….....77

4.2. Example 2: case of 2 interlacing points….....81

4.2.1. Example 2, load case 1….....83

4.2.2. Example 2, load case 2….....85

4.2.3. Example 2, further optimized solution cases 3 and 4….....87

4.3. Example 3: hinge-like part….....91

4.3.1. Example 3, regular interlacing, load case 1….....92

4.3.2. Example 3, regular interlacing, load case 2….....95

4.3.3. Example 3, regular interlacing, load case 3….....97

4.3.4. Example 3, arbitrary interlacing, load case 4…….....99

4.4. Chapter summary….....104

Chapter 5. Manufacturing and Testing….....107

5.1. Experimental validation of SA algorithm….....107

5.1.1. Introduction to generating weaving patterns.....…….....107

5.1.2. MicroScribe G2 and Rhino coordinate measurement software….....109

5.1.3. Validation results….....111

5.2. Manufacture of prototypes….....111

5.2.1. First-generation prototype 1..... ....….113

5.2.2. Second-generation prototypes….....114

5.2.3. Third-generation prototypes….....117

5.3. Testing results….....118

5.4. Chapter summary….....124

Chapter 6. Conclusion and Future Work….....126

6.1. Conclusions….....126

6.2. Future works and recommendations….....127

References …….....…….128

Appendices …….....…….....147

Appendix A. Measurement data for SA experimental validations….....147

Appendix B. Load-displacement curves for bars in prototypes 2.1, 2.2….....149

List of Figures

Figure 1.1. Autoclave process schematic [9]….....3

Figure 1.2. AFP technology with thermoplastic head (a) and integrated AFP system subcomponents (b) [12, 13] ….....4

Figure 1.3. Schematic of RTM process [15, 17] …….....4

Figure 1.4. Schematic of VARTM setup with distribution media [20] …….....6

Figure 1.5. AM rocket nozzle prototype made via PBF [24] …….....7

Figure 1.6. Components featuring PMFRC parts used in a production car [8] … 8

Figure 1.7. Schematic of topology optimization [24] …….....9

Figure 1.8. Cross-section of a prototype brake lever produced by Markforged [35] 10

Figure 1.9. Composite parts with (a) 8-node 1D lattice truss structure [37, 44]), (b) isogrid truss structure [40], (c) symmetric lattice structures [43].….....11

Figure 1.10. Manufacturing techniques and textile preforms for 3D preforms [48] 12

Figure 1.11. Schematic illustrations of woven, knits and braided fabric structures [48-50] ……..13

Figure 1.12. Schematic of a simple 3 interlacing yarns featuring 1 interlacing point….15

Figure 2.1. Schematic of the binder jetting process [61] ….....20

Figure 2.2. Schematics of DED systems (a) using laser together with powder feedstock and (b) using electron beam and wire feedstock [63] .....….21

Figure 2.3. Schematic of fused deposition modelling process [57, 65] .....….21

Figure 2.4. Schematic of multi-material jetting technology [66]….....22

Figure 2.5. Schematic of common SLS/SLM system [68]….....23

Figure 2.6. Process of sheet lamination [69] .....……...24

Figure 2.7. Schematic of stereolithography process [59]……...…....25

Figure 2.8. AM parts with FCC, VC, and ECC built cellular lattice structures [72]…...26

Figure 2.9. nTopology and AFIT lattice CubeSat bus structure [23] ……...……..27

Figure 2.10. Schematic of fiber reinforced AM process [34, 73]……....28

Figure 2.11. SEM images presenting porosities (a, b) in AM metal parts [78] and void distributions (c, d) at fibre-resin interfaces [79]……...…29

Figure 2.12. Types of 3D angle interlock woven fabrics: a) orthogonal type, b) layer-to-layer type and c) through-the-thickness type [24]……..……..…31

Figure 2.13. Schematics of guide needle tufting process to reduce thread degradation [88]……..33

Figure 2.14. AFP of a 6-meter spar for an engine pylon [89]……...……...35

Figure 2.15. FRP component manufactured via ISFLIP [92]……...……..36

Figure 2.16. Composite pyramidal lattice (CPL) core structure [100]……....38

Figure 2.17. Examples and dimensions of enhanced pyramid lattice cells [101]……....38

Figure 2.18. Schematics of isoTruss structures featuring essential regions and numbers [107]……....40

Figure 2.19. Schematic view of triangular cross-section composite truss [111]…...…..42

Figure 3.1. Interlacing diagram for pre-equilibrium 3D discontinuous, incomplete dry yarn tensile truss featuring 4 yarns and 2 interlacing points…….45

Figure 3.2. Interlacing diagram for pre-equilibrium 2D continuous dry yarn tensile truss featuring 4 yarns, 1 interlacing point, and 2 boundary points……...……...47

Figure 3.3. Interlacing diagram for pre-equilibrium 2D continuous dry yarn tensile truss featuring 2 yarns and 1 interlacing point……..48

Figure 3.4. Yarn length as a function of interlacing point position for 2D continuous structure featuring 2 yarns and 1 interlacing point…….……..49

Figure 3.5. Stain energy distribution as a function of interlacing point position for 2D continuous dry yarn tensile truss when T1 = 2 T2 …….…..53

Figure 3.6. Interlacing diagram for pre-equilibrium continuous dry yarn tensile truss featuring 8 yarns and 10 interlacing points……..…57

Figure 3.7. Arbitrary interlacing positions in dry yarn tensile trusses, prior to SA GSE optimization……...…….....59

Figure 3.8. Schematic of 3D bar element in local coordinate system……...……..65

Figure 3.9. Transformation between local and global coordinate systems…….....…67

Figure 4.1. Interlacing diagram for pre-equilibrium 3D structure example 1 featuring 3 yarns and 1 interlacing point……..……..77

Figure 4.2. Displacements and force distribution in non-optimized (a) and optimized (b) trusses, example 1…….....80

Figure 4.3. Interlacing diagram for pre-equilibrium 3D structure example 2 featuring 4 yarns and 2 interlacing point2 for (a) load case 1 and (b) load case 2……..….82

Figure 4.4. Displacements and force distribution in non-optimized (a) and optimized (b) trusses, example 2……..…….84

Figure 4.5. Displacements and force distribution of 2-interlacing-point case in horizontal loads in non-optimized (a) and optimized (b) trusses…….……....86

Figure 4.6. Displacements and force distribution after optimization for case 3 (a) and case 4 (b)…….……....89

Figure 4.7. Metal AM parts 3D printed for European Space Agency……...……..91

Figure 4.8. Interlacing diagram for pre-equilibrium 3D structure example 3 featuring 7 yarns and 6 interlacing points……..……....93

Figure 4.9. Displacements and force distribution in non-optimized (a) and optimized (b) trusses, example 3…….....94

Figure 4.10. Displacements and force distribution in optimized trusses, example 3, case 2, load case 1……...……96

Figure 4.11. Interlacing diagram for pre-equilibrium 3D structure example 3 featuring 7 yarns and 6 interlacing points, load case 3……..…..97

Figure 4.12. Displacements and force distribution in optimized trusses, example 3, case 3, load case 3……...……98

Figure 4.13. Interlacing diagram for pre-equilibrium 3D structure example 3 featuring 7 yarns and 6 interlacing points, load case 4……...……...100

Figure 4.14. Displacements and force distribution in optimized trusses, example 3, case 3, load case 4……...……...…102

Figure 4.15. Displacements and force distribution in optimized trusses, example 3, case 3, load case 5……...……..104

Figure 5.1. A designed cubic volume for generating early interlacing patterns…...….108

Figure 5.2. Schematic of interlacing yarns and points information……...…...109

Figure 5.3. Diagram of MicroScribe G2 CMM device in home position……..110

Figure 5.4. Data consistency at interlacing points a and b for load case 1 (left) and load case 2 (right)…….…….112

Figure 5.5. Prototype 1 with cubic structure, post-optimization……...113

Figure 5.6. Second generation prototypes of cubic structures in pre-optimized (a) and post-optimized (b) configurations……...……..115

Figure 5.7. Prototype 2.3 with smaller cubic structure, post-optimization……...…116

Figure 5.8. Tooling frame made of steel tubes (a) and prototype 3 of the hinge-like composite part in post-optimization configuration (b)……..……....117

Figure 5.9. Compression testing setups for prototype 2.1 in pre-optimization configuration (a) and prototype 2.2 in post-optimization configuration (b)……...119

Figure 5.10. Load-displacement curves processed for tests along individuals bar-1 (a) and bar-2 (b) in post-optimized prototype 2.2 ……..…….....121

Figure 5.11. Stiffness results for individual bars in prototypes 2.1 (a) and 2.2 (b), (unit: MPa) ……..…..…….....122

Figure B.1. Load-displacement curves processed for bars 3-8 in post-optimized prototype 2.2 …….149

Figure B.2. Load-displacement curves processed for bars 1-12 in non-optimized prototype 2.1……...……..151

List of Tables

Table 3.1. Coordinates of boundary points……....57

Table 3.2. Yarn connection information……....58

Table 4.1. Pre-and post-optimization displacements and bar lengths, example 1……...79

Table 4.2. Pre-and post-optimization displacements and bar lengths, example 2, load case 1……...85

Table 4.3. Pre-and post-optimization displacements and bar lengths, example 2, load case 2……...87

Table 4.4. Pre-and post-optimization displacements and bar lengths, example 2, case 3, load case 1……..….88

Table 4.5. Pre-and post-optimization displacements and bar lengths, case 4 of example 2, load case 1……...90

Table 4.6. Pre-and post-optimization displacements and bar lengths, example 3, load case 1……...95

Table 4.7. Pre-and post-optimization displacements and bar lengths, example 3, load case 2……...…96

Table 4.8. Pre-and post-optimization displacements and bar lengths, example 3, load case 3…….....99

Table 4.9. Pre-and post-optimization displacements and bar lengths, example 3, load case 4…….103

Table 4.10. Pre-and post-optimization displacements and bar lengths, example 3, load case 5…….104

Table 5.1. Tension combinations for yarns 1-3……...….111

Table 5.2. Typical properties of carbon yarn TENAX®-J: HTS40 E13 12K 800tex....114

Table 5.3. Stiffness values for individual bars in prototypes 2.1 and 2.2……..123

Table A.1. Measure data for SA verifications 1) 5:2:2 grams unit: millimeter….....147

Table A.2. Measure data for SA verifications 2) 5:5:2 grams unit: millimeter……..148

Nomenclature

Greek letters		**Units**
Af	Final fabric angle	rad
$\Delta\delta$	Equilibrium variability	N
∇g	Gradient variability	
∂	Partial derivative	

Latin letters		**Units**
A	Area of cross section	
B	Bending stiffness	$N \cdot m^2$
cc	Cubic centimetre	cm^3
d	Displacement of rod	M
E	Elastic modulus	N/m^2
GPa	Gigapascal	N/m^2
L	Length of segment	Cm
MPa	Megapascal	N/m^2
n	Total amount of yarn segments	
P	Quasi-static uniform tension	N
U	Strain energy	

Acronyms

2D	Two dimensions
3D	Three dimensions
3DP	Three-dimensional printing
AFP	Automated fibre placement
AIWF	Angle-interlock woven fabric
CAE	Computer-aided engineering
CGS	Composite grid structures
CPL	Composite pyramidal lattice
DED	Directed energy deposition
DLP	Digital light processing
DLS	Digital light synthesis
DOF	Degree of freedom
EBF3	Electron beam free-form fabrication
EBM	Electron beam melting
EBW	Electron beam welding
ECC	Edge centre cube
FCC	Face centre cube
FDM	Fused deposition modeling
FEA	Finite element analysis
FRP	Fibre-reinforced polymer
ISFLIP	In situ forming of a liquid infused preform
LCD	Liquid crystal display
LCM	Liquid composite molding
LDM	Liquid deposition modeling
LENS	Laser engineering net-shaping
LLAIWF	Layer-to-layer angle-interlock woven fabric
LMD	Laser metal deposition
LOM	Laminated object manufacturing
MJF	Multi-Jet fusion

PDF	Powder bed fusion
PLA	Polylactic acid
PMC	Polymer matrix composite
PMFRC	Polymer matrix fibre reinforced composite
PP	Polypropylenes
PWTC	Plain-woven textile composites
RTM	Resin transfer moulding
SA	Steepest ascent
SEM	Scanning electron microscope
SL	Stereolithography
SLA	Stereolithography apparatus
SLM	Selective laser melting
SLS	Selective laser sintering
TO	Topology optimization
TPU	Thermoplastic polyurethanes
UV	Ultraviolet
VARTM	Vacuum assisted resin transfer moulding
VC	Vertex cube
WAAM	Wire arc additive manufacturing
WrapToR	Wrapped tow reinforced

Chapter 1. Introduction

The history of the use of composite materials can be traced back to ancient times where straw was combined into reinforced clay, along with reinforced concrete used for centuries in modern times [1]. To meet the needs of the aviation industry in the 1940s, glass fibre reinforced plastic was developed [2, 3]. Successively, technology developed further through the advent of carbon fibres, graphite fibres, aramid fibres, silicon carbide fibres and other more exotic high-strength and/or high modulus fibres. When these fibres are combined with synthetic polymer resins, or with other materials including carbon, ceramics, rubbers, and metallic alloy matrices such as aluminum, magnesium or titanium, a composite material with its own characteristics is obtained [4].

1.1. PMFRC components

Polymer-matrix fibre-reinforced composite (PMFRC) materials have become structural materials of choice for numerous demanding applications in many industries because of their exceptional specific mechanical properties, lighter weight, and relative ease of manufacturing, especially in smaller series. These important advantages have translated to prevalence in aerospace, where more than 50% of the structure of civilian transport aircraft structures are routinely made of PMFRCs [3-5].

Beyond mass reduction, PMFRC are also highly sought materials for moderate-temperature applications, which are now used in a wide range of fields including aerospace, watercraft, solid-fuel launch vehicles, industrial equipment, and sporting goods. The usage of thermoplastics is rapidly growing, but thermosetting polymers are still the most used matrix materials for structural applications [3-4, 6-8]. Many

manufacturing technologies can be used for producing PMFRC components. The main processes include prepreg autoclaving [9-11], automated tape placement [12-14], resin transfer moulding (RTM) [15-18] and vacuum-assisted resin transfer moulding (VARTM) [19-22]. All these processes lead to parts with shell topology: their shapes are curved but generally simple, and their thickness is always much smaller than other dimensions. Furthermore, these shells are always continuous in the sense that they typically do not feature numerous large holes at the time of moulding – any large holes in PMFRC parts are typically cut post-moulding, during final trimming operations.

1.1.1. Prepreg autoclaving

The term prepreg stands for pre-impregnated fibres. Prepreg tape consists of a sliver of continuous fibres embedded in a polymer matrix which is not fully cured. The fibres can be woven or included as non-woven unidirectional layers. Prepreg materials available in industry feature primarily thermoset resins.

Prepreg autoclaving is illustrated in Figure 1.1. When consolidated into parts, prepreg tape is accurately cut and layered onto a mould according to prescribed orientation sequences, creating a laminated structure [9]. Strategically defined fibre orientations give the components its desired properties such as rigidity and shear strength [11], along the directions required by load cases. Once prepreg is laid down on the mould, the mould and prepreg stack is bagged under a temperature-resistant bag or membrane [9] and cured under heat and pressure in a numerically controlled autoclave. The component is then cooled, demoulded, and trimmed. Autoclaving leads to parts with high volume fractions (typically 65% to 70%), high specific properties and consistency.

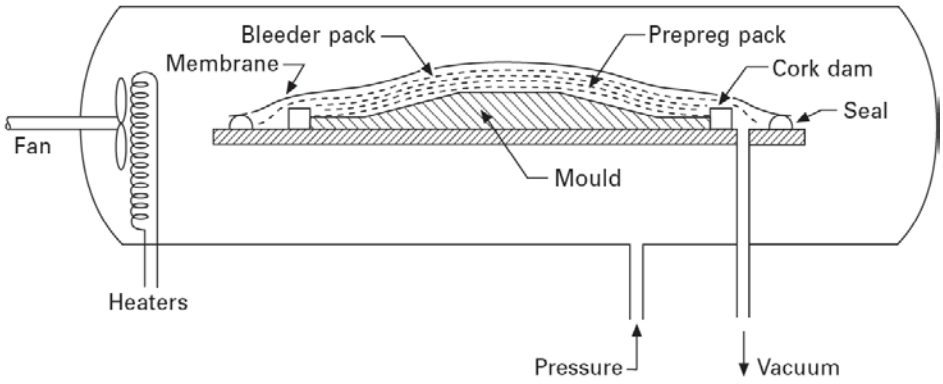

Figure 1.1. Autoclave process schematic [9]

However, limitations include high cost of materials as well as the need for specialized tools and equipment [10, 11].

1.1.2. Automated fibre placement

Automated fibre placement (AFP) is an innovative technique for manufacturing large composite structures, processing fibres layer by layer [12] using an AFP head mounted on a robotic system [13], as shown in Figure 1.2. Productivity and accuracy are significantly enhanced through programming and automation [14]. The feeding prepreg tape is heated and consolidated on the mould under compaction of a roller, all mounted on a robotic arm system. A continuous fibre-reinforced laminate of composite tape is produced, where layers can be positioned along different directions. Along with repeatable accuracy, AFP lowers labour costs, manufacturing time and material waste [13, 14].

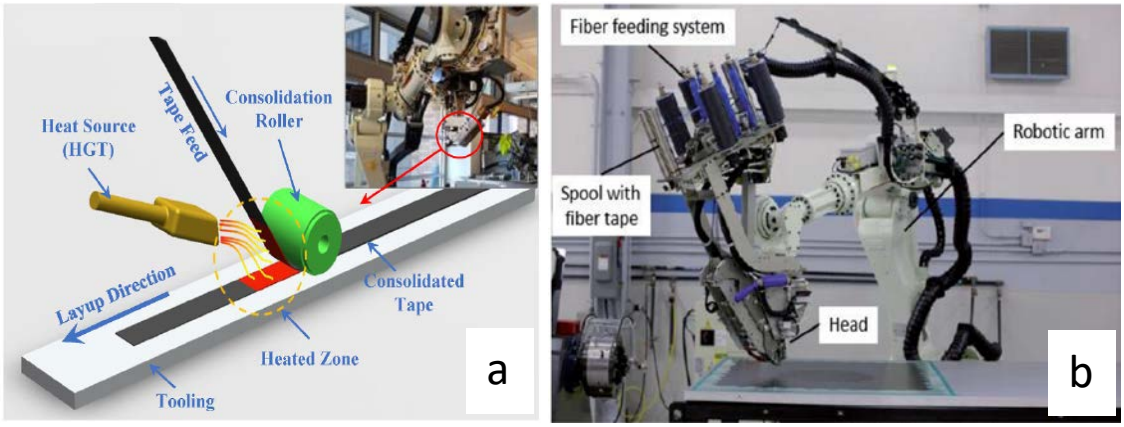

Figure 1.2. AFP technology with thermoplastic head (a) and integrated AFP system subcomponents (b) [12, 13]

1.1.3. Resin transfer moulding

Resin transfer moulding (RTM) has been widely adopted for fabricating PMFRCs due to its capability to manufacture parts with relatively high fibre volume fractions (typically 50% to 55%), sophisticated geometric features, and high-quality surface finish [15, 16], as schematically shown in Figure. 1.3.

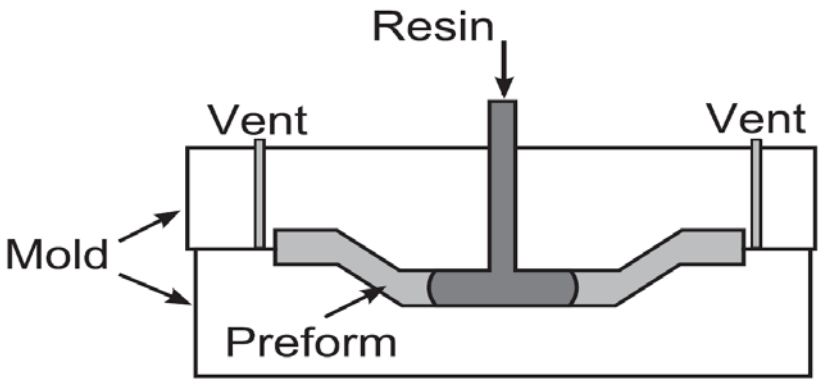

Figure 1.3. Schematic of RTM process [15, 17]

In this closed mould process, resin is pumped under pressure into a dry fibre preform that was previously positioned in the mould, and pressure is maintained throughout the polymerization process. RTM is closely affected by process variables such as injection pressure, resin properties, tooling configuration and fibre preform architecture etc. [17]. In this process, the temperature and pressure are well controlled, and productivity can be increased through automation [18]. All these characteristics guarantee PMFRC parts of consistent quality. Beyond relatively high fiber volume fractions in products, RTM also decreases material waste and achieves low air and volatile content [15, 17].

1.1.4. Vacuum-assisted resin transfer moulding

Vacuum assisted resin transfer moulding (VARTM) has become increasingly popular for manufacturing large-scale parts such as marine structures as well as semi-structural and non-structural airplane components [19, 20]. In this process, a vacuum bag covers all reinforcements, distribution media and other ancillary materials, under a vacuum-tight seal. Atmospheric pressure pushes the resin into the part the resin through inlet tubes to spread evenly into the preform [20], Figure 1.4. VARTM reduces tooling costs through its use of a sole one-sided mould while still producing high-quality composite parts, making it an attractive manufacturing process for top-side structures. As no positive pressure is applied on the resin during infusion, the pressure difference generating the gradiaent is limited to 1 atm hence infusion takes more time that in RTM.

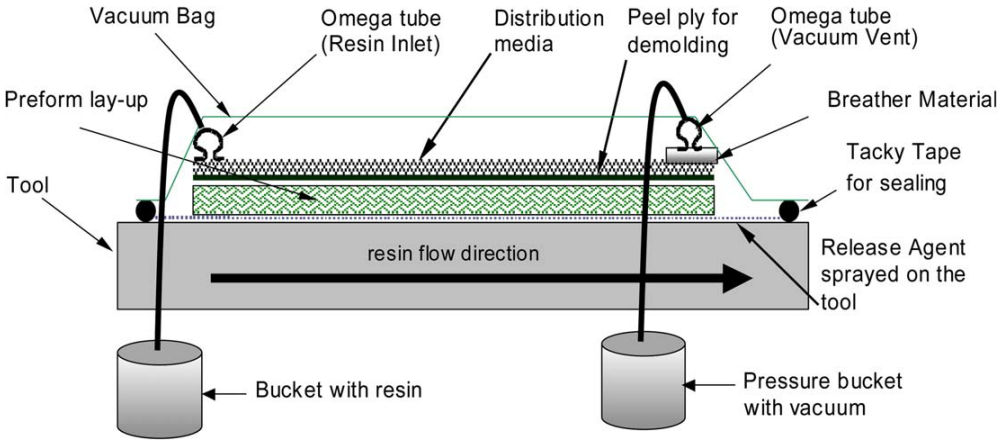

Figure 1.4. Schematic of VARTM setup with distribution media [20]

Although VARTM reduces material waste and produces laminates with reasonably good fibre volume fractions (typically 40 to 50%) [21], vacuum-driven mould filling becomes more difficult as the complexity and/or size of the part increases, or when advanced fibre preforms exhibiting low permeability are used, which can lead to dry spots requiring repair or scrapping of the PMFRC component. Therefore, much research work was devoted to flow rates and simulation of VARTM [20-22].

1.2. Industrial motivation

Additive manufacturing (AM) techniques are enabling significant technological innovations in manufacturing industries, allowing the fabrication of unique, non-moulded products [23, 24]. In AM processes, a heat source is used for combining materials in forms such as powders and solid wires, or to solidify layers of polymer layers or multi-materials [25]. The main processes for general materials include binder jetting, directed energy deposition (DED), powder bed fusion (PBF), and stereolithography (SL). For example, Figure 1.5 shows an AM prototype of rocket nozzle featuring internal

cooling channels, produced by applying successive layers of materials at selected positions on top of previously deposited layers. Complex metal alloy parts such as the nozzle can be manufactured from the application of AM techniques [24].

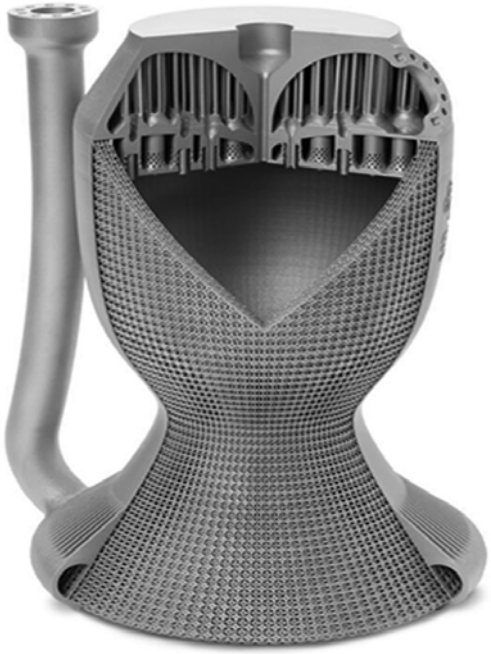

Figure 1.5. AM rocket nozzle prototype made via PBF [24]

The PMFRC manufacturing processes discussed above, namely prepreg autoclaving, automated tape placement, resin transfer moulding and vacuum-assisted resin transfer moulding are inherently additive in nature. Although these manufacturing processes can produce lightweight PMFRC laminates and parts with high stiffness, two distinctive differences compared with parts made of metallic alloys and produced using AM processes must be highlighted in discussing the aim of this work.

Firstly, the PMFRC manufacturing processes described above lead to parts that have a panel or shell geometry [26]. Their shapes can be relatively complex, but one

dimension - the thickness - is always much smaller than others defined along the main surface dimensions, as illustrated in Figure 1.6.

Secondly, these shells are always continuous due to the textile nature of the reinforcements used; mass reduction of the part through topology optimisation is not done, even as PMFRC processes inherently additive. General geometrical characteristics of PMFRC parts and metallic alloy parts produced using AM are very different, as discussed below.

Figure 1.6. Components featuring PMFRC parts used in a production car [8]

1.2.1. Topology optimization and additive manufacturing

Topology optimization (TO) refers to the mathematical application of computer-aided engineering (CAE) in which a given set of mechanical loads, boundary conditions and constraints may be applied to a design, in order to optimize the layout of material in

space, within a set envelope, to optimize load paths and the mechanical behaviour of the part [24], as illustrated in Figure 1.7. The development of topology optimization has produced innovative methods and empowered it as an effective tool for structural design, say for the design of lattice structures and porous structures [25].

Figure 1.7. Schematic of topology optimization [24]

AM technologies benefit from TO methods towards enabling the manufacturing of designs with complex geometry. The last decades have seen the parallel emergence of AM processes and parts made from polymers and, more crucially, metal alloys [23-25, 27-28]. AM processes enable the production of parts featuring geometry that cannot be made using subtractive manufacturing processes such as numerical control machining. AM technology is also increasingly relied upon in producing lightweight parts from many metallic alloys, through the application of TO in industrial AM, AM can outperform conventional machining and casting processes in numerous cases [23, 29, 30].

For complex parts, the integration of TO technologies with AM makes metal parts lightweight by avoiding unnecessary or redundant mass, along with reducing the amount of separate parts to be assembled, which reduces cost and saves material [27]. AM processes also enable economic production of trellis or lattice parts where TO leads to material being deposited only along paths of high stresses under specific load cases. These technologies lead to structures that are highly efficient on a stiffness and strength to mass basis [26, 28, 31, 32].

1.2.2. Limitations of PMFRC

Despite of the above, PMFRC parts mainly keep continuous shell geometries, TO has not happened with PMFRCs, mainly for two reasons. Firstly, the usage of continuous yarns in structural PMFRCs restricts flexibility over yarn orientations. Printed PMFRC parts typically feature layered yarns [33, 34] that might possibly be oriented optimally in 2D, but not at all in 3D along paths of higher normal stress. For example, Figure 1.8 shows the composite brake lever [35] produced by Markforged.

Figure 1.8. Cross-section of a prototype brake lever produced by Markforged [35]

The lever features two rings of concentric Kevlar fibre deposited along the contour of the structure; there is no interlacing, and the centre of the part is filled with black neat-resin Onyx matrix, most part volume features no fibres.

Established industrial PMFRC manufacturing processes do not readily enable the production of general optimized structures such as trellis or lattices. Whilst some examples of manufacturing were reported [36, 37], the resulting truss-like structures are typically defined within simple geometric envelopes and often feature a repeating basic structural unit [38-44], as illustrated in Figure 1.9. As a result, whilst PMFRCs outperform metal alloys in terms of specific material properties, in the current state of technology additively manufactured structures made from metal alloys, including large metal parts such as car subframes, trusses and others [45-47] can outperform structures made from PMFRCs, as PMFRC parts remain limited to continuous shells because of limitations to PMFRC manufacturing processes.

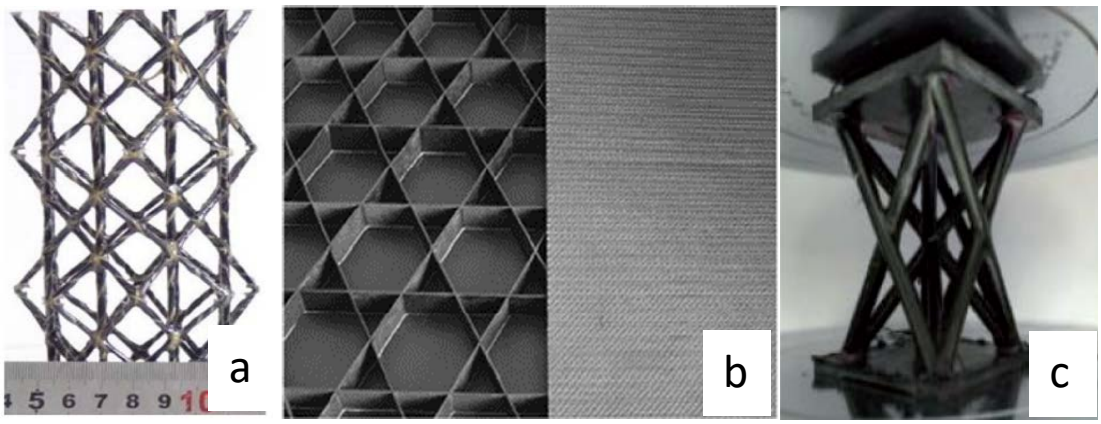

Figure 1.9. Composite parts with (a) 8-node 1D lattice truss structure [37, 44]), (b) isogrid truss structure [40], (c) symmetric lattice structures [43]

1.3. Project overview and objectives

When considering material properties only, PMFRC are often preferred for structural applications as they offer specific stiffnesses superior to those of metal alloys, largely because of their low mass. However, with AM technologies, metal alloy parts can reach superior specific structural stiffness through TO. Structural optimization applied through additive manufacturing leads to mass reduction of components through highly efficient lightweight designs [23], effectively removing mass that contributes less to structural performance. Such alloy parts can outperform PMFRC parts, the geometry of which is limited to continuous shells or panels.

1.3.1. Interlacing patterns of textile reinforcements

Within PMFRC manufacturing processes, dry reinforcement fibres and yarns are most often assembled and handled as textiles and textiles preforms, which are dry assemblies of layers of textiles uncoated with resin. Figure 1.10 shows the main manufacturing techniques for producing three-dimensional textile preforms [48] and Figure 1.11 illustrates the interlacing architectures of typical textile structures [48-50].

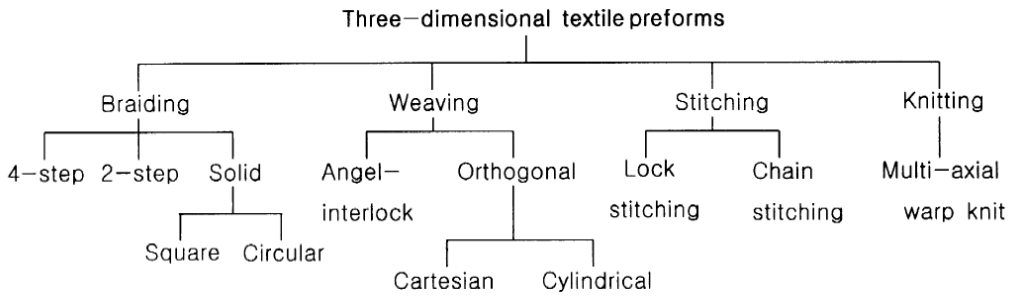

Figure 1.10. Manufacturing techniques and textile preforms for 3D preforms [48]

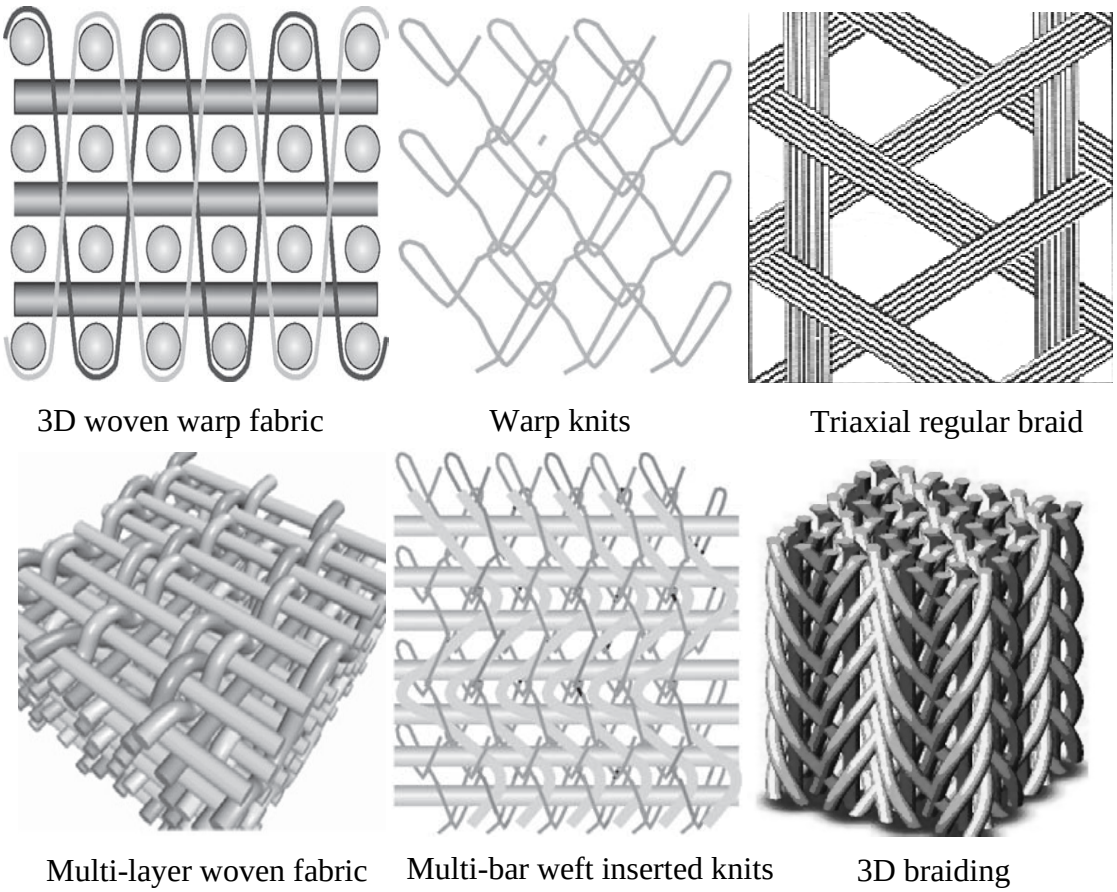

Figure 1.11. Schematic illustrations of woven, knits and braided fabric structures [48-50]

These textile structures are the reinforcements for PMFRC parts, hence the textile preforms are typically cut, tailored, and formed onto tools, to take the shape of the PMFRC parts to be made. Besides fibre and yarn characteristics, fabric structure plays a major role in defining the mechanical properties of the PMFRC final products, as tensile, bending, shear, buckling, and compression are important mechanical properties that determine structural performance [49, 51, 52].

1.3.2. Interlacing patterns for open structures

Whilst interlacing structures are fundamental to the work reported in this thesis, the structures modelled and produced are fundamentally different from the conventional textile architectures listed above. These structures, and the process devised for making them, are very novel.

The work reported in this thesis aims at bringing 3D TO to continuous yarn structural PMFRC components, as continuous yarns enable PMFRC parts offering mechanical performance far superior to those of plastic parts reinforced with short or even long fibres. The resulting trellis structures, labelled open truss interlaced composite structures, are designed by optimizing the geometry of an interlaced dry reinforcement defined in 3D through adjustments to individual yarn tensions. Figure 1.12 illustrates an interlaced model of a very simple case of such a structure. Dry reinforcement structures are made of yarns subjected to individual levels of tensions.

The single interlacing point in the simple open structure illustrated in Figure 1.12 is positioned using steepest ascent methods. Then, the resulting structure is modelled as a 3D PMFRC component subjected to external loads and boundary conditions. Composite material extending between interlacing points is modelled as beams subjected to tensile/compressive loading, and displacements at points of application of external loads are calculated using a finite element method. These displacements are minimized through a search procedure where yarn tensions are progressively adjusted, culminating in a more efficient 3D open truss interlaced PMFRC structure.

Therefore, this work studies the optimization of composite open structures via tension adjustments made on the dry reinforcement. Eventually, the process will optimize

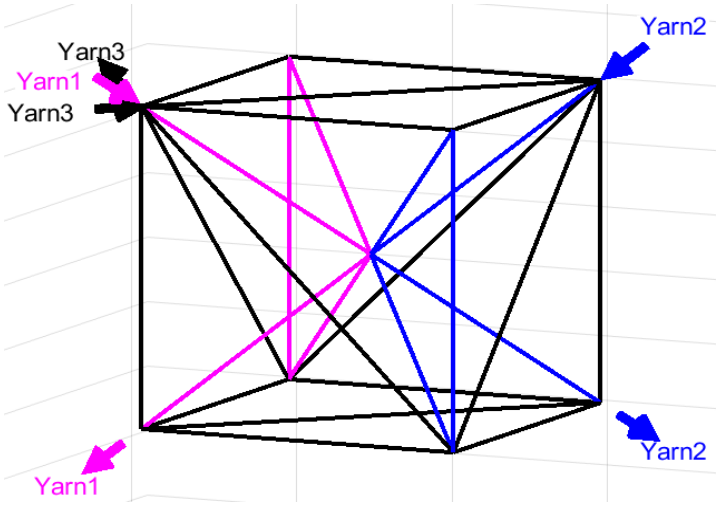

Figure 1.12. Schematic of a simple 3 interlacing yarns featuring 1 interlacing point

PMFRC structures according to different loading factors applied, improving the stiffness of the parts to reach the aim of mechanical performance optimization.

1.4. Chapter summary

Topics covered in the thesis include the introduction of the highly novel concept as well as a literature review; application of steepest ascent (SA) methods for determining the geometry of the interlaced dry yarn reinforcement and equilibrium at interlacing points; and optimization of the structural performance of the composite part through finite element simulations, to determine displacements at loading points with calculation loops for different combinations of yarn tensions. Cases are studied, and experimental production and validation is attempted. Some limitations of the work and a discussion of further steps are also featured.

The thesis consists of 6 chapters. Chapter 1 introduces a general view of PMFRC components and textile architectures, as well as the motivation for this project.

Chapter 2 is a literature review covering technology and research pertaining to optimizing the fabrication and structure of PMFRC parts, including interlacing and its mechanical behaviour. Moreover, a brief overview of additive manufacturing for metal alloys aiming at mass reduction is introduced. A contrasted review of lattice structural PMFRC parts is presented, including two different types of manufacturing approaches.

Chapter 3 summarizes the optimization methodology. In the beginning, the dry reinforcement is introduced along with the SA algorithm used for determining its structure, followed by an illustration case which shows how the locations of interlacing points are determined. Then, the FEA method employed for calculating the stiffness of the PMFRC part from the geometry of the dry reinforcement is described.

Chapter 4 presents optimization results for 3 different cases of open structures in 3D, from a simply interlaced volume with 1 interlacing point to hinge-like parts featuring complex interlacing patterns, as well as comparisons with non-optimized interlacing patterns and arbitrary structures. Optimization results are listed for different loading characteristics in terms of their respective performance.

Chapter 5 shows experimental results, starting with interlacing point positions for measuring the coincidence of interlacing point positions with computational predictions, followed by two manufacturing demonstrators of simple PMFRC parts. The composite parts were tested and compared with predictions models for performance.

Chapter 6 summarizes contributions made and lists recommendations for future work.

This work leads to a peer-reviewed conference paper: 3D open-structure continuous-fibre composite parts: yarn path optimization, presented orally at the 12th Canadian-International Conference on Composites (CANCOM 2022) on July 14th, 2022, in Fredericton, NB, Canada.

Chapter 2. Literature Review

2.1. Introduction

Light weight combined with excellent stiffness and strength have become the main drivers behind widespread selection of PMFRCs for structural applications [5, 31, 33], and for this work which targets the optimization of structural parts regarding their structural behaviour, namely stiffness. Due to low densities of structural fibres and polymer resins, PMFRC parts have become a game-changing market reality in many industries [5, 31, 33, 48, 53] where continuous shell parts such as car body panels, body-in-white, sub-frames and even complete monocoque and crash-absorbing sub-structures can be made easily and economically with PMFRCs. However, beyond thin shell parts, traditional PMFRC manufacturing faces challenges in making parts with complex 3D geometries, whist metal alloy parts produced using AM technologies show improved structural performance through TO and better structural usage of the material.

Compared with conventional methods for producing metal alloy parts, such as casting or machining, AM allows components to be printed out layer by layer [30] and enables flexibility in part geometry [54]. Many approaches to AM technology were developed. According to ISO/ASTM 52900 standard [55] and the American Society for Testing and Materials (ASTM) International Committee F42 F2792 [56], there are seven categories of AM processes, namely:

- binder jetting,
- directed energy deposition (DED),
- material extrusion,
- material jetting,

- powder bed fusion (PBF),
- sheet lamination,
- vat photopolymerization.

This chapter presents background information on additive manufacture technologies, and briefly reviews existing methods for optimizing structures for both AM industrial and PMFRCs towards advancing structural designs and mechanical performance.

2.2. Additive manufacturing technologies

AM classification can differ according to additive material type and deposition technique, as well as the processes used for fusing and solidifying the material [57-59]. Individual processes are discussed in the following sections.

2.2.1. Binder jetting

Binder jetting, also known as powder bed inkjet printing, is based on the inkjet principle [60] and was initially known as 3D printing (3DP) process. Figure 2.1 illustrates a classic binder jetting system. In this process, a liquid bonding agent is applied onto thin layers of powder by using Inkjet print heads. Once the binder is printed via the inkjet head [61], a layer of the object is consolidated through reaction between the binder and powder. By repeating the process and layering, material elements are bonded together to build the desired shape [58,61]. Post-treatment is applied to clean the component and smooth its surfaces as required.

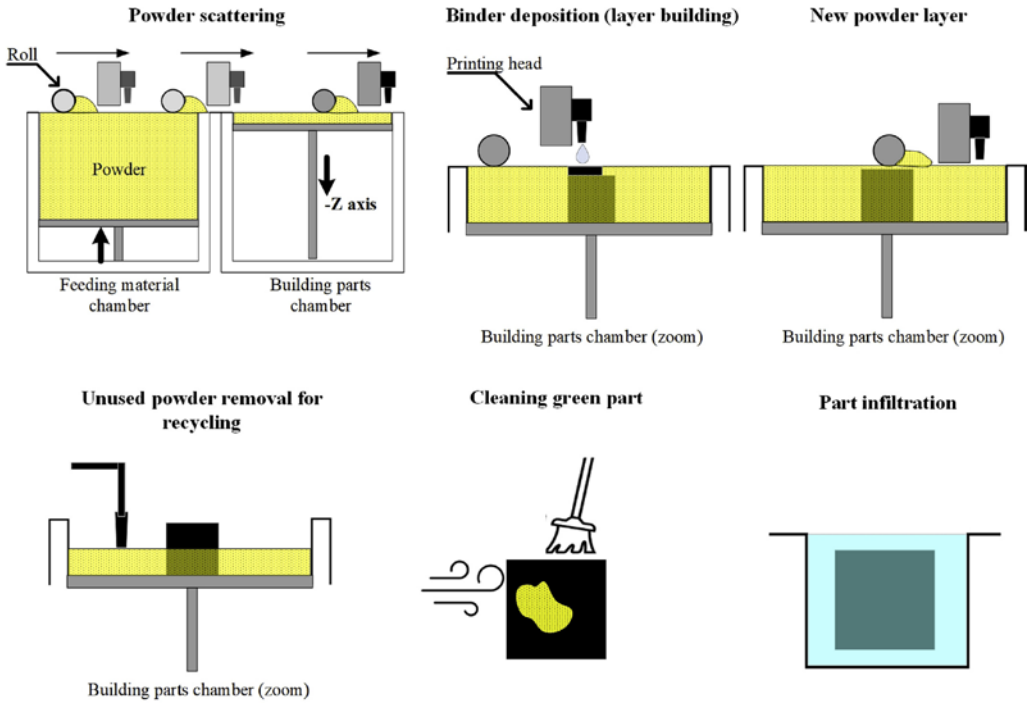

Figure 2.1. Schematic of the binder jetting process [61]

2.2.2. Directed energy deposition

DED refers to the process of using focused thermal energy to fuse materials and depositing them in the molten state [62]. Material is deposited, typically as powder molten using a laser as shown in Figure 2.2 a) or as wire feedstock molten using an electron beam as shown in Figure 2.2 b). Other sources of focused thermal energy, such as a plasma arc, can be used for melting the material being deposited [63]. DED technologies are widespread in the aerospace industry, include variants such as laser metal deposition (LMD), laser engineering net-shaping (LENS), electron beam welding (EBW), electron beam free-form fabrication (EBF3), and wire arc AM (WAAM) [60].

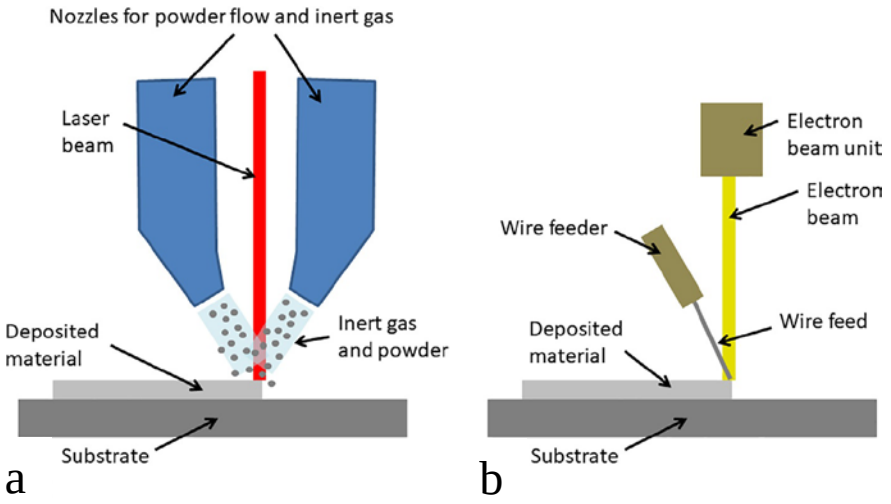

Figure 2.2. Schematics of DED systems (a) using laser together with powder feedstock and (b) using electron beam and wire feedstock [63]

2.2.3. Material extrusion

In this process, additive material is dispensed through a nozzle or orifice to build parts [64]. Fused Deposition Modeling (FDM) represents the most popular method in this category [58, 59], Figure 2.3.

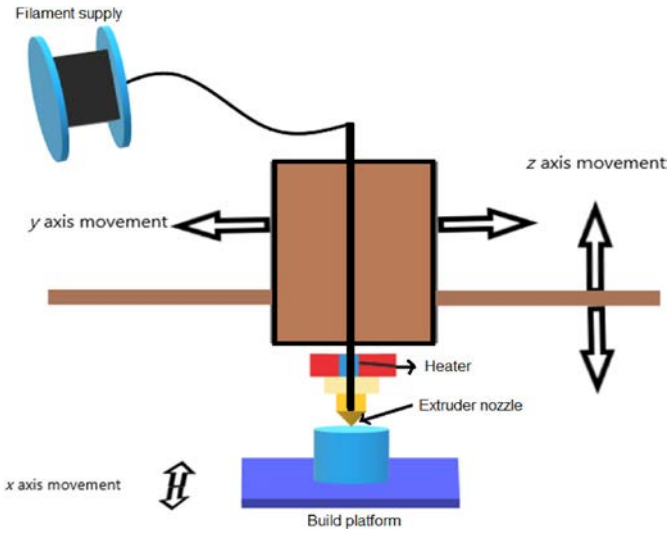

Figure 2.3. Schematic of fused deposition modelling process [57, 65]

As illustrated above, a thin layer is deposited onto a build plate. Thermoplastic polymer material is generally taken above its melting temperature and allowed to cool down suddenly after extrusion from the nozzle, on the plate or on previously layers deposited layer [65].

2.2.4. Material jetting

Material jetting, also known as PolyJet [58, 60], uses inkjet printing technology to jet liquid photopolymer droplets onto a build substrate and then cure it with ultraviolet (UV) light [66], as illustrated in Figure 2.4. This process can fabricate parts with fine features and good surface finish, while exhibiting little stair stepping effect [60], which makes it preferable for applications such as organ printing, cell bioprinting, medicine and dental fields [66, 67].

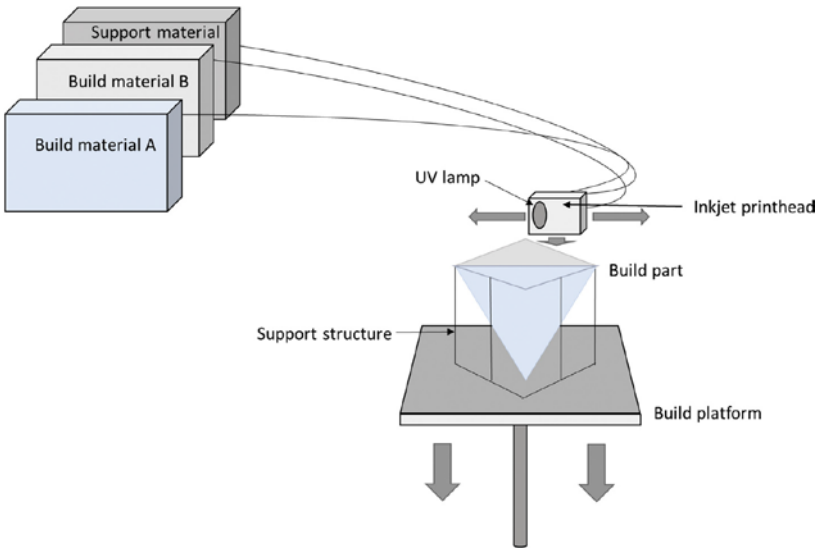

Figure 2.4. Schematic of multi-material jetting technology [66]

2.2.5. Powder bed fusion

Powder bed fusion (PDF) uses focused thermal energy to selectively fuse regions of a powder bed [58], as illustrated in Figure 2.5. Selective laser sintering (SLS), selective laser melting (SLM), electron beam melting (EBM), and Multi Jet Fusion (MJF) are the four main methods in the technology group [68]. SLS and SLM processes need thermal energy for the material to reach temperatures ensuring melting and complete fusion [60], while EBM mostly processes metallic powders with electric conductivity, in a high vacuum chamber to avoid metallic oxidation issues [59, 68]. MJF is mostly used for processing a narrow group of polyamides, polypropylenes (PP), and thermoplastic polyurethanes (TPU) [68].

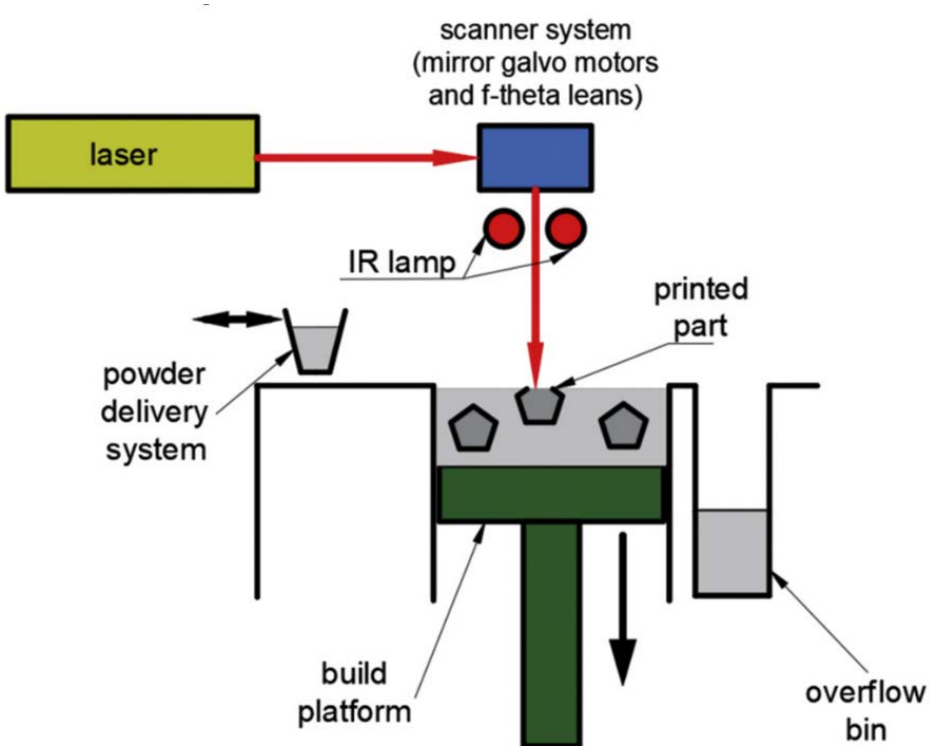

Figure 2.5. Schematic of common SLS/SLM system [68]

2.2.6. Sheet lamination

Sheet lamination, also known as laminated object manufacturing (LOM), combines additive and subtractive techniques to build layered objects [69], as illustrated in Figure 2.7. In this process, the materials come in continuous sheet form. First, a laser is used for cutting plies from material sheets. Then, these plies are bonded together through the application of pressure and heat, using a thermal adhesive coating [59]. LOM allows cheaper processing, without significant requirement of support materials, and without generating residual stresses in the parts. However, the process causes material wastage from the laser cutting [58].

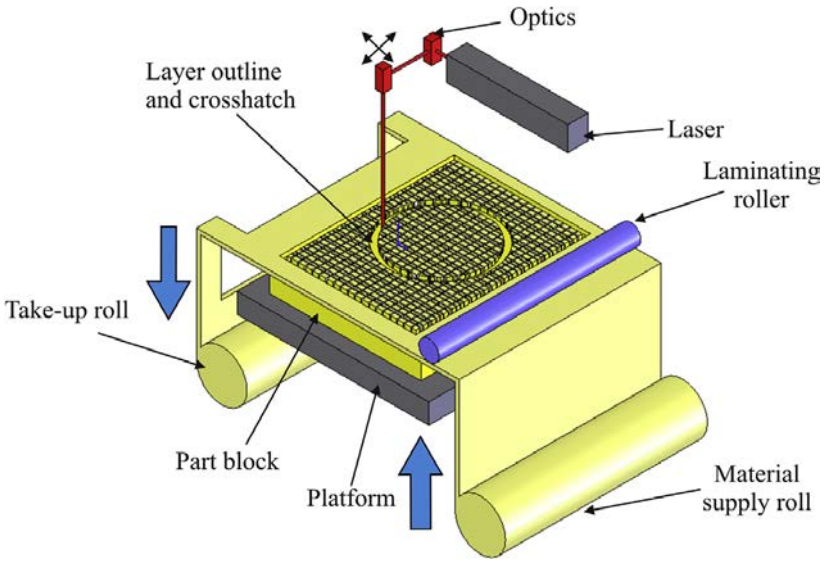

Figure 2.6. Process of sheet lamination [69]

2.2.7. Vat photopolymerization

Vat photopolymerization, also known as stereolithography (SL), designates methods for creating 3D objects using a light-emitting device, e.g., laser or digital light, to selectively illuminate and cure a liquid photopolymer resin layer by layer [60], as

illustrated in Figure 2.7. This group of AM processes is also known as photolithographic 3D printing and can be categorised into four main techniques, including stereolithography apparatus (SLA), digital light processing (DLP), digital light synthesis (DLS), and liquid crystal display (LCD) 3D printing [58, 70].

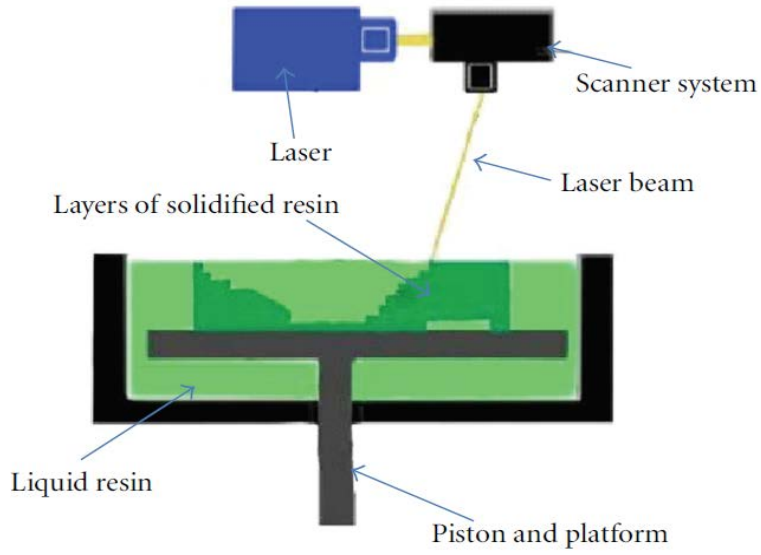

Figure 2.7. Schematic of stereolithography process [59]

Although the above seven groups of AM processes build parts layer by layer, material jetting, material extrusion and DED are further grouped as processes that can build a layer directly on the objects, whilst others require a pre-set layer of the material [71].

2.3. Structural optimization by additive manufacturing

The AM technologies described above empower components to be manufactured additively in a selected shape. Figure 2.8 illustrates AM parts built as three types of

cellular lattice structures, namely face centre cube (FCC), vertex cube (VC), and edge centre cube (ECC) [72]. Such parts with complex 3D porosities are extremely difficult to manufacture using traditional processes, requiring either sophisticated moulds or dexterous machining tools. On the other hand, the structures can be manufactured easily through SLM technology [72].

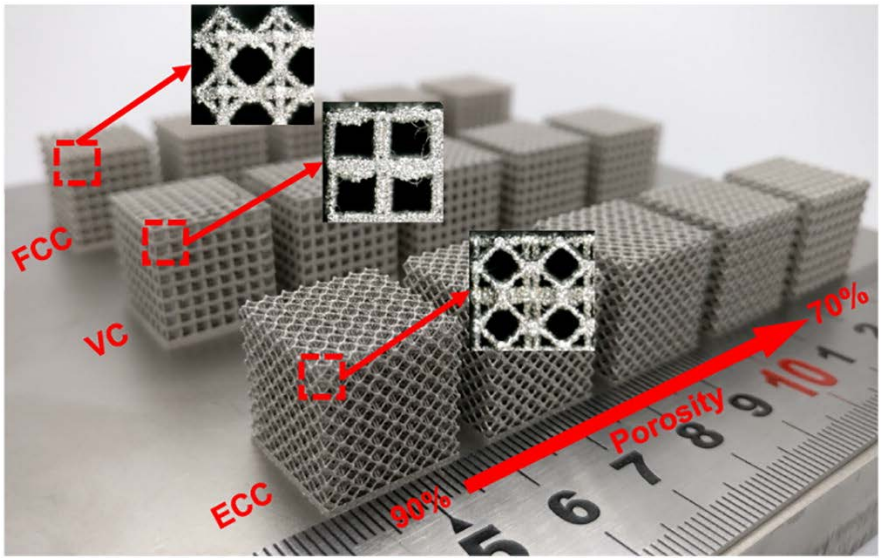

Figure 2.8. AM parts with FCC, VC, and ECC built cellular lattice structures [72]

Furthermore, the manufacturing characteristics of AM technologies can make part consolidation - the process of consolidating multiple components into one piece without assembly operations [23] - a prominent advantage. For example, the AM injector head of Ariane 6 rocket consolidated 248 individual components into one single component, drastically reducing assembly operations such as fastening, welding, brazing and other bonding methods [23]. Another prominent advantage related to structural optimization enabled by AM is mass reduction. Compared with traditional

manufacturing, AM technologies can eliminate spatial constraints in manufacture and significantly increase design freedom, leading to complex structures such as lattices [23, 31, 38, 72].

Moreover, by adopting structural topology optimization introduced in Chapter 1, it is possible to reduce the weight of complex parts considerably, removing redundant material [27, 32]. For example, Figure 2.8 shows AM parts built as lattice structures. The topology optimized structures offer superior performance when compared with ordinary solid structures. Lattice patterns computed using TO can maximise design lightness while meeting mechanical performance criteria [72]. Figure 2.9 shows the lattice structure design of CubeSat bus structure manufactured using AM technology, which achieved a mass reduction of 50% and a 20% increase in stiffness.

Figure 2.9. nTopology and AFIT lattice CubeSat bus structure [23]

The above strategies make AM technologies useful in aerospace applications, bringing significant cost and lead time reductions and enabling the introduction of new materials and designs [23, 27]. Beyond metal alloys, multi-materials were also outlined for manufacturing using AM to find solutions for optimal structures with higher performance [28]. Apart from the brake lever shown in Figure 1.8 which shows a commercial application of composite AM parts, another platform for creating fibre-reinforced cellular structural composite parts with short or continuous fibres was also developed based on fused deposition modeling (FDM) AM technology. The printer head is illustrated in Figure 2.10.

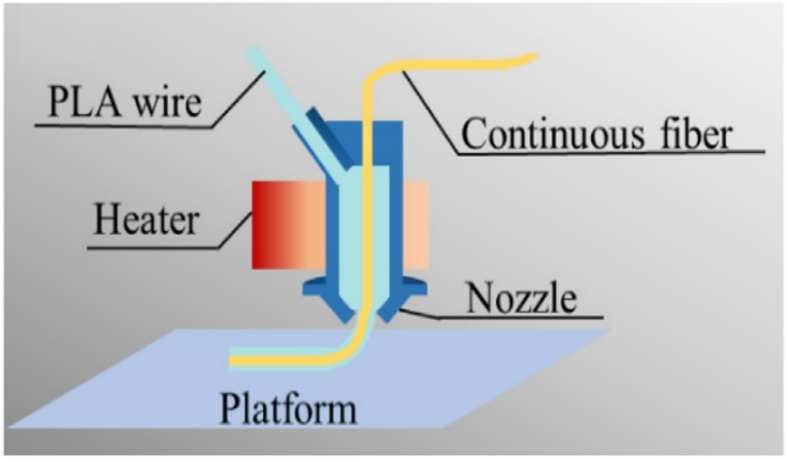

Figure 2.10. Schematic of fiber reinforced AM process [34, 73]

In this strategy, polymer-matrix fibre-reinforcement materials were impregnated by polylactic acid (PLA) matrix and then laid by the 3D printer head [34, 73]. Similarly, liquid deposition modeling (LDM) was also used for printing 3D triangular structures using continuous fibres [74]. The mechanical characteristics and influence of yarn paths

were investigated. Despite their capability to produce intricate, precisely sized components, AM technologies still suffer from limitations on material types and processes. AM processes suffer from elemental evaporation, oxidation, segregation, cracking, and pore development [75], which can produce or transfer defects to finished parts via 3 general ways: feedstock of materials, interaction during melting and processing-related defects, and post-treatments defects resulting from the application of heat [76, 77], as illustrated in Figure 2.21.

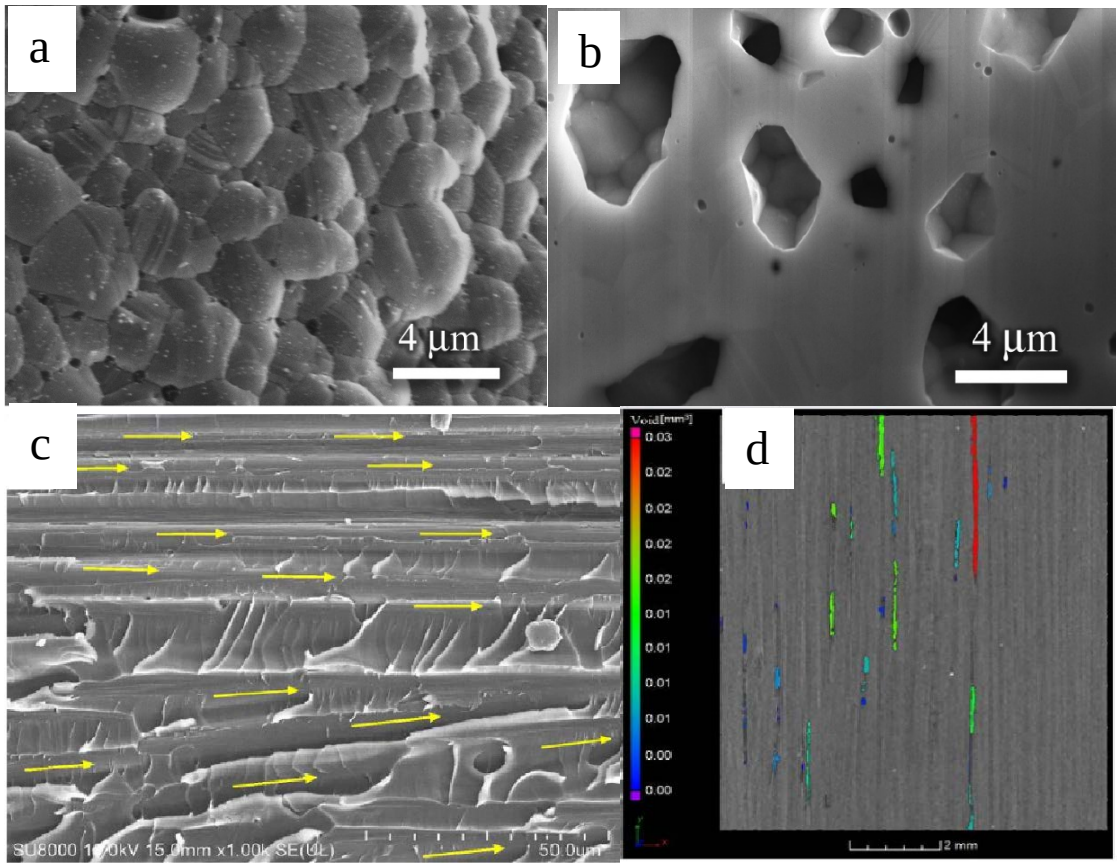

Figure 2.11. SEM images presenting porosities (a, b) in AM metal parts [78] and void distributions (c, d) at fibre-resin interfaces [79]

The scanning electron microscope (SEM) images in Figure 2.21 illustrate general microstructural defects observed in AM components, including various types of porosities. Lack of fusion, balling and keyholes appear in Figure 2.11 (a, b) in metal parts, whilst void distributions in composites appear in Figure 2.11 (c, d) [78, 79]. Other defect types including surface roughness, residual stresses and distortion from AM processes were also studied [76, 77, 80].

2.4. Structural optimization in composites

Despite innovations in AM manufacturing processes for metal alloys, composite materials still offer advantages in terms of higher mechanical performance components with lower mass, produced at lower cost. This latter aspect of the performance envelope of PMFRCs in industrial production is especially enabled by liquid moulding processes, where a liquid resin is infused through a dry textile stack of reinforcement fibres and textiles. The structure of dry reinforcements was the subject of much research effort, leading to improvements in mechanical properties of the PMFRC parts.

The mechanical characteristics of PMFRC parts made from woven reinforcements will differ for different weaving patterns including plain weaves, satin weaves, and twill weaves. The effect of these patterns was studied and compared though experimental tests and numerical FEA simulations by Valentino et al. [75], leading to methods for analysing the stiffness of fabric reinforced composites. Similarly, the in-plane shear behavior is a major mechanical property of woven reinforcement fabrics, influencing their draping ability. Montazerian et al. [81] reviewed and improved testing tools from the limitation of picture-frame tests for studying the shear behaviour, using

kinematic and continuum-based approaches. Ghazimoradi et al. [82] also validated models of biaxial tensile and in-plane shear deformation and performed experimental tests for the uniaxial and biaxial mechanical performance of plain woven PMFRC reinforcements.

2.4.1. 3D woven textile fabrics

Beyond well-known 2D woven fabrics such as plain, satin and twill weaves, 3D warp interlock fabrics offer outstanding mechanical performance for both the dry reinforcement and PMFRCs produced from these reinforcements, for example, both higher resistance to delamination and tolerance to impact were reported, as illustrated in Figure 2.12.

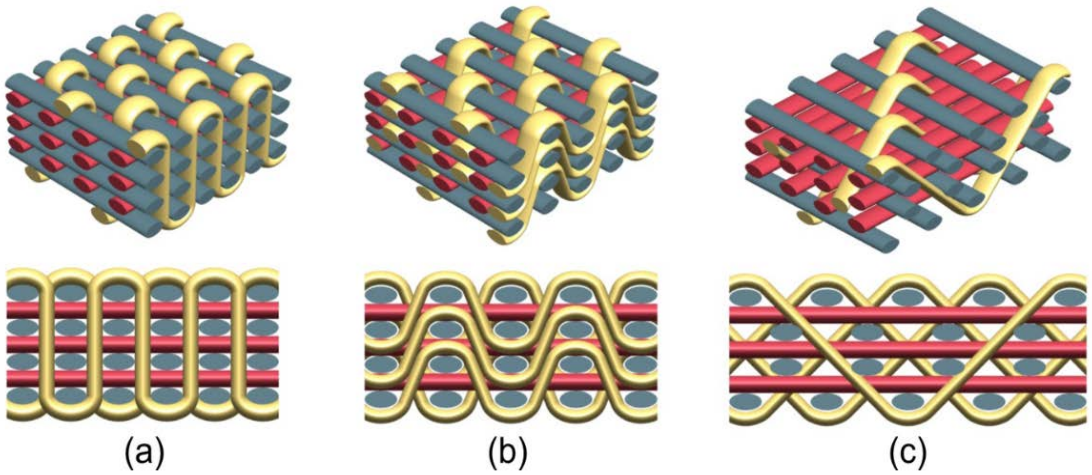

Figure 2.12. Types of 3D angle interlock woven fabrics: a) orthogonal type, b) layer-to-layer type and c) through-the-thickness type [24]

Gereke and Cherif [24] established numerical models of the mechanical properties of 3D woven fabrics. The work featured realistic meso-scale models detailing yarn architecture and interlacing, reduced preforming procedures due to these structural improvements were also reported.

Wei et al. [83] constructed FEA models to evaluate tolerance to ballistic impact, and tested 3D angle interlock woven fabric (AIWF) PMFRCs subjected to projectile impact, offering an instructive method to improve fabric reinforcements for ballistic protection. Guan et al. [84] compared two design changes on yarn fineness and number of yarn layers in 3D layer-to-layer angle-interlock woven fabrics (LLAIWF), and they studied the effect on in-plane shear characteristics, showing that in-plane shear properties were affected and deformation is asymmetrical with varying thickness. Harrison et al. [85] investigated the identification of shear stiffness, out-of-plane bending, in-plane bending and torsional stiffness using two simple tests, by modelling the fabrics in a semi-discrete FEA method combined with specific mesh in their experimental measurements, providing an approach to demonstrate the main mechanical forming characteristics in fabric simulations.

Minapoor et al. [86] adopted a meso-scale FEA model and emulated a series of compression experiments for different weave parameters, namely two different orthogonal weaves, carbon fibre tow type and binder yarns insertion density. The authors showed that inserting densities of adhesive yarns changed the fabric architecture and prevented stress wave propagation from growing more cracks in PMFRC parts, which made an important contribution towards tensile strength of parts made from 3D orthogonal reinforcements. Investigating the behaviour of high stiffness multilayer fabrics, Korkmaz et al. [87] studied the mechanical properties of different 3D warp

interlock fabrics architectures featuring the same amount of carbon fibres in the wrap and weft directions. The authors identified three types of fibre breakage, that were affected by crimp percentage. This could help optimizing fabric structure for forming processes.

Tufting is another manufacturing technology for 3D textile reinforcements. Inserted yarn architectures make PMFRC parts formed with good through-thickness tensile toughness, Figure 2.13.

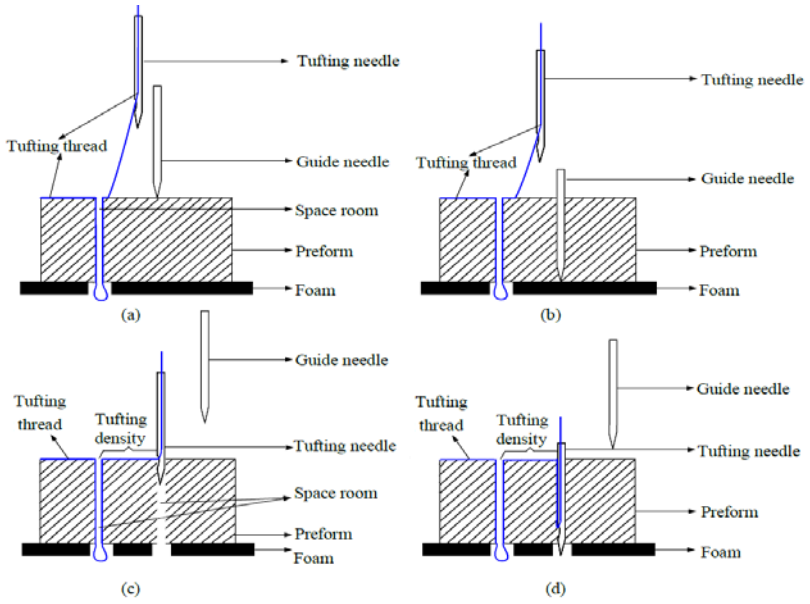

Figure 2.13. Schematics of guide needle tufting process to reduce thread degradation [88]

Hui et al. [88] studied and analyzed disadvantages in terms of degradation of inserted tufting threads. In their experiments, an improvement was designed towards reduced degradation, by using a guide needle without tufting threads, showing that this improvement of the tufting mechanism decreased thread degradation by 30% and significantly improved tensile performance.

Although structural optimization was the subject of sustained effort by the research community towards reaching higher mechanical performance of PMFRC parts, automated preforming technology and manufacturing processes also received much attention in terms of PMFRC manufacturing based on dry textile reinforcements [53]. Linke et al. reviewed the most widely used textile preforming technologies for automated production of PMFRCs.

Compared with manual operations, automating processes can guarantee better quality and consistency during manufacturing, due to stable repetitive work devoid of human factors, making it reasonable to consider automation especially in the aerospace industry facing stringent demands for reproducible mechanical performance of PMFRC parts. De Kruijk [89] illustrated examples of automated fiber placement (AFP) adopted in automated composite manufacturing processes, providing feasible solutions towards advanced technology and materials implementation replacing techniques employed in historical manufacturing. Sample structures with sophisticated patterns using unidirectional (UD) fibers were produced, Figure 2.14. Apart from higher part consistency and quality obtained through better repeatability of the automated process, the replacement of human labour enabled cost reductions around 40-50 % based on the original parts, as well as significant time savings.

Despite preforming technology achievements, manufacturing technologies innovation is also essential to enhancing mechanical performance advancements. Classic manufacturing technologies are still attractive; for example, liquid composite molding (LCM) based on stacked 2D dry textile reinforcements still dominates PMFRC manufacturing because of its better economic price point [90].

Figure 2.14. AFP of a 6-meter spar for an engine pylon [89]

To address poor reproducibility of LCM processes using 2D textile reinforcement stacks, available methods and correspondingly costs for mitigation of variability factors were evaluated and exemplified, using monitoring and control processes. For example, a new manufacturing process labelled in-situ forming of liquid infused preforms (ISFLIP) for PMFRC parts with shell shapes were introduced. A 'C' cross-section prototype PMFRC profile with two sharp joggles was reported by Juan et al. [92], Figure 2.15. Riedel et al. introduced a system labelled model-based systems engineering, dedicated to managing specific requirement and parameter dependencies in the textile product development process [93], towards assisting in evaluating design feasibility.

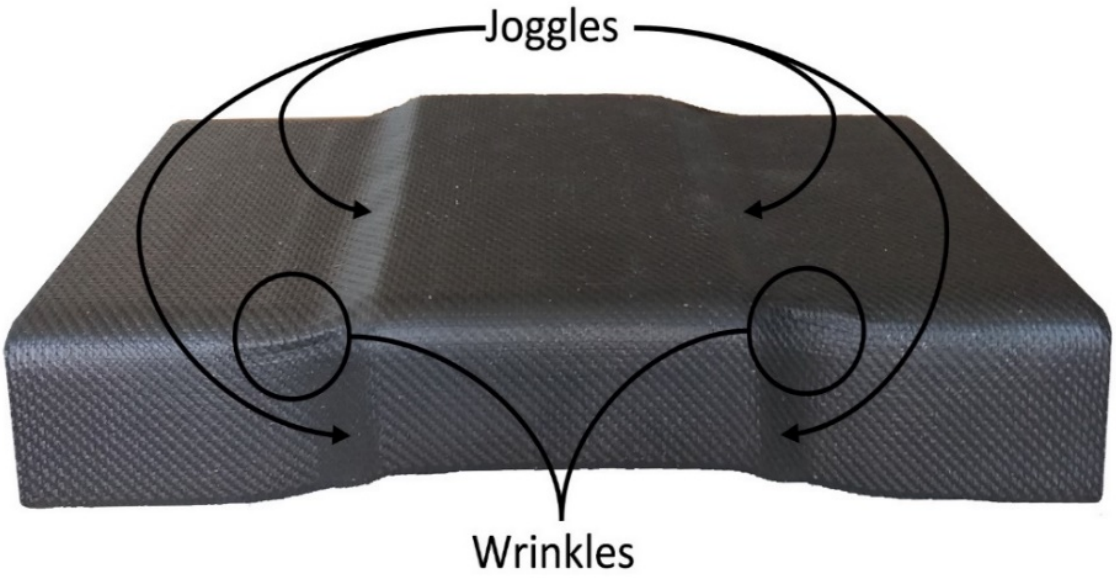

Figure 2.15. FRP component manufactured via ISFLIP [92]

Testing and detection technologies are also the subject of necessary innovation. Unlike metallic materials that feature a relatively certain life cycle, lack of damage accumulation documentation process is an obstacle for textile based PMFRC structures. Consequently, composite designs use large safety factors to remedy precise knowledge of failure mechanisms. Therefore, experimental techniques are heavily depended upon for detecting any possible damage; acoustic emission is frequently applied for continuous inspection of laminated composites [94].

2.4.2. Lattice structures

Beyond AM technologies targeting mass reduction, structural researchers also explored PMFRC parts with lattice features, as structure built from a web of interconnected members can provide excellent structural efficiency and stiffness, even

when made of metal alloys [38, 95, 96]. Relevant studies have demonstrated outstanding mechanical properties under compression, shear, bending and impact in both metal alloy and PMFRC components [97]. Unlike isotropic materials like metal alloys, PMFRCs are inherent orthotropic, hence lattice truss structures made from PMFRCs can offer better performance by aligning fibres axially with external primary loads [98, 99]. Highly efficient lattices can therefore be obtained from the combination of PMFRCs and structure geometry.

2.4.2.1. Pyramidal and grid core structures

One main method of manufacturing lattice structures from PMFRCs is to pre-manufacture lattice elements and later assemble them as a lattice geometry [39]. Such assembly causes separative fibre joints between adjacent elements, which in turn may lead to interfacial debonding and other unresolved problems. Yin et al. [100] designed composite pyramidal lattice (CPL) cores, by using two stacking patterns of hierarchical composite pyramidal cores together, Figure 2.16. Testing showed excellent mechanical characteristics in tension and bending. Wu et al. [97] improved the lattice truss core by interlocking composite struts with top and bottom aluminum connectors, leading to significant improvements in compressive and shear performance.

Besides these enhancements, Shi et al. [101] investigated enhanced types of composite pyramid lattice core structures to further improve interface strength and bearing capacity. Stiffness, displacement, and buckling were studied computationally. One type of reinforcement with surrounding vertical rods, Figure 2.17.

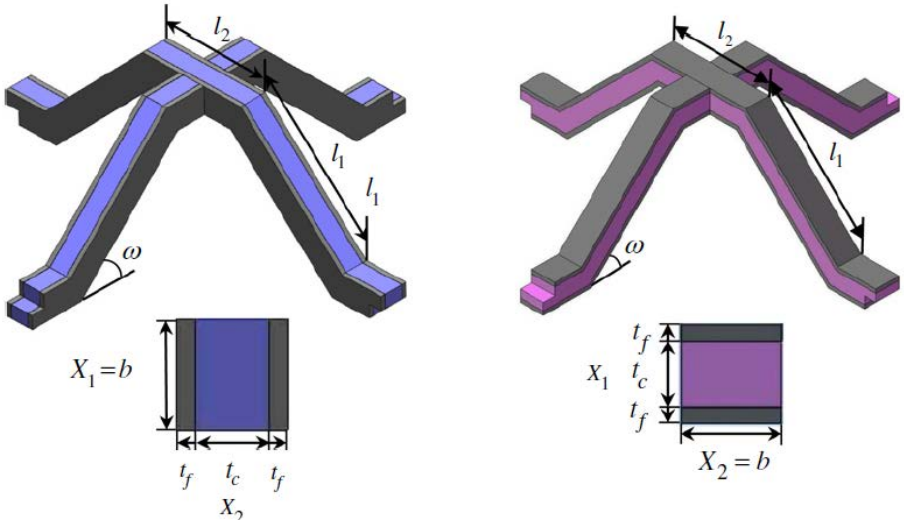

Figure 2.16. Composite pyramidal lattice (CPL) core structure [100]

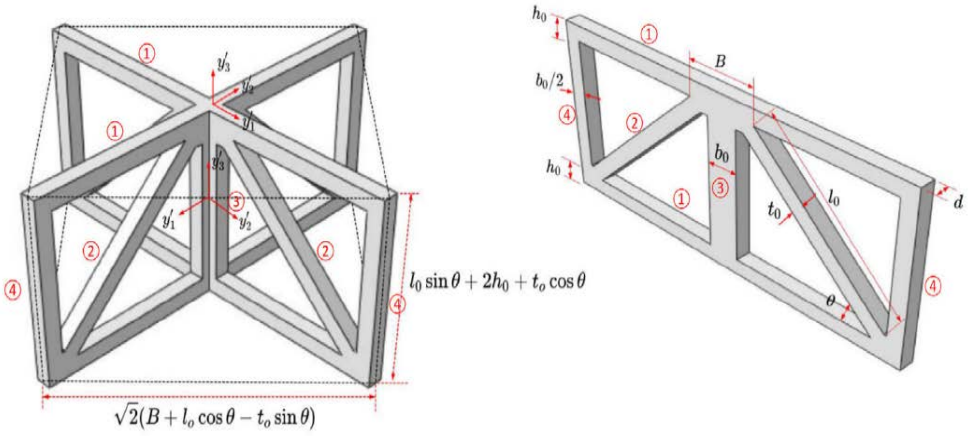

Figure 2.17. Examples and dimensions of enhanced pyramid lattice cells [101]

Those cells enabled smaller static displacements and larger buckling loads, and much lower local stresses. Gan et al. [102] modified lattice cores to improve the impact resistance of hierarchical lattice structures; impact simulation results showed that their hierarchical structures performed better in terms of impact resistance, when compared with hollow structures. Besides, Li et al. [103] also proposed predictions and experiments

to prove that the compressive stiffness and failure modes of the composite pyramidal truss cores were also affected by thermal environment, illustrating that low temperatures increased the compression properties of their lattice cores.

Grid core is another lightweight structure equivalent to pyramidal truss cores, applied to PMFRC sandwich structures. The difference between them is structural variability, as grid core structures consist of regular smaller grids and shapes such as triangles, squares, hexagons, etc. [104]. Reinforced structures with grid cores can offer outstanding mechanical properties and structural resistance, for a light weight. The manufacturing processes and related methods of producing composite grid structures (CGS) were outlined with different geometries including cylindrical and flat shapes [41, 105, 106]. Geometrical and structural characteristics were tested and compared.

2.4.2.2. Isotruss structures

Another manufacturing process for lattice structures consists in using continuous fibres to form lattice elements and the lattice geometry at the same time. Unlike the method of pre-manufacture and assembly, the approach brings about distinctive structures, as the first method causes fibre joints and separations between adjacent elements, while the latter enables some fibre continuity and requires less or no assembly. Differences in geometry connection and member consolidation result in different mechanical properties for the composite structures [39].

Among these, PMFRC isoTruss structures are usually implemented as structural beams for longitudinal compression and/or bending resistance [107, 108]. Weaver and Jensen [107] investigated graphite epoxy PMFRC isoTruss structures, Figure 2.18, testing performance under compression, tension and torsion, and revealed that higher mechanical stiffness in isoTruss structures is obtained by increasing fibre interconnectivity of unit cells.

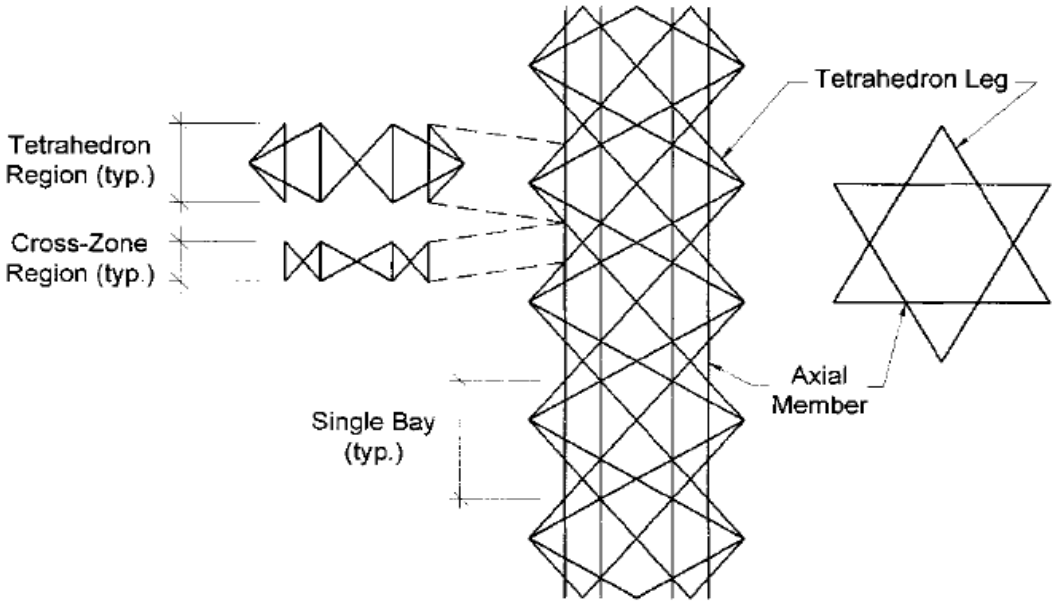

Figure 2.18. Schematics of isoTruss structures featuring essential regions and numbers [107]

Lai et al. [37] designed tooling for fabricating lattice truss structures with a local consolidation process. Their flexible tooling could fasten the whole consolidation process dramatically, and their method led to a 48% improvement in compression strength.

Sui et al. [44] modelled isoTruss structures with FEA and theoretical analyses to probe their buckling resistance under compression and torsion. Their parameterized models predicted forces and moments accurately. FEA modeling methods [109] were also developed for studying free vibration modes and fundamental frequencies of PMFRC isoTruss structures. Predictions were consistent with numerical simulations when applied to the dynamic loading aspect of designs. Gurley et al. [110] created a braiding process for producing optimal lattices composite structures. Through integration with FEA tools and topology optimization methods, open structure composites with braided truss were manufactured with speed and accuracy.

2.4.2.3. WrapToR truss structures

Continuously wound truss structures constitute an important subset of isoTruss structures. Ju et al. [111] investigated the stiffness properties of a PMFRC truss featuring triangular cross-section cells, Figure 2.19. Through parametric studies and validated experiments, individual geometry caused changes in flexural properties and performance of PMFRC trusses. Further enhancement was implemented through an optimization toolbox, adjusting the final structure design leading to significantly reduced mass [112]. Another version of highly efficient PMFRC truss structures with continuously wound truss concept was explored by Woods et al. [108]. A prototype was manufactured by simple winding, for testing and optimization. Compared with composite tubes, the work showed that continuously wound truss structures potentially lead to structural efficiency rising by two orders of magnitude in terms of stiffness in bending and compression with respect to mass.

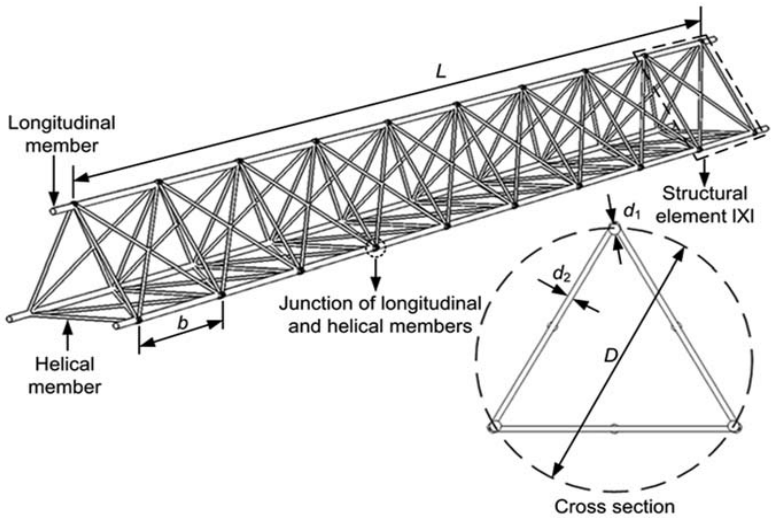

Figure 2.19. Schematic view of triangular cross-section composite truss [111]

PMFRC structural members manufactured by winding were labelled Wrapped Tow Reinforced (WrapToR) trusses by Hunt et al. [98], Figure 2.19. Aiming at optimizing structural efficiency, a procedure of twisting the tow bundles was incorporated in the winding process, leading to much enhanced buckling resistance capacity through a 51% increase in shear resistance of truss shear members. This structure also presented 9% lower mass and doubled loading capability when compared with an 8 mm pultruded composite tube. At the same time, a structural model was proposed according to the novel truss configuration, for predicting pre-failure mechanical response. Results predicted deflections and strains accurately [99].

2.5. Chapter Summary

PMFRCs are lightweight materials with anisotropic characteristics, which makes it possible to design structures with high stiffness and mechanical properties for specific

optimization needs [98, 99, 111, 112]. In current applications of PMFRC parts, optimization of geometry and manufacturing processes can make composite shells stronger and lighter [83-85, 91-93]. However, rapidly increasing application of AM technologies mean that traditional materials like metal alloys can be produced efficiently in structures featuring complex topology though structural design optimization and manufacturing process innovation [27, 32]. Emerging technologies for manufacturing PMFRC lattice structures enable PMFRC parts to be created with enhanced mechanical properties and complexity [37, 101-107, 109]. Innovations in open structures enable composite parts such as WrapToR structures to be manufactured, offering high loading capacity and bulking resistance compared with the tradition shell shapes for PMFRCs [98, 99].

Chapter 3. Computational Methodology

3.1. Dry reinforcement and steepest ascent algorithm

The Steepest Ascent (SA) method is employed for locating the optimum of a function. The approach assumes that the quickest rising or decreasing gradient at a particular probing site is the best search direction at that site. As a result, identifying the gradient at that site determines which way to explore further. The computation of gradients and the size of steps towards the next probing site are two key features of the procedure. As long as gradients are positive, the search will continue in the same direction [113]. When the gradient turns negative, both the search direction and step size change. The search will stop when convergence is reached, where the difference between successive iterations reduces below a set threshold. Then, an optimum location is determined.

3.1.1. Yarn length to determine the mass of composite parts

The goal of the work reported in this thesis is to design and produce open truss interlaced composite parts where PMFRC material is distributed within the part envelope in a way that reduces strains under a set load case for a given total material mass, maximizing the structural contribution of every element of material as well as specific structural stiffness. PMFRC material is distributed and oriented specifically as a function of load cases, in a way that maximizes stresses in most locations without reaching failure. To put it another way, the part envelope is conceptually filled with PMFRC material, and then some material is conceptually removed whilst the rest is reoriented until a minimal

mass of material is present, that will sustain the loads and ensure their transfer at boundary and contact points. In this conceptual vision, the remaining material features yarns that are oriented in ways that ensure yarn continuity and maximal structure stiffness.

In this work, segments of continuous dry yarn maintained under tension are used for part manufacture. These dry yarns are first brought to an optimal geometric configuration and are then impregnated with resin and transformed into a PMFRC truss after resin cure. Yarns are tensioned at their ends and interlace within the part envelope in the initial stage of manufacturing where an optimum tensioned dry yarn tensile truss is built. Figure 3.1 shows a simple example with yarns 1 and 2 interlacing, and yarns 3 and 4 interlacing, at different points. All yarn identification numbers appear at yarn ends. In this example, neither yarn 1 or 2 is in contact or interlaces with either yarn 3 or 4, hence the truss is not complete.

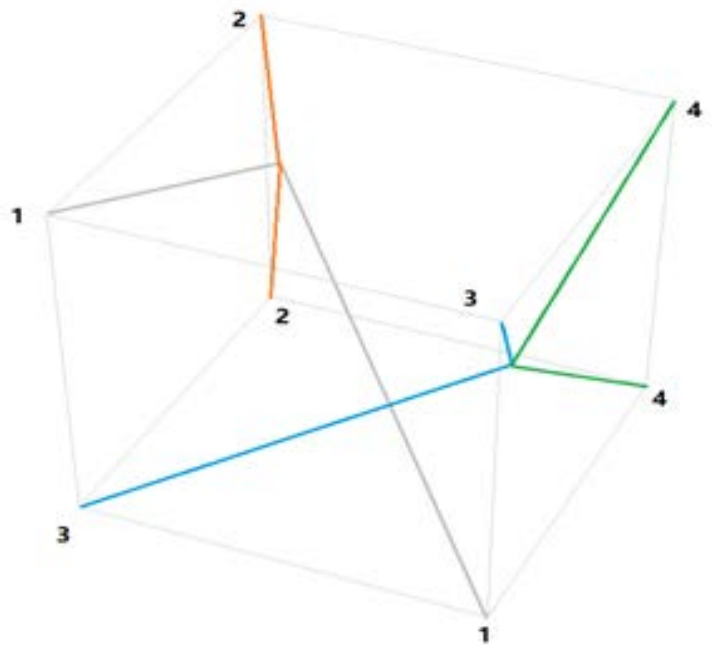

Figure 3.1. Interlacing diagram for pre-equilibrium 3D discontinuous, incomplete dry yarn tensile truss featuring 4 yarns and 2 interlacing points

The general concept can be used for creating more sophisticated 3D examples where all yarns are in contact with at least one other yarn. In the case of a simple 3D structure, dry textile trusses subjected to yarn tension are considered. A pre-set part envelope is defined along with a given number of yarns, their endpoints, and initial, arbitrary, non-optimized, pre-equilibrium yarn interlacing positions. Equilibrium positions are then identified for the dry yarn tensile truss as a function of yarn tensions, which are kept constant at this stage. This first step is strictly about identifying the equilibrium positions of interlacing points in the dry yarn tensile truss under set yarn tensions, irrespective of any loads that may be applied on the PMFRC structure once it is turned into a composite structure and subjected to external loads, hence pre-optimization. To be clear, the aim of this first step is not to optimize the position of interlacing points for optimal performance of the PMFRC structure by varying the yarn tensions. The first step positions the interlacing points in the dry yarn tensile truss, so that the truss is in a state of internal equilibrium under set but unchanged levels of yarn tension.

For the 2D case shown in Figure 3.2, yarn 1 in grey and yarn 2 in red interlace, yarn 2 and yarn 3 in yellow interlace, and yarn 3 and yarn 4 in black interlace. Therefore, the dry yarn tensile truss is continuous in the sense that all yarns are connected to at least another yarn, excluding circular references. The numbers in Figure 3.2 represent yarn ends, where a yarn connects to a tensioning device. The green circles identify boundary points, which are locations on the part envelope where a continuous yarn is redirected into the envelope; in practice these positions are eyelets, which are also labelled boundary points and determine some external dimensions of the entire structure. As the dry yarn tensile truss is modified and adjusted under varying yarn tensions, low friction is useful;

friction is assumed to be negligible when optimizing the dry yarn tensile truss internal geometry. A first demonstration is provided below for 2D structures, for explanation and discussion purposes.

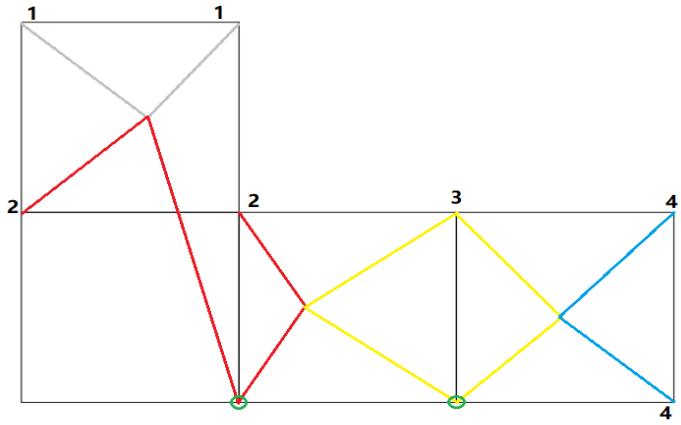

Figure 3.2. Interlacing diagram for pre-equilibrium 2D continuous dry yarn tensile truss featuring 4 yarns, 1 interlacing point, and 2 boundary points

Unlike parts made from metal alloys, the mass of which is determined by the volume of the part and density of the alloy, it is reasonable to calculate the mass of dry yarn tensile trusses presented in this thesis through their total yarn length as cross-section properties are assumed to be constant. As yarn tensions are adjusted, yarn length is added or removed from the dry yarn truss, before it is turned into a PMFRC structure. Eventually, the mass change is reflected by yarn length change, and the expected mass of an open truss PMFRC part can be estimated directly from geometrical information, without need for weighing the part itself – which cannot be done at design and optimisation time. Figure 3.3 shows a simple case featuring a single interlacing point in a 2D domain.

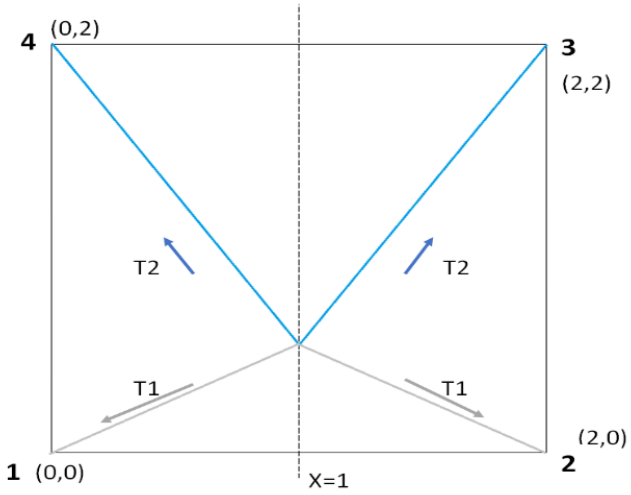

Figure 3.3. Interlacing diagram for pre-equilibrium 2D continuous dry yarn tensile truss featuring 2 yarns and 1 interlacing point

The 2D square envelope of size 2 by 2 has corner 1, 2, 3 and 4 coordinates (0, 0), (2, 0), (2, 2) and (0, 2) respectively. Yarn 1 extending between corners 1 and 2 through the interlacing point is subjected to tension T1, while yarn 2 extending between corners 3 and 4 through the interlacing point is subjected to tension T2. Using symmetry, half of total yarn length is calculated as follows:

$$L = \sqrt{(1^2 + y^2)} + \sqrt{(1^2 + (2 - y)^2} \qquad (3.1)$$

where *y* is the vertical position of the interlacing point. As expected, *L* is independent of tension levels *T1* and *T2*, although *T1* and *T2* will determine the position of the interlacing point through force equilibrium or minimum strain energy as discussed below. The system is presumed to be frictionless hence it follows that the interlacing point is located along central line (1, 0) to (1, 2) as interlacing along this line will minimize total

length as shown by the map of total yarn length over the domain, Figure 3.4. The minimum length solution can be identified mathematically with $\frac{\partial L}{\partial y} = 0$, and the answer is found as $y = 1$. Total yarn length is found as a concave function of x and y coordinates in Figure 3.4, where minimum length can be identified as 5.66 for interlacing point (1, 1). In comparison with derivation solutions, the function map is useful in terms of demonstrating numerous solutions and as an introduction to 3D cases.

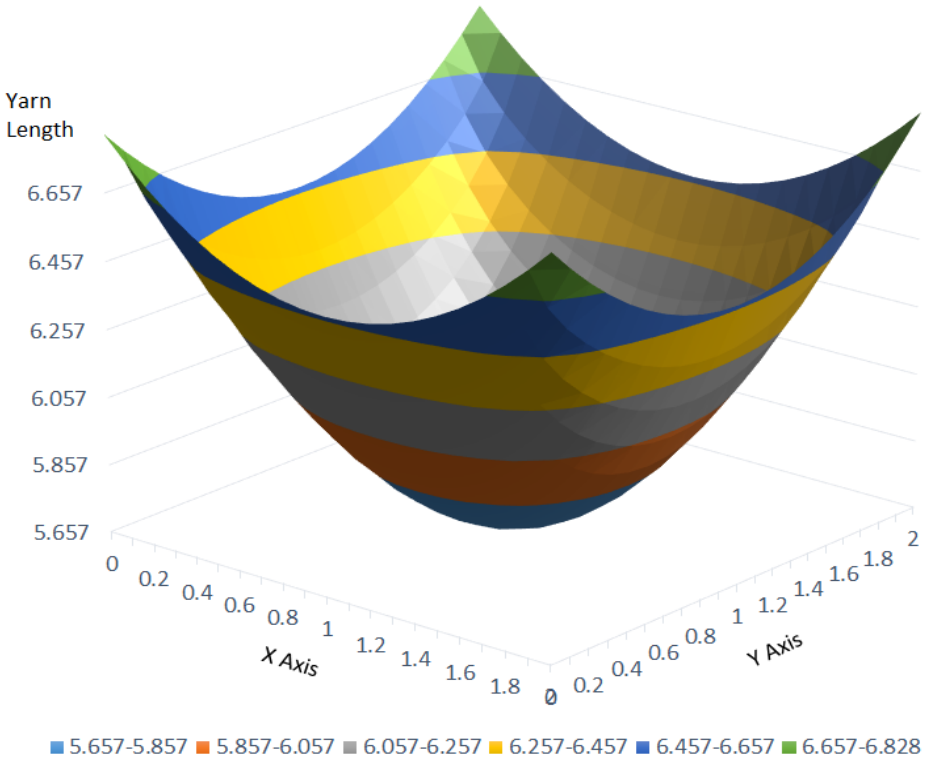

Figure 3.4. Yarn length as a function of interlacing point position for 2D continuous structure featuring 2 yarns and 1 interlacing point

3.1.2. Strain energy for equilibrating the dry yarn tensile truss

Strain energy is used frequently for determining the reaction of a structure to external loads and internal stresses. A prismatic bar with length L subjected to quasi-

static uniform tension *P* lengthens by displacement *d* when load reaches its maximum value *P*. Force *P* increases linearly from 0 to *P* as its point of application travels progressively throughout the length incrementation of *d* and does a specific amount of work during this process. Thus, the strain energy in the tensioned bar is equivalent to the work done by a gradually applied load [114], and it is expressed as:

$$U = \frac{P*d}{2} \tag{3.2}$$

where *d* is the elongation of the bar. Strain in the bar is obtained using material stiffness in the direction of loading, within the elastic range.

Similarly, upon applying a tensile load on a dry yarn, strain energy is stored in the yarn. However, calculating displacements and strains accurately in dry yarn tensile trusses with moving interlacing points in order to use force equilibrium is challenging numerically, especially for complex cases with multiple yarns and small displacements defined in 3D. Knowing that the longitudinal Young's modulus of the material *E* is a constant,

$$Constant = \frac{P}{A} * \frac{L}{d} \tag{3.3}$$

and given the condition that loading force and material property remain the same at all times, yarn elongation will be proportional to its length. The quantitative relationship for strain energy in dry yarn material can be expressed as proportional to the individual yarn segment lengths multiplied by individual tensions. Therefore, strain energy is

proportional to individual yarn length. The quantitative relationship determining strain energy is labelled Generalized Strain Energy (GSE).

For example, considering Figure 3.3, given system symmetry the interlacing point will be located on the vertical centreline, i.e. on a line extending between points (1, 0) and (1, 2). Labelling the vertical coordinate as *y* and assuming that all yarns have constant cross-section and material properties, as the system is symmetric, half the total strain energy can be formulated as proportional to:

$$U = T_1 * \sqrt{(1^2 + y^2)} + T_2 * \sqrt{(1^2 + (2 - y)^2} \qquad (3.4)$$

As for Equation 3.4, the minimal strain energy value can be computed as $\frac{\partial E}{\partial y} = 0$. When tensions T_1 and T_2 have equal magnitudes, solving leads to $y = 1$: the interlacing point of the 2 yarns, 1 interlacing point dry yarn tensile truss with equal tensions in both yarns is located in the domain centre. Force equilibrium at the interlacing point confirms the solution.

Minimization of length and minimization of strain energy towards static equilibrium can be compared for the case discussed above. However, it is worth noticing that the distribution map for minimum length and for minimum energy are not the same. The magnitudes of length and energy are different; the minimal length is independent and only affected by the coordinate system. Once yarn tensions change, the location of minimal GSE will be relocated and cause an incremental to total yarn length.

The same solution can be performed with any tension levels, leading to different positions for the interlacing point, as validated experimentally in Chapter 5. Hence, GSE

for all yarn segments in the dry yarn tensile truss can be expressed as:

$$GSE = \sum_{i=1}^{n} P_i * L_i \tag{3.5}$$

where *i* is a segment identifier and *n* stands for the total number of yarn segments in the structure.

Overall, equilibrium positions of interlacing points in dry yarn tensile trusses where yarns are subjected to different levels of tension are identified through minimization of GSE generated by tension forces along yarns in the tensile truss. The strain energy stored in all yarn segments extending between interlacing points is a function of the tensile stress and amount of material, namely yarn cross-section and length.

However, instead of using derivation, an iterative calculation is deemed more efficient in finding answers, and it can be more readily expanded to more complicated 3D systems featuring multiple interlacing points, as discussed below. For example, consider the same domain and system from Figure 3.3. If yarn tensions are $T_1 = T_2 = 1$ N, the interlacing point will be in the centre of the domain and the GSE map will be the same as its yarn length map. However, with different yarn tensions, say $T_1 = 10$ N and $T_2 = 5$ N, it can be suggested instinctively that the interlacing point will be closer to the yarn subjected to higher tension as higher forces pull the interlacing point in. Moving the interlacing point will lead to lower GSE. The resulting GSE map is illustrated in Figure 3.5.

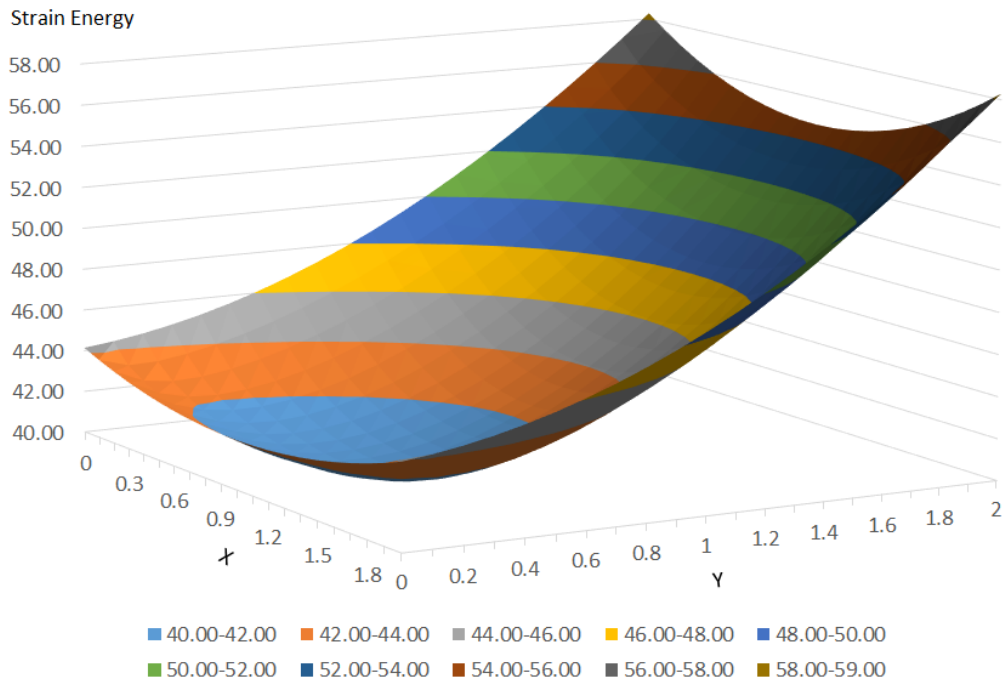

Figure 3.5. Stain energy distribution as a function of interlacing point position for 2D continuous dry yarn tensile truss when $T_1 = 2\ T_2$

A minimum GSE of 40.388 N·cm is found at $x = 1$, $y = 0.5$. Verification of force equilibrium at the interlacing point confirms that the location is correct. As a result, minimizing the sum of products of yarn length and yarn tension for each yarn segment leads to the correct solution, assuming a constant yarn cross-section everywhere or adapting for different yarn cross-sections.

The above single crossover case has demonstrated the functional process where minimum strain energy determines equilibrium interlacing point positions in dry yarn tensile trusses. Position can be modified through different tension combinations. It is necessary to expand this simplest 2D case to multiple interlaced yarns, as well as developing non-planar examples defined in 3D. These two paths will then converge towards solving for larger numbers of yarns interlacing in 3D.

3.1.3. Steepest ascent method for energy minimization in dry yarn tensile trusses

Two illustrative examples were given above, providing basic insight into the application of minimum strain energy theory to interlaced open dry yarn tensile trusses for determining interlacing point positions. In this section, implementation is expanded to more complex cases, to confirm the same deduction. The progressive effort to address the problem using corresponding parameters in 2D and 3D domains is performed in steps, starting with the few following simple examples.

Even though the above simple case featured only one interlacing point, 400 calculations were required for producing the strain energy map, using a position interval of 0.1 within a 2 by 2 square domain. Had the interval on the domain grid been set to a smaller value, for example 0.01, the number of calculations required would have increased to 40 000 – 100 times higher than for the original setting – for a single interlacing point defined in a 2D domain. Clearly this is unsustainable computationally. By contrast, applying a SA algorithm will significantly reduce the calculation effort required.

Applying SA for cases with one variable is straightforward. Firstly, one makes sure of the variable to be optimized as well as its starting condition, normally labelled iteration 1. Secondly, the initial value of step size is set, which determines the speed and accuracy of optimization progress [113]. Setting the initial step size to a much larger or smaller value would slow down the entire process through additional iterations. For example, if a current answer was close to an optimum from the start, large step sizes would lead to many changes in direction as the gradient would alternate between positive and negative values repeatedly.

Thirdly the strain energy calculation system is set. As discussed before, in this

work SA is applied on the strain energy of the whole interlacing dry yarn tensile truss. By comparing energy on successive iterations and reaching minimum energy in the dry tensile truss, the optimum positions of interlacing points are determined. In order to apply SA effectively, it must be ensured that the minimum energy identified by the steepest ascent algorithm is the true minimum solution over the whole domain, instead of a local optimization. However, SA does not necessarily identify a global optimal solution, but possibly a local optimum over a limited range. Of course, if the optimization process is performed for a convex function, namely a function that has only one minimum or maximum over the domain, then the solution obtained is the global optimum.

In order to make the calculation process efficient for cases featuring numerous interlacing points, a search strategy was implemented along with an SA algorithm for identifying locations, as described in the following sections.

3.1.4. Applying SA algorithm to GSE computation

Interlacing is one of the easiest, most widespread, and most flexible techniques for producing textiles and it is used in virtually every textile process including weaving, braiding and most others. In the present work, one specific interlacing pattern is required as a given initial condition. From this interlacing pattern, the number of points where yarn tension must be balanced is determined, along with yarn orientations at interlacing points, for all dry yarns. Changes to the geometry of the dry yarn structure are caused by different external tensions applied on individual yarns since every interlacing point must maintain force equilibrium as interlacing position shifts. However, these changes in interlacing points positions do not alter the interlacing pattern, in the sense that one given yarn will always interlace with the same other yarns as tensions are varied and optimized.

3.1.4.1. Interlacing patterns

Most typical 2D textiles are built, used and modelled as either continuous sheets or as ensembles of identical and equally spaced repeating unit cells. Hence, the internal configuration of yarns in textiles is seldom discussed, save possibly for quantifying transport properties such as thermal conductivity or permeability to liquids or gases [118, 119].

In this work, when the endpoints of interlacing yarns are localized in an external envelope or frame and the complete interlacing patterns are pre-set, interlacing point locations and resulting dry yarn tensile truss geometry will be altered by tension changes. Upon determining these positions numerically, the final dry tensile truss will also be determined, and forces at interlacing points will be equilibrated. Collectively, the locations of interlacing points must meet the requirement of minimal GSE for the entire structure.

Figure 3.6 illustrates an 8 yarns and 10 interlacing points case, showing the 2D domain area. The 8 yarns are labelled as yarn1, yarn2, …, yarn8 respectively. With 2 different end points for every yarn, there are 16 boundary points labelled from 1 to 16, which can be regarded as yarn inlets and outlets. Coordinates for the 16 boundary points appear in Table 3.1. In this case, all these points are input and output of dry yarns with positions that are regarded as fixed on an external rigid body frame. Point 1 is the origin of the coordinate system.

The eight yarns are interlaced, creating ten interlacing points in this case, labelled point *a*, point *b*, …, to point *j*. Contrary to boundary points, the locations of interlacing points are not fixed and will vary with yarn tensions, hence they must be identified through the SA algorithm applied to GSE. A listing of yarn connections appears in Table 3.2.

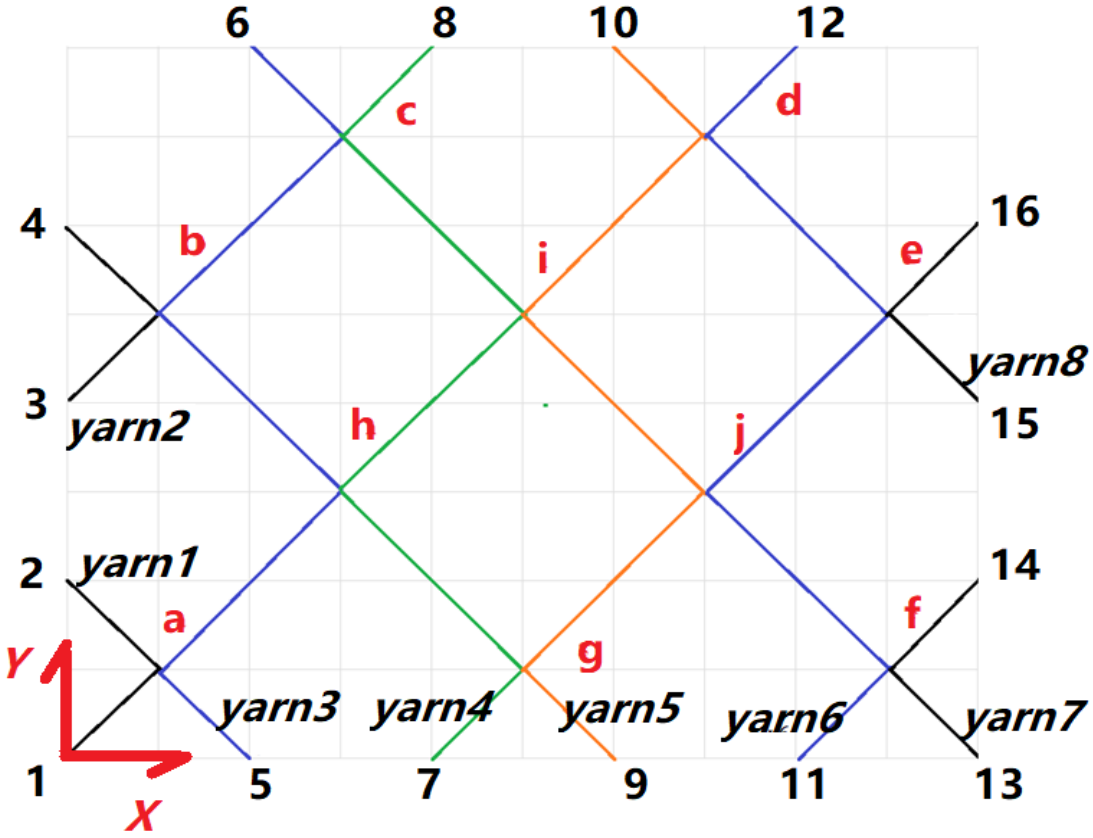

Figure 3.6. Interlacing diagram for pre-equilibrium continuous dry yarn tensile truss featuring 8 yarns and 10 interlacing points

Table 3.1. Coordinates of boundary points

Point #	1	2	3	4	5	6	7	8	9	10	11	12	13	14	15	16
X	0	0	0	0	2	2	4	4	6	6	8	8	10	10	10	10
Y	0	2	4	6	0	8	0	8	0	8	0	8	0	2	6	8
Z	0	0	0	0	0	0	0	0	0	0	0	0	0	0	0	0

Table 3.2. Yarn connection information

	Yarn 1	Yarn 2	Yarn 3	Yarn 4	Yarn 5	Yarn 6	Yarn 7	Yarn 8
End point #1	1	3	5	7	9	11	13	15
End point #2	2	4	6	8	10	12	14	16
Intersecting point #1	*a*	*b*	*a*	*g*	*g*	*f*	*f*	*e*
Intersecting point #2	/	/	*h*	*h*	*j*	*j*	/	/
Intersecting point #3	/	/	*b*	*i*	*i*	*e*	/	/
Intersecting point #4	/	/	*C*	*c*	*d*	*d*	/	/

3.1.4.2. Determination of initial positions for interlacing points

Tentative initial positions must be identified for interlacing points in the dry yarn tensile structure, at the beginning of the iterative process, in pre-optimal status. Yarns with higher tension will pull interlacing points towards their direction; conversely, the algorithm will locate the interlacing point in a central position if two interlacing yarns carry the same tension. Therefore, it is suggested that central locations are good starting positions for pre-optimization interlacing points, thereby reducing processing time. However, it is worth noting that assigning initial positions of interlacing points to central locations is not mandatory, and that it is important to keep the initial position within subdomains delimited by boundary points. The following examples show that initial positions only have slight impact on processing times. Interlacing points *b* and *c* are given as examples in Figure 3.7:

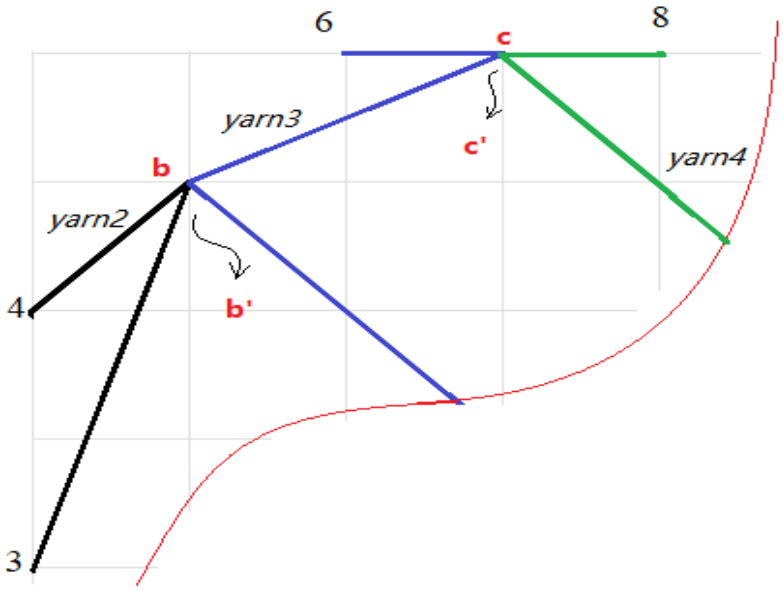

Figure 3.7. Arbitrary interlacing positions in dry yarn tensile trusses, prior to SA GSE optimization

Point *b* is defined as the interlacing point between yarn 2 in black and yarn 3 in blue. The four boundary points 3, 4, 6 and 8 are known, with coordinates (0, 4, 0), (0, 6, 0), (2, 8, 0) and (4, 8, 0) respectively. As the boundary points nearest point *b* are points 4 and 6, the initial position of point *b* can be determined simply within the reasonable domain as:

$$[b_X \quad b_Y \quad b_Z] = \left[\frac{(4_X + 6_X)}{2} \quad \frac{(4_Y + 6_Y)}{2} \quad 0\right] \qquad (3.6)$$

Thus, the initial position of interlacing point *b* is generated as (1, 7, 0). Applying the same rules between points 3 and 6 or points 4 and 8 is feasible; as explained above, this barely makes a difference on further SA GSE iterations once the optimization process is underway. Similar operations take place for other interlacing points including point *c*

at the interlacing of yarn 3 and yarn 4 in green, the initial positions of which can be defined between points 6 and 8, or between points *b* and 8, once point *b* has been positioned. The purpose of choosing initial locations is to set a starting point for iterations.

Once initial positions are set, the GSE of segment *bc* is calculated from Equation 3.5 where T_3 stands for tension in yarn 3 and the geometry input of (*x*, *y*, *z*) is done through geometry matrix $\begin{bmatrix} b_X & b_Y & b_Z \\ c_X & c_Y & c_Z \end{bmatrix}$;

$$f(x,y,z) = T_3 * \sqrt{(b_X - c_X)^2 + (b_Y - c_Y)^2 + (b_Z - c_Z)^2} \tag{3.7}$$

Similarly applying the algorithm to all segments in the dry yarn tensile truss, the objective is formalized as minimizing total GSE, Equation 3.8:

$$E_{minimize} = \sum_{i,j}^{m,n} f(\begin{bmatrix} i_X & i_Y & i_Z \\ j_X & j_Y & j_Z \end{bmatrix}) \tag{3.8}$$

/where *i* and *j* stand for the 2 end points of one segment in the interlacing structure, and *m* and *n* account for all segment endpoints.

3.1.4.3. Determination of gradients for next step

After determining the initial interlacing points coordinates, step sizes for iterations are determined. For example, choosing steps along the *x* axis in a 2D domain where the first iteration starts at arbitrary x_1, the next querying point x_2 would be one of

the two following options: $x_2 = x_1 + \alpha * \frac{dE}{dx}$ in the ascending direction of the gradient, or $x_2 = x_1 - \alpha * \frac{dE}{dx}$ for the descending direction of the gradient [113, 115]. Then, the gradient is obtained again at x_2 and the procedure continues.

According to the GSE Equation 3.8, the GSE value is affected by yarn tensions and the segment lengths. Therefore, when SA algorithm comes to tension optimizations, the tension gradients can be obtained as:

$$\nabla g(T_i) = \frac{\partial E}{\partial T_i} \tag{3.9}$$

where *i* identifies the different interlacing yarns. Considering a situation where all yarn tensions were available as priors in the interlacing process, the GSE value will fluctuate and be minimized at different coordinate data from the interlacing points as they change positions.

Therefore, considering the GSE in a 3D system, search directions along axes *x*, *y* and *z* that reduce GSE are independent as the directional gradients have no relation to each other. For coordinates changing along 3 degrees of freedom (DOFs), the directional gradients are obtained as:

$$\nabla g(x, y, z) = (\frac{\partial E}{\partial x}, \frac{\partial E}{\partial y}, \frac{\partial E}{\partial z}) \tag{3.10}$$

Gradients for further calculations can be acquired dynamically. In following steps, the SA algorithm computes the GSE value according to the different gradients, stopping while the gradients have reached convergence.

3.1.4.4. Rules for SA convergence and equilibrium verification

As the SA algorithm proceeds, each interlacing point gets gradually closer to its target location. Because of differences in the geometry of the target system, and because locations of starting points are arbitrary, some positions will be reached earlier whilst others will require more steps to be identified.

If the derivation formula was used [116, 117], the target value would correspond exactly to a specific minimum value of energy. However, in this work SA is used without an approximation function, and in consequence there is no pre-defined minimum value for the step size. Therefore, it is necessary to set numerical limits to tension and geometrical precision for stopping the SA computing operation.

In the case of yarn tension, a minimum value is used for maintaining tensile stress, and a reasonable maximum value is also set to avoid loads beyond yarn tensile strength, as well as structural issues in the interlacing apparatus. Additionally, geometrical precision is also set according to the physical case.

In SA calculation processes, reaching an exact theoretical minimum or maximum value is possible but uncommon. In this work, most GSE SA calculations will exceed their target, then change gradient direction and automatically reduce the step size, so that the algorithm will make SA query positions move back and forth around the target, progressively moving towards being infinitely close. When the step size becomes less than the required accuracy, an acceptable hence correct position has been reached.

Overall, the rules for stopping SA loops and acquiring target positions are criteria stating that the current interlacing points have identical energies left and right of the target, and that gradients have become lower than a set value.

3.1.4.5. Equilibrium verification

Calculation loops stop when any criterion is satisfied. The geometry of the dry reinforcement is determined once the SA algorithm reaches a point where all interlacing positions collectively meet the requirement of minimal GSE for the structure. Since interlacing point positions are identified through structure equilibrium, which is determined by minimum GSE value, the static equilibrium of tensions applied through the interlacing points must be verified before the dry reinforcement can be transformed into a composite structure. Segments ending at a given interlacing point are filtered and assembled in order to verify their equilibrium status as illustrated in Equation 3.11:

$$\Delta\delta = \sum_{i=1}^{n} T_i * [l_i \quad m_i \quad n_i] * \begin{Bmatrix} \vec{i} \\ \vec{j} \\ \vec{k} \end{Bmatrix} \qquad (3.11)$$

where *T* stands for the tension applied in a yarn segment; *l*, *m* and *n* are the components of *T* along *x*, *y*, *z* directions respectively, which are acquired through geometry information and satisfy Equation 3.12 of the Pythagorean theorem; and $\vec{i}$, $\vec{j}$ and $\vec{k}$ represent unit vectors along *x*, *y* and *z* directions.

$$l^2 + m^2 + n^2 = 1 \qquad (3.12)$$

In the SA process, most target locations are usually values in the precision range around the target locations, rather than the exact theoretical values. Even under a theoretical setting where yarn mass and inter-yarn friction are neglected, computed equilibrium sums at interlacing points cannot reach absolute zero. Therefore, an

additional criterion on force, sufficiently small to be deemed negligible, is necessary on static equilibrium. The criterion for equilibrium verification is labelled as $\Delta\delta \leq T_{min}$.

3.2. Composite structure and FEA

After combination with resin, composite parts are obtained from the dry yarn tensile truss. The geometric information is used for the structural analysis of the PMFRC part, conducted using finite element analysis (FEA) to calculate nodal displacements for the entire structure.

3.2.1. FEA on bar-elements in a 3D domain

FEA is used for determining displacements at points of application of external loads, along with internal stresses and strains in the PMFRC structure. FEA results are used in a second-level SA optimization cycle labelled structural SA. Each structural iteration SA includes both FEA analysis and multiple-iterations, first-level equilibrium SA optimizations. The specific stiffness of the PMFRC open structure part is progressively increased for a specific load case, by iterating dry yarn tensions, re-equilibrating, and re-assessing the structural performance using FEA. In this work, PMFRC segments extending between two boundary, contact or interlacing points are modelled as bars subjected to tension or compression only; torsion and bending are not considered. All structures are triangulated and all bars form tetrahedra to limit deformations in the PMFRC part under load.

3.2.2. Stiffness relationship in local coordinates system for bar element

Consider a bar element *e* defined in a local coordinate system (x', y', z'), Figure 3.8. Local axes *x*', *y*', *z*' are perpendicular to each other. A force is applied along the length of the element from node *i* to node *j*. Nodal displacements are labelled u_i', v_i' and w_i' along x', y', z' directions respectively at node *i*, and the corresponding forces can be disported and labelled as F_{xi}', F_{yi}' and F_{zi}'.

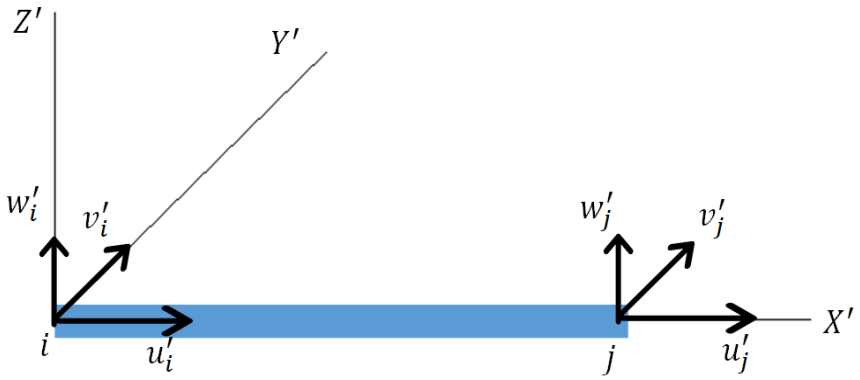

Figure 3.8. Schematic of 3D bar element in local coordinate system

The same applies at node *j* with nodal displacements described as u_j', v_j' and w_j', and corresponding forces as F_{xj}', F_{yj}' and F_{zj}'. From elementary strength of materials,

$$\delta = \frac{PL}{AE} \tag{3.13}$$

where δ represents the axial elongation. It is assumed that the material used in the work is homogenous and loaded within its elastic domain hence material stiffness is constant.

The deformation of the bar element is expressed by the difference of nodal displacements as $\delta = u_j' - u_i'$, hence axial forces at the nodes are:

$$\begin{bmatrix} F_{xi}' & F_{xj}' \end{bmatrix} = \frac{AE}{L}\begin{bmatrix} u_i' - u_j' & u_j' - u_i' \end{bmatrix} \tag{3.14}$$

where the axial forces are in equilibrium as $F_{xi}' + F_{xj}' = 0$. As bar elements only withstand axial forces, then $F_{yi}' = F_{yj}' = 0$ and $F_{zi}' = F_{zj}' = 0$, and no relative, local displacements happen in the transverse directions. A matrix form of the 4 above equations is written as:

$$\frac{AE}{L}\begin{bmatrix} 1 & 0 & 0 & -1 & 0 & 0 \\ 0 & 0 & 0 & 0 & 0 & 0 \\ 0 & 0 & 0 & 0 & 0 & 0 \\ -1 & 0 & 0 & 1 & 0 & 0 \\ 0 & 0 & 0 & 0 & 0 & 0 \\ 0 & 0 & 0 & 0 & 0 & 0 \end{bmatrix}\begin{Bmatrix} u_i' \\ v_i' \\ w_i' \\ u_j' \\ v_j' \\ w_j' \end{Bmatrix} = \begin{Bmatrix} F_{xi}' \\ F_{yi}' \\ F_{zi}' \\ F_{xj}' \\ F_{yj}' \\ F_{zj}' \end{Bmatrix} \tag{3.15}$$

where v_i', v_j' and w_i', w_j' are the transverse displacements, equal to zero. Element length can be computed from coordinate geometry. A more concise matrix form can be written as:

$$\left[K^{e'}\right]\left\{U^{e'}\right\} = \left\{F^{e'}\right\} \tag{3.16}$$

where $[K^{e'}]$ is the matrix of local stiffness, $\{U^{e'}\}$ is the local nodal displacement vector and $\{F^{e'}\}$ is the local nodal force vector for the element. While *e* identifies the element, $'$ stands for the local coordinate system. After transformation, the stiffness matrix will be applicable to a bar element arbitrarily oriented in any direction in the *x*, *y*, *z* plane.

3.2.3. Transformation from local to global coordinate system

A point *P* is arbitrarily oriented in a 3D coordinate system, Figure 3.9. Therefore, vector $\vec{r}$ can be written as 2 different equations corresponding to different coordinate systems:

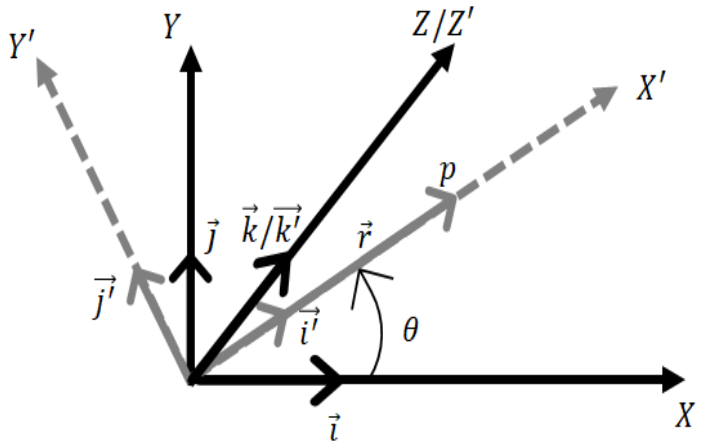

Figure 3.9. Transformation between local and global coordinate systems

Assuming that $\vec{i'}$, $\vec{j'}$, $\vec{k'}$ and $\vec{i}$, $\vec{j}$, $\vec{k}$ are unit vectors for local and global coordinate systems, the vector $\vec{r}$ is written in local coordinate system (x', y', z') and in the global coordinate system (x, y, z) respectively as Equation 3.17:

$$\vec{r} = [r_{x'} \quad r_{y'} \quad r_{z'}] \begin{Bmatrix} \vec{\imath'} \\ \vec{\jmath'} \\ \vec{k'} \end{Bmatrix} = [r_x \quad r_y \quad r_z] \begin{Bmatrix} \vec{\imath} \\ \vec{\jmath} \\ \vec{k} \end{Bmatrix} \quad (3.17)$$

Thus, by applying $\vec{r} * \begin{Bmatrix} \vec{\imath} \\ \vec{\jmath} \\ \vec{k} \end{Bmatrix}$ on the equation, a comparable relationship related to the 2 different coordinate system will be written as:

$$[r_{x'} \quad r_{y'} \quad r_{z'}] \begin{Bmatrix} \vec{\imath'} \\ \vec{\jmath'} \\ \vec{k'} \end{Bmatrix} * \begin{Bmatrix} \vec{\imath} \\ \vec{\jmath} \\ \vec{k} \end{Bmatrix} = [r_x \quad r_y \quad r_z] \begin{Bmatrix} \vec{\imath} \\ \vec{\jmath} \\ \vec{k} \end{Bmatrix} * \begin{Bmatrix} \vec{\imath} \\ \vec{\jmath} \\ \vec{k} \end{Bmatrix} \quad (3.18)$$

Using a scalar product function to solve the equations, the relationship between local and global displacements is described respectively by its triangular coefficients, which can be assembled in matrix form as:

$$\begin{Bmatrix} r_x \\ r_y \\ r_z \end{Bmatrix} = \begin{bmatrix} cos\,(\vec{\imath'}, \vec{\imath}) & cos\,(\vec{\jmath'}, \vec{\imath}) & cos\,(\vec{k'}, \vec{\imath}) \\ cos\,(\vec{\imath'}, \vec{\jmath}) & cos\,(\vec{\jmath'}, \vec{\jmath}) & cos\,(\vec{k'}, \vec{\jmath}) \\ cos\,(\vec{\imath'}, \vec{k}) & cos\,(\vec{\jmath'}, \vec{k}) & cos\,(\vec{k'}, \vec{k}) \end{bmatrix} \begin{Bmatrix} r_{x'} \\ r_{y'} \\ r_{z'} \end{Bmatrix} \quad (3.19)$$

Since all calculations occur in a specific coordinate system, it is necessary to replace trigonometry coefficients with coordinate values. Assuming that the angle

between vectors $\vec{\imath'}$ and $\vec{\imath}$, namely the angle from global to local coordinate system, is θ, and that vector $\vec{r}$ represents the bar element with nodes i (x_i, y_i, z_i) and j (x_j, y_j, z_j), Figure 3.9, the directional cosines in the left column of the matrix can be rewritten as:

$$\begin{bmatrix} cos(\vec{\imath'}, \vec{\imath}) \\ cos(\vec{\imath'}, \vec{j}) \\ cos\ (\vec{\imath'}, \vec{k}) \end{bmatrix} = \begin{bmatrix} \frac{x_j - x_i}{L} \\ -\frac{y_j - y_i}{L} \\ -\frac{z_j - z_i}{L} \end{bmatrix} \qquad (3.20)$$

Similarly, cosines can be rewritten as a product of coordinates. To write the matrix more concisely, Equation 3.19 can be stated as:

$$\begin{Bmatrix} r_x \\ r_y \\ r_z \end{Bmatrix} = \begin{bmatrix} l & m & n \\ -m & l & 0 \\ -n & 0 & l \end{bmatrix} \begin{Bmatrix} r_{x'} \\ r_{y'} \\ r_{z'} \end{Bmatrix} \qquad (3.21\ a)$$

$$\begin{cases} l = \frac{x_j - x_i}{L} \\ m = \frac{y_j - y_i}{L} \\ n = \frac{z_j - z_i}{L} \end{cases} \qquad (3.21\ b)$$

Since Equation 3.21 illustrates the transformation between local and global coordinate systems, the rotation matrix is obtained as:

$$[R_{3D}] = \begin{bmatrix} l & m & n \\ -m & l & 0 \\ -n & 0 & l \end{bmatrix} \tag{3.22}$$

Eventually, the transforming equation for the coordinate system is assembled for nodes *i* and *j* together as:

$$[T] = \begin{bmatrix} R_{3D} & 0_{3X3} \\ 0_{3X3} & R_{3D} \end{bmatrix} \tag{3.23}$$

to express the matrix concisely as an equivalent Equation 3.24 a), in which [*T*] is obtained as the transformation matrix. Similarly, the transformation of the force vector $\{F^{e'}\}$ to the global coordinate system can be achieved using matrix [*T*] as Equation 3.24 b):

$$\{U^e\} = [T]\{U^{e'}\} \tag{3.24 a}$$

$$\{F^e\} = [T]\{F^{e'}\} \tag{3.24 b}$$

therefore, the stiffness relationship in the global coordinate system is obtained as:

$$\left[K^{e'}\right][T]^{-1}\{U^e\} = [T]^{-1}\{F^e\} \tag{3.24}$$

which is equivalent to:

$$[K^e]\{U^e\} = \{F^e\} \tag{3.25}$$

where $[K^e] = [T]\left[K^{e'}\right][T]^{-1}$ represents the global element stiffness matrix, showing the reaction between applied forces and resulting displacements. Combining all the matrices and solving the calculation process, the stiffness matrix representing sub-matrices assembly for two different nodes in one bar element with 3 DOFs can be rewritten as

$$[K^e] = \frac{AE}{L}\begin{bmatrix} l^2 & lm & ln & -l^2 & -lm & -ln \\ lm & m^2 & mn & -lm & -m^2 & -mn \\ ln & mn & n^2 & -ln & -mn & -n^2 \\ -l^2 & -lm & -ln & l^2 & lm & ln \\ -lm & -m^2 & -mn & lm & m^2 & mn \\ -ln & -mn & -n^2 & ln & mn & n^2 \end{bmatrix} \tag{3.26}$$

Hereby, the stiffness relationship in global coordinates for one bar element has been illustrated. After finishing assemblage of all members, the stiffness relationship of an entire PMFRC structure is obtained.

3.2.4. Stiffness matrix assemblage and force vectors

Equation 3.25 illustrates the relation between applied forces and resulting displacements along each axis, for one bar element in a 3D domain, with 2 nodes *i* and *j*

at bar ends. For stiffness in Equation 3.26, a more compact matrix form can be obtained for the single element through sub-matrix notation, with block matrices in terms of the two nodes in the end points of the bar segment. The matrix can be rewritten as:

$$[K^e] = \begin{bmatrix} K_{ii}^e & K_{ij}^e \\ K_{ji}^e & K_{jj}^e \end{bmatrix} \tag{3.27}$$

where K_{ii}^e is the 3×3 sub-matrix of stiffness components for node i and the size of the block-matrix represents the DOFs of nodes. Similarly, K_{jj}^e is the 3×3 sub-matrix of stiffness components pertaining to node j, and K_{ij}^e, K_{ji}^e are the stiffness matrices components related to both node i and node j. Therefore, when assembling all bar-elements into the entire structure, nodal displacements compatibility along the *x, y, z* axes at all nodes must be satisfied.

In order to acquire the assembled stiffness matrix $[K^a]$ for the entire PMFRC structure, a connectivity table is established by listing all node information for each bar element. When a node has multiple connections to different element members, its assemblage matrix of stiffness will be obtained by adding all submatrices related to this node. Eventually, shared nodes from the connectivity table would have the submatrix transposed to fit in assembly matrix $[K^a]$.

Beyond integrating the stiffness matrix for all bar elements, application of all loads to the force vector $\{F^e\}$ is essential. Similarly with the assembly of stiffness matrices, forces applied on the structure at the nodes must be distributed and merged into

x, *y* and *z* directions as 3 DOFs of each node in the 3D domain, which will finally transpose to the assemblage forces vector $\{F^a\}$.

3.2.5. Boundary conditions for nodal displacements and solutions

After the assemblage of structure stiffness and applied forces, all node displacement can be solved using Equation 3.28, where all factors assembled with all nodes feature together for the entire structure:

$$[K^a]\{U^a\} = \{F^a\} \tag{3.28}$$

where $\{U^a\}$ represents the nodal displacements, which are distributed correspondingly to the force vector $\{F^a\}$, namely, the nodal displacements in the *x*, *y* and *z* directions are identically in the same rows as the forces. There will always be 0 displacements on the $\{U^a\}$ because the whole structure cannot move as a rigid body through space, hence some nodes are used for anchoring the entire structure. Moreover, the process of bar element motion is set to happen on a rigid body, which means that the stiffness matrix $[K^a]$ is still a singular matrix temporarily, thus $\{U^a\}$ cannot be determined because the stiffness matrix $[K^a]$ cannot be inverted as its determinant is zero.

Therefore, restraints must be applied as boundary conditions. Correspondingly eliminating unknown rows and zero value columns, the system equation becomes non-singular. Unknows can be solved using the inverted matrix, with a unique solution obtained using the inverse of stiffness matrix multiplied by the force vector as $\{U\} =$

$[K]^{-1}\{F\}$. Eventually, the assemblage of nodal displacements vector $\{U^a\}$ is obtained by reintegrating the solutions and restraints to the boundary conditions. Consequently, all reactions including the external loads of vector force $\{F^a\}$ are determined using Equation 3.28.

3.2.6. Axial forces and nodal displacements transform

After $\{U^a\}$ is determined, the nodal displacements of each element can be found directly from the vector. Axial elongation, strains, stresses, and forces in each element can be computed from nodal displacements. For example, at element *e*, by combining its nodal displacements $\{U^e\}$ with rotation matrix $[T^e]$, the axial elongation $\{\delta\}$ is obtained as:

$$[T^e]^{-1}\{U^e\} = \{\delta\} \tag{3.29}$$

Since the material is assumed to be elastic, the axial strains and the axial forces are obtained by using Equation 3.3 of material properties. The last but very important point is that these element results acquired from the calculations must be checked against maximum allowable strain and yield stress in elastic unidirectional composites.

3.3. Chapter summary

This chapter introduces ideas about how interlacing structures can be optimized in an iterative way. On one hand, interlacing patterns are determined through structural

equilibrium; on the other hand, structural equilibrium is reached by minimizing strain energy. These are the two basic components in processing optimization loops. Taking advantage of SA algorithms, finding optimal values is done efficiently. It is especially important in complex cases with multiple interlacing points defined in 3D domains. Changing the tension combinations among the interlacing yarns, different dry yarn tensile trusses can be obtained. By applying FEA on the PMFRC structure with selected load cases, the entire parameters can be identified. Then, a second SA method is used on the tension combinations. After limited calculation loops, the structure is optimized.

Chapter 4. Case Studies

As discussed in Chapter 3, SA is employed for locating a function's optimum. The approach assumes that the steepest rise or decrease in a function at a particular point indicates the best direction for further search. When the difference in function outcome between subsequent iterations is sufficiently small, convergence occurs. After the dry textile truss reinforcement structure is optimized, PMFRC is obtained by combining with resin. FEA is then utilized for determining displacements at points of external load application, as well as internal stresses and strains. Results are then deployed in a structural SA optimization cycle. Structural SA incorporates both FEA analysis and equilibrium SA.

The specific stiffness of the PMFRC open structure part is improved for a certain loading scenario by looping dry yarn tensions, re-equilibrating, and re-assessing using FEA. In this early version of the concept, PMFRC segments running between two boundary points, contact points and/or interlacing points are treated as bars exposed to tension/compression solely; torsion and bending are not considered. In order to reduce deformations in the PMFRC structure under load, all structures are triangulated, and all bars form tetrahedra.

In Chapter, 4 different structures are modelled, starting with the simplest open structure, and culminating with a more complex structure mimicking a part within the boundaries set for the modelling method. All cases aim at demonstrating the stiffness optimization scheme. An optimized open truss interlaced composite structure with different internal geometry may be obtained by changing external yarn tensions within

the same part envelope. The stiffness of the part obtained through consolidation of the dry yarn into a PMFRC is analysed through FEA as described above.

4.1. Example 1: case of 1 interlacing point

Example 1 is a simple 3D structure featuring 3 yarns and 1 interlacing point. All yarns may be subjected to different tensions so that the position of the interlacing point may be altered accordingly. Example 1 is defined within a cube with arbitrary 10 cm side length, Figure 4.1.

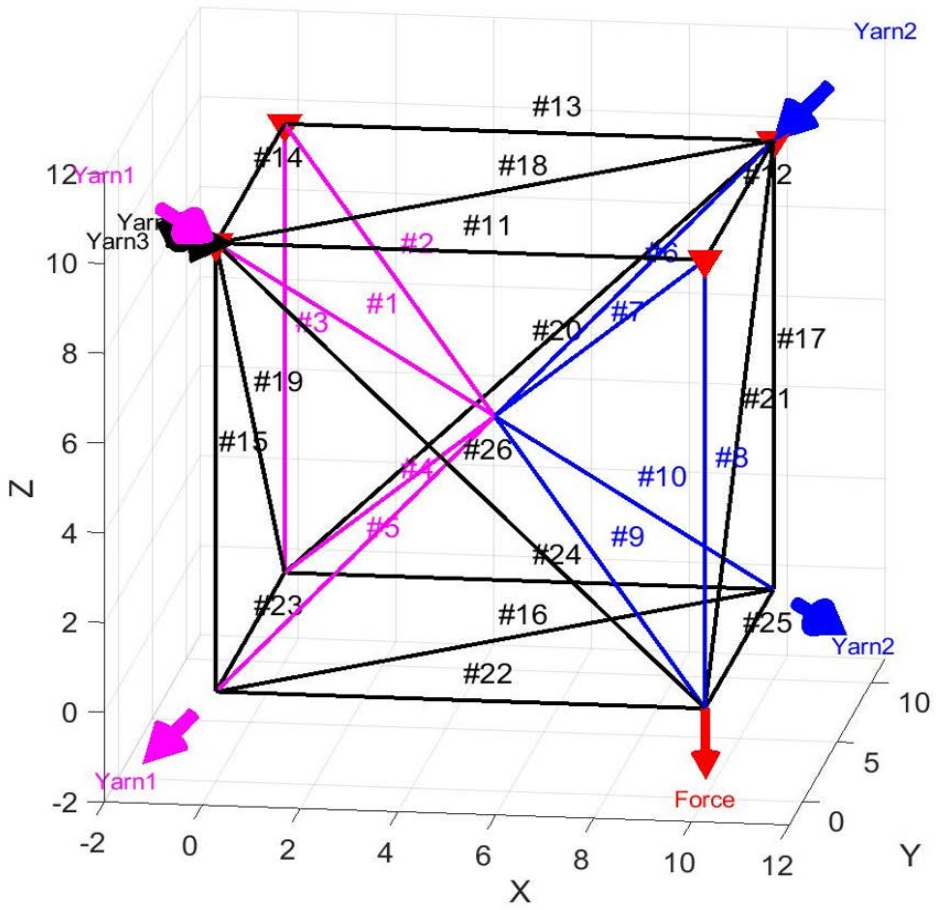

Figure 4.1. Interlacing diagram for pre-equilibrium 3D structure example 1 featuring 3 yarns and 1 interlacing point

The structure is made from 3 continuous yarns shown in magenta (yarn 1), blue (yarn 2) and black (yarn 3), extending uninterrupted as yarn segments #1-5, #6-10 and #11-26. Entry and exit points of the yarns, where tension is applied, are shown by coloured arrows. Specific paths for the yarns were selected manually and arbitrarily with the only imperative of producing a continuous and fully triangulated structure with stable interlacing points.

The structure is delimited by 12 vertices #3, #8, #11-15, #17, #22-25 corresponding to the edges of the cube and part envelope. This is anecdotal to this case - no hard requirement is set on external vertices of the envelope beyond triangulation of the resulting PMFRC structure. In its initial, pre-equilibrium and non-optimized configuration, the one interlacing point within the envelope is positioned arbitrarily at the centre of the domain, leading to 8 diagonal yarn segments #1, #2, #4-7, #9, #10 interlacing. The domain within the part envelope is divided into 6 pentahedra, each one then divided into 2 tetrahedra for triangulation, leading to 12 tetrahedra with identical dimensions in their initial configuration.

The loading case was set arbitrarily by anchoring the ends of all 4 vertices in the upper plane, marked by 4 red triangles, and applying a vertical downward 50 N force in the lower right corner (x = 10, y = 0). Assuming very small bars loaded in tension only and with very small interlacing points in the calculations, all forces equilibrate at a point in an interlacing point, and so the bar sections need to be very small. Therefore, bar stiffness and bar section were set at 100E9 $\mathrm{N/m^2}$ and 1E-8 $\mathrm{m^2}$, which were the default setting for all cases in this project.

Initial tensions were all set to 10 N pre-optimization, leading to a central interlacing point (x = 5, y = 5, z = 5), Figure 4.2 a). The dotted lines show the initial structure whilst the coloured continuous lines show the deformed structure under load. Anecdotally, this is the same position as the initial position decided arbitrarily for this simple case; to be clear, the position stays the same post-equilibrium hence post steepest ascent, but pre-optimization of yarn tensions towards increasing structure stiffness. Applying the force leads to a pre-optimization vertical displacement of 0.3995 cm at the point of application of the force, with the largest tension in bar #8 reaching approximately 40 N.

Steepest ascent optimization for stiffness leads to tensions in yarns 1 and 2 equal to 5 N and 15 N respectively, the upper-lower ratio of 3 being set as a limit on processing time since beyond that point, much smaller displacements consume much more time. Results appear in Figure 4.2b). Vertical displacement at the point of application of the force was 0.3897 cm, with largest tension in bar #8 slightly reduced to approximately 39 N. In this case, displacement was reduced by 2.51% for an increase in structure mass of 1.07%, hence light improvements in both structural stiffness and specific structural stiffness, Table 4.1.

Table 4.1. Pre-and post-optimization displacements and bar lengths, example 1

	Initial, pre-optimization	Optimized	Δ
Applied load	50 N	50 N	
Displacement (cm)	0.3995	0.3897	-2.45%
Total bar length (cm)	274.3	277.3	+1.15%

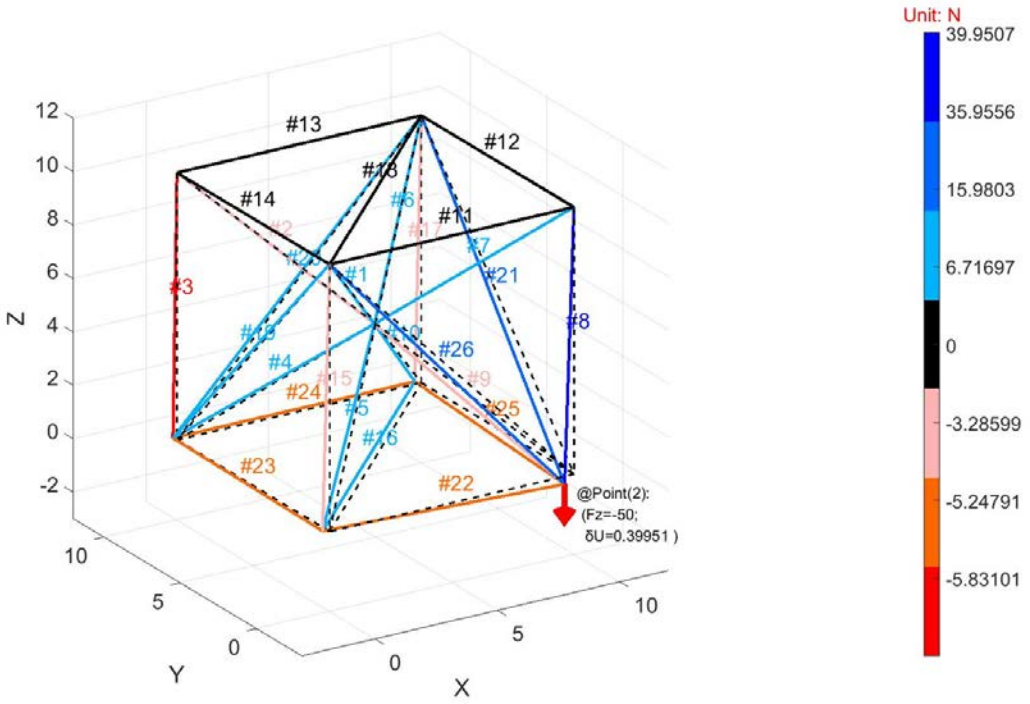

(a)

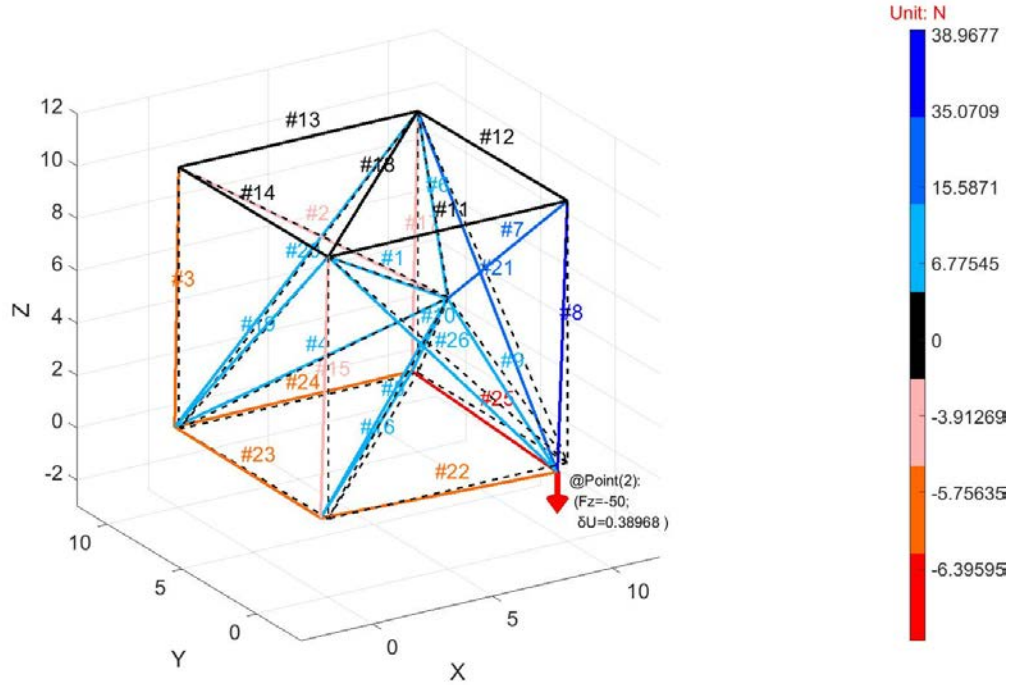

(b)

Figure 4.2. Displacements and force distribution in non-optimized (a) and optimized (b) trusses, example 1

Improvements gained through optimization are very limited in this case, for two reasons. Firstly, bar #8 extends between the point of application of the force and one anchoring point along the line of action of the force, and bar #21 extends in a plane defined by the line of action of the force and two anchoring points. Consequently, contributions to stiffness from other bars are minimal for this simple load case and structure. Secondly, the ratio of yarn tensions was artificially limited in order to replicate similar restrictions that are likely to arise in actual manufacturing. Overall, these factors limit possible displacement of the interlacing point.

4.2. Example 2: case of 2 interlacing points

Example 2 is defined as two similar cubes with arbitrary 10 cm side length, Figure 4.3 a). The structure is made from 4 continuous yarns shown in magenta (yarn 1), blue (yarn 2), black (yarn 3) and red (yarn 4) extending uninterrupted as yarn segments #1-10, #11-20, #21-34 and #35-47. All yarn paths were selected manually, targeting a fully triangulated structure with stable interlacing points as in example 1. It must be noted that over segment #32, black yarn 3 and red yarn 4 overlap, with doubled stiffness over this segment.

The structure is delimited by 16 vertices #3, #8, #13, #18, #21-24, #30, #34-38, #44, #47 corresponding to the edges of the part envelope. In its initial, pre-equilibrium and non-optimized configuration, the two interlacing points are positioned arbitrarily at the centres of the cubes, leading to 16 diagonal yarn segments #1-2, #4-7, #9-12, #14-17, #19-20 interlacing. The domain within the part envelope is divided into 12 pentahedra,

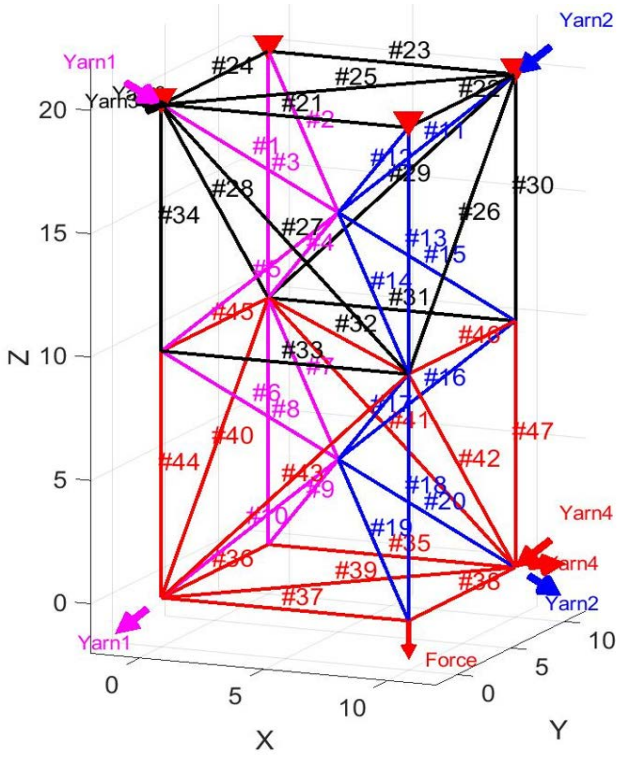

(a)

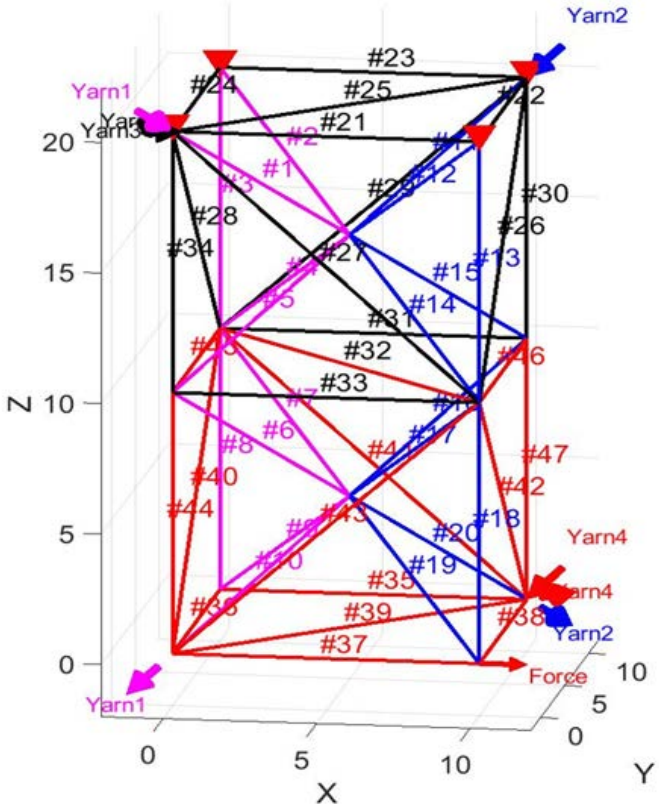

(b)

Figure 4.3. Interlacing diagram for pre-equilibrium 3D structure example 2 featuring 4 yarns and 2 interlacing point2 for (a) load case 1 and (b) load case 2

each one then divided into 2 tetrahedra for triangulation, leading to 24 tetrahedra with identical dimensions in their initial configuration.

Two load cases were probed. Load case 1 was set arbitrarily by anchoring the ends of all 4 vertices in the upper place, marked by 4 red triangles, and applying a vertical downward 50 N force in the lower right corner ($x = 10$, $y = 0$).

4.2.1. Example 2, load case 1

Initial tensions were all set to 10 N pre-optimization leading to two central interlacing points distributed in each cube at ($x = 5$, $y = 5$, $z = 5$) and ($x = 5$, $y = 5$, $z = 15$) respectively, Figure 4.4 a). These positions are post-equilibrium but pre-optimization. The force leads to a pre-optimization vertical displacement of 0.7917 cm at the point of application of the force, with the largest tension in bar #18 reaching approximately 45 N.

Steepest ascent optimization for stiffness leads to tensions in yarns 1 and 2 equal to 5 N and 15 N respectively, artificially limited to 1:3 as explained for example 1, Figure 4.4 b). Displacement is reduced to 0.7511 cm, and the largest tension found in truss #18 is deduced to 42 N. Overall, displacement was reduced by 5.41% and length increased by 1.22%, as shown as Table 4.2. It should be noted that the change in length is not the same as seen in example 1.

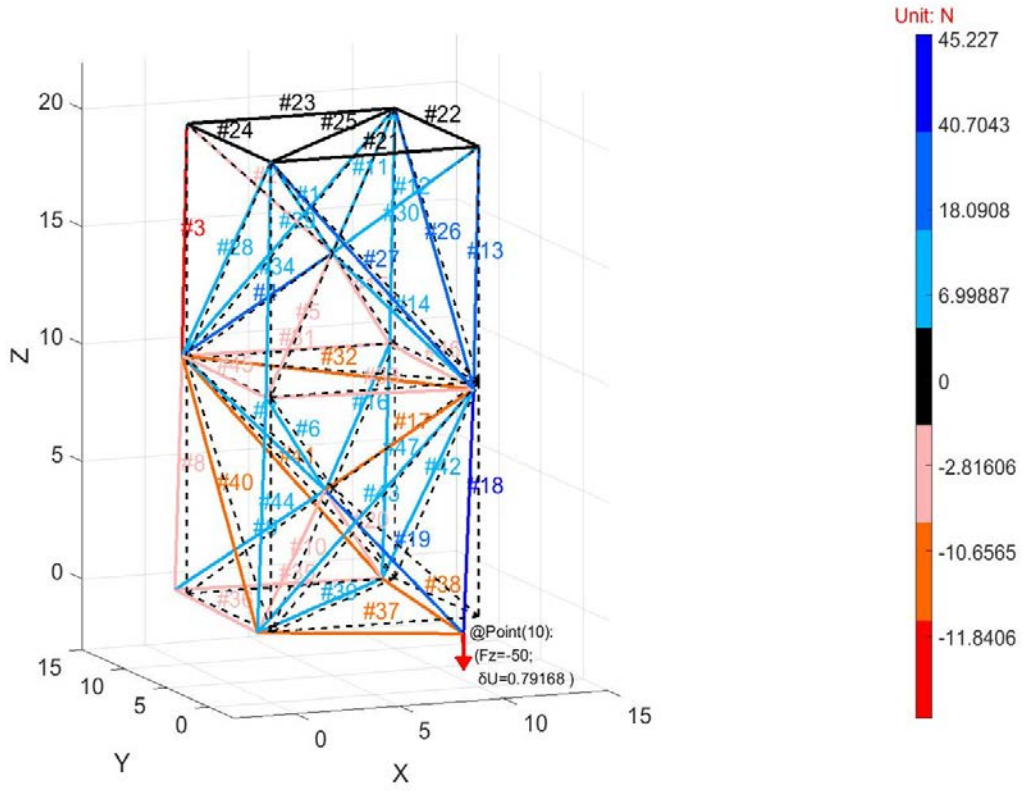

(a)

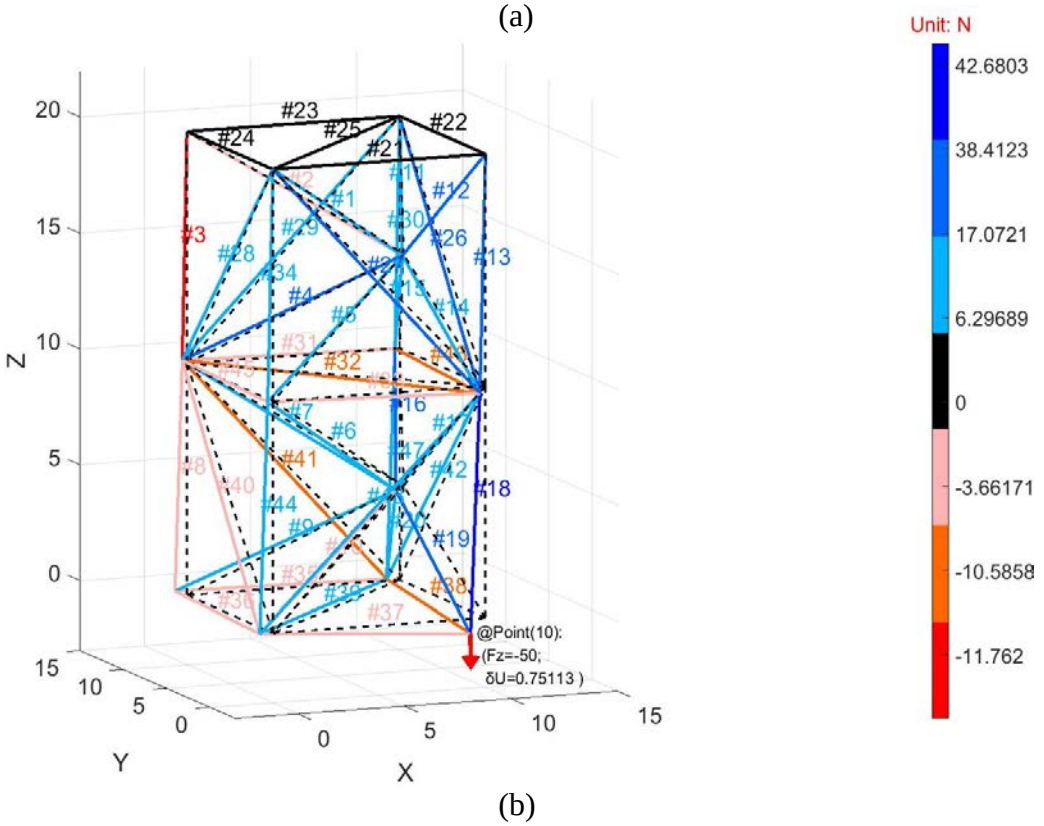

(b)

Figure 4.4. Displacements and force distribution in non-optimized (a) and optimized (b) trusses, example 2

Table 4.2. Pre-and post-optimization displacements and bar lengths, example 2, load case 1

	Initial, pre-optimization	Optimized	Δ
Applied load	50 N	50 N	
Displacement (cm)	0.7917	0.7511	-5.12%
Total bar length (cm)	508.3	514.5	+1.22%

4.2.2. Example 2, load case 2

Load case 2 is similar to the above with the force applied horizontally along the positive direction of axis *x*, Figure 4.3 b). Initial tensions were similarly set to 10 N pre-optimization, Figure 4.5 a), leading to a horizontal displacement of 2.9838 cm at the point of force application, with the largest tension in bar #3 reaching approximately 39 N.

Structural optimization was performed as described above, Figure 4.5 (b). Horizontal displacement was reduced to 2.8016 cm, and the largest tension in bar #3 reduced to 35 N. Overall, displacement reduced by 6.10% for an increase in total yarn length of 1.22%, Table 4.3.

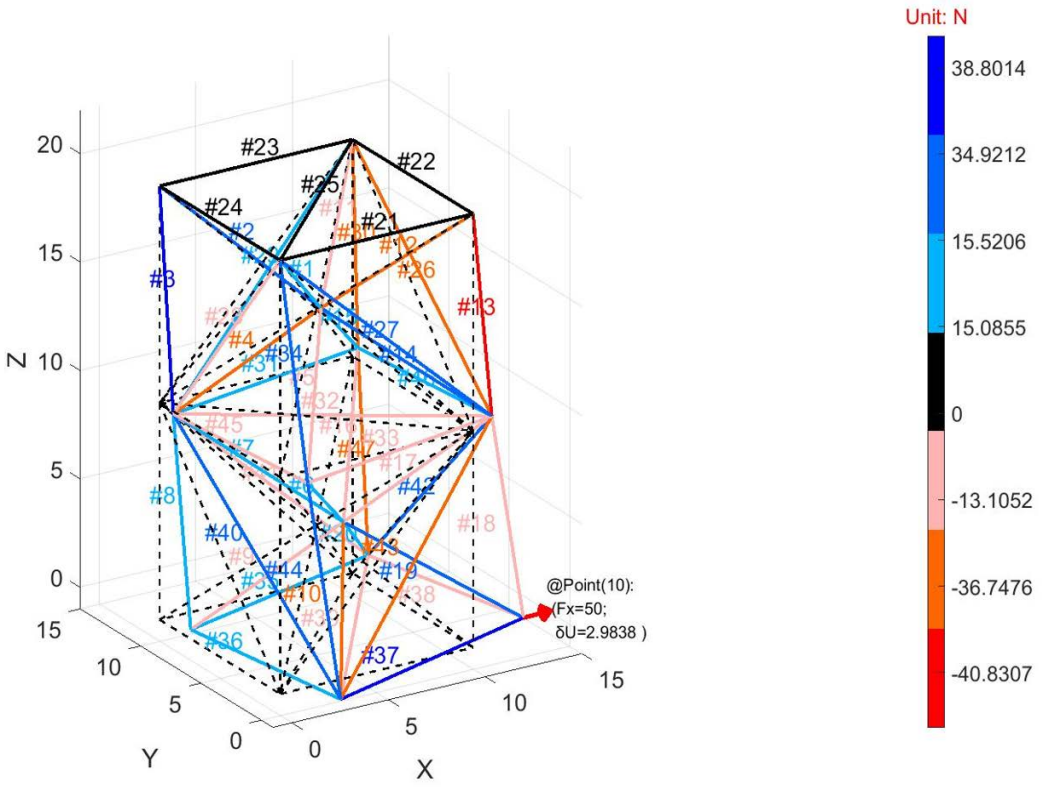

(a)

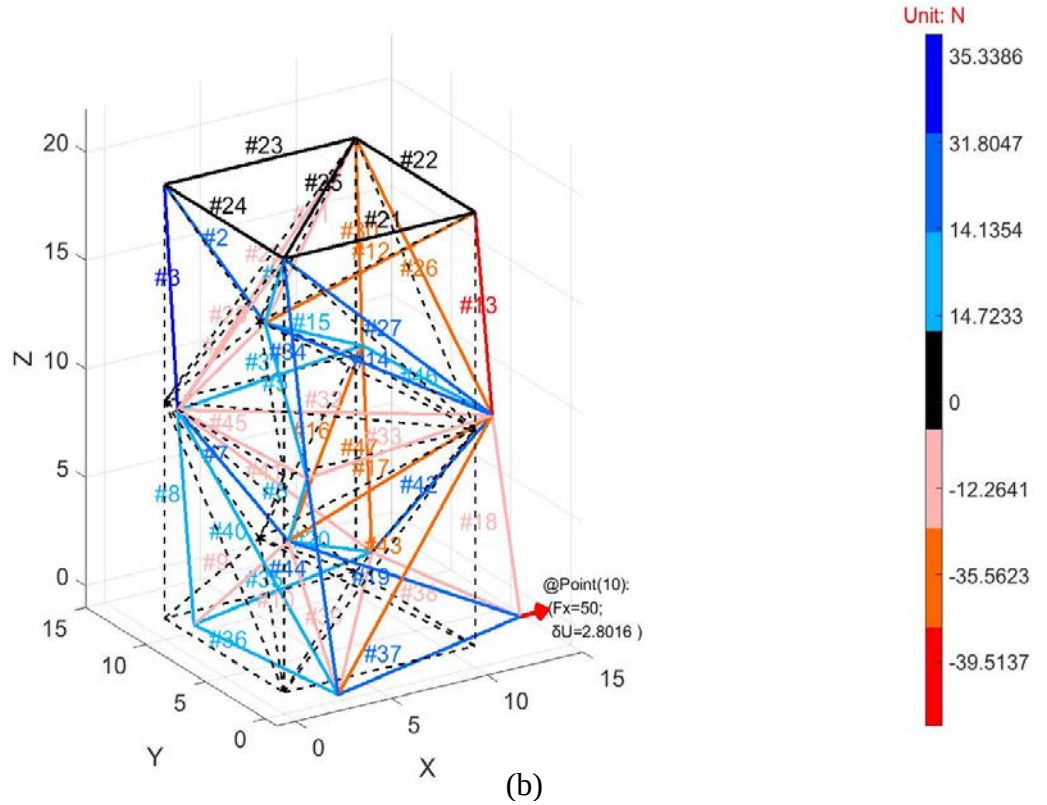

(b)

Figure 4.5. Displacements and force distribution of 2-interlacing-point case in horizontal loads in non-optimized (a) and optimized (b) trusses

Table 4.3. Pre-and post-optimization displacements and bar lengths, example 2, load case 2

	Initial, pre-optimization	Optimized	Δ
Applied load	50 N	50 N	
Displacement (cm)	2.9838	2.8016	-6.10%
Total bar length (cm)	508.3	514.5	+1.22%

Although example 2 features what remains a simple structure, improvements in stiffness and specific stiffness were larger than those obtained for example 1. These improvements are limited but not negligible, despite limitations imposed on tension ratios.

4.2.3. Example 2, further optimized solution cases 3 and 4

Example 2 can be optimized further as the structure features more points that are available to move, including points defined on boundaries. Such point displacements may be limited arbitrarily to positions that make no changes to the initial volume envelope and maintain its dimensions, as for case 3. Alternatively, movement may be allowed for some points defining the envelope, as for case 4. Both examples feature the vertical load case seen previously in case 1, and all boundary conditions are maintained except for allowing boundary points in the horizontal mid-plane to move along limited directions (case 3) or limited orthogonal planes (case 4). Better optimized results will be obtained, depending on allowed directions or planes where boundary points may move.

In optimization case 3, movement is allowed for boundary points defined in the middle plane, marked as points *A, B, C, D* in Figure 4.6 a). These points may move along the *z* axis only. Final optimized displacement was reduced to around 0.7166 cm, the largest tension found in truss #18 was more than 46 N. Movements of the boundary points along *z* can be observed clearly as the upper proportion of the entire structure is larger that the lower proportion. Overall, displacement was reduced by 9.49% and length increased by 1.60%, Table 4.4.

Table 4.4. Pre-and post-optimization displacements and bar lengths, example 2, case 3, load case 1

	Initial, pre-optimization	Optimized-case 3	Δ
Applied load	50 N	50 N	
Displacement (cm)	0.7917	0.71655	-9.49%
Total bar length (cm)	508.3	516.4	1.60%

In case 4, with all other conditions kept the same, changes pertaining to the boundary points from case 3 were such that 2 points *A* and *C* could move only along *z*, however the 2 points *B* and *D* were allowed to move along the *x* and *y* axes respectively. As a result, displacement was drastically reduced to around 0.5869 cm, and the largest tension found in truss #18 dropped to around 37 N, Figure 4.6 b). Even though the motions of middle-plane points changed the outlines of the part envelope, overall displacement decreased by 25.87% whilst length increased by only 0.42%, Table 4.5.

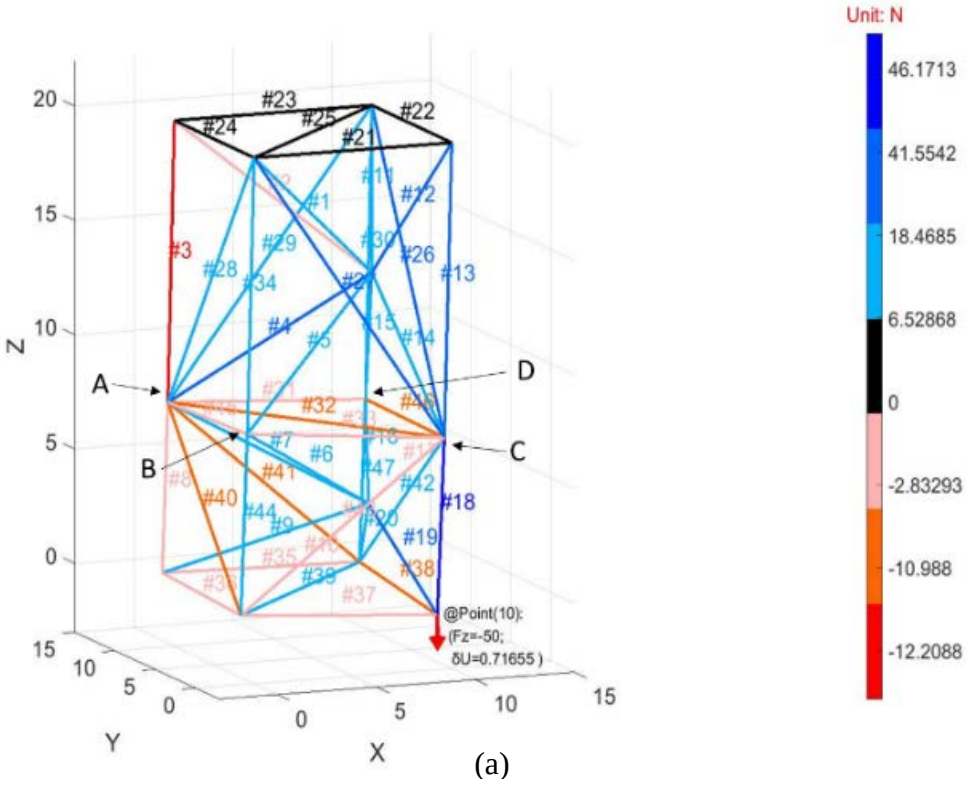

(a)

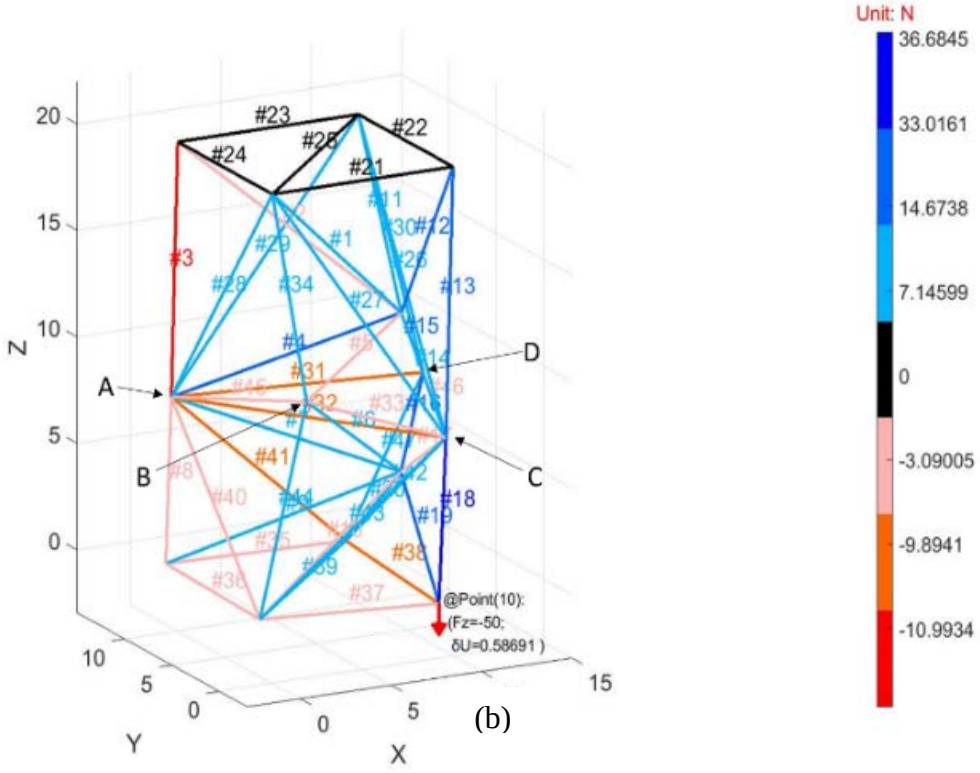

(b)

Figure 4.6. Displacements and force distribution after optimization for case 3 (a) and case 4 (b)

Table 4.5. Pre-and post-optimization displacements and bar lengths, case 4 of example 2, load case 1

	Initial, pre-optimization	Optimized-case 4	Δ
Applied load	50 N	50 N	
Displacement (cm)	0.7917	0.58691	-25.87%
Total bar length (cm)	508.3	510.4	0.42%

It is worth mentioning that imparting additional degrees of freedom to boundary or contact points may not always be advantageous; in some situations of free movement of points in the *x*, *y* and/or *z* directions, the outcome could be poorer than when these DOF are fixed. The main issue is that when DOFs of boundary points are not limited, then these boundary points will be allowed to move around freely in the spatial volume under strain. In such instances, many points including boundary points and interlacing points, will possibly end up in the same positions whilst calculations can still meet all the SA requirements, irrespective of how unfavourable the structure envelope may be. Alternatively, additional interlacing or crossing that were not included in the initial design could appear unintentionally and without being correctly managed. The volume size or interlacing configurations may not be maintained, as many points are jointed in the same position, potentially causing the collapse of the entire structure under external loads.

4.3. Example 3: hinge-like part

After exploring the above examples, one additional attempt at a somewhat more realistic part inspired by the AM hinge shown in Figure 4.7 is introduced as example 3. Even though interlacing is again predefined arbitrarily, the cases display the capability to produce good optimization results in terms of structural stiffness combined with contained mass. Example 3 was designed and optimized in two different forms in terms of the internal structure and interlacing patterns, labelled regular interlacing and arbitrary interlacing respectively.

Figure 4.7. Metal AM parts 3D printed for European Space Agency [120]

Figure 4.7 shows AM hinges with 3 different internal patterns, developed at the European Space Agency. At the top left is the original metal part manufactured by casting, with high mass. Taking advantage of TO and AM technologies, these metal parts become capable to match stiffness requirements with a decreasing weight. The objective of example 3 is to design a simple hinge-like part with a generally similar outline, then

optimise the structure for selected load cases. Unlike prior examples, example 3 was conducted using 2 different interlacing patterns as well as 2 different load cases.

4.3.1. Example 3, regular interlacing, load case 1

Case 1 of example 3 with regular interlacing is defined by 4 similar cubes and 2 similar triangular prisms with arbitrary 10 cm side length, Figure 4.8. The structure is made from 7 continuous yarns shown in magenta (yarn 1), blue (yarn 2), green (yarn 3), red (yarn 4) and cyan (yarn 5) as well as peripheral yarn 6 and yarn 7 in black. Corresponding to the yarn sequence, the bar segments #1-10, #11-20, #21-30, #31-40, and #41-44 are for the yarns 1-5 respectively, which are used for optimizing interlacing under different combinations of tensions. Segments #45-87, #88-105 are for yarn 6 and yarn 7, which are merely used for connecting all points and make up the outline of the entire volume. The structure is delimited by 21 vertices, and the segments in black connect all the vertices corresponding to the edges of the part envelope.

In its initial, pre-equilibrium and non-optimized configuration, there are 6 interlacing points positioned arbitrarily at the centres of the cubes and triangles, leading to a total of 44 diagonal yarn segments #1-44 interlacing. The domain within the part envelope is divided into 32 pentahedra, each one then divided into 2 tetrahedra for triangulation, leading to 64 tetrahedra with identical dimensions in their initial configuration.

Dimensions of the structure are 30 cm along the *x* axis, 20 cm along the *y* axis and 10 cm along the *z* axis, the load case was set up arbitrarily by anchoring the starts of all 6 vertices in the top *y*-*z* plane, marked by 6 red triangles, and applying a vertical

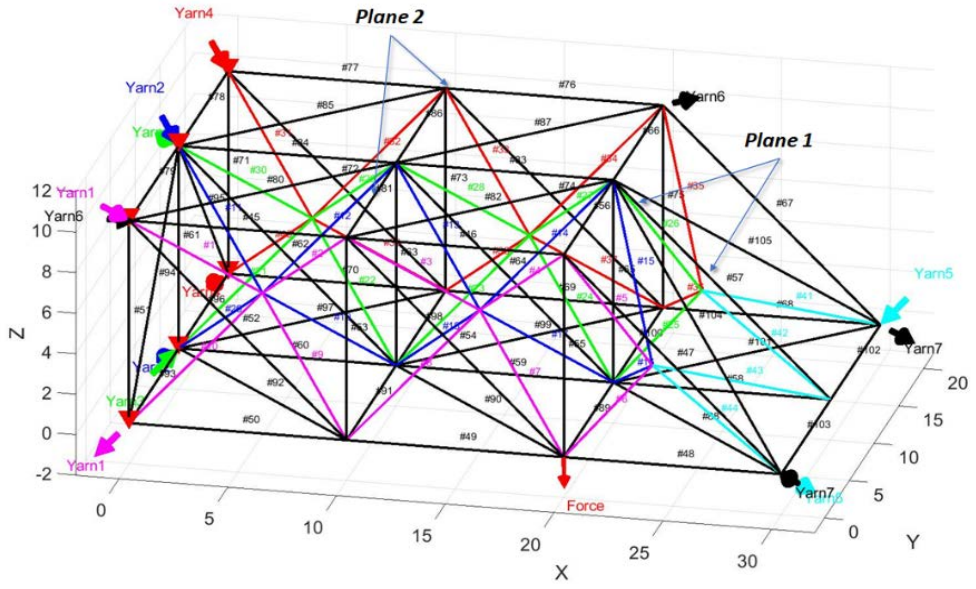

Figure 4.8. Interlacing diagram for pre-equilibrium 3D structure example 3 featuring 7 yarns and 6 interlacing points

downward 50 N force in the lower right corner (x = 20, y = 0). Bar stiffness and bar section were the same as in previous cases.

Initial tensions were all set to 10 N pre-optimization leading to central interlacing points distributed in each cube, Figure 4.9 a). These positions are post-equilibrium but pre-optimization. The forces lead to a pre-optimization vertical displacement of 2.4163 cm at the point of application of the force, with the largest tension in bar #54 reaching approximately 27 N.

Applying SA optimization for stiffness lead to tensions in yarns 1-5 equal to 15 N, 5 N, 15 N, 5 N and 5 N respectively; all yarn tensions were pushed to the maximum and minimum boundaries artificially imposed, Figure 4.9 b).

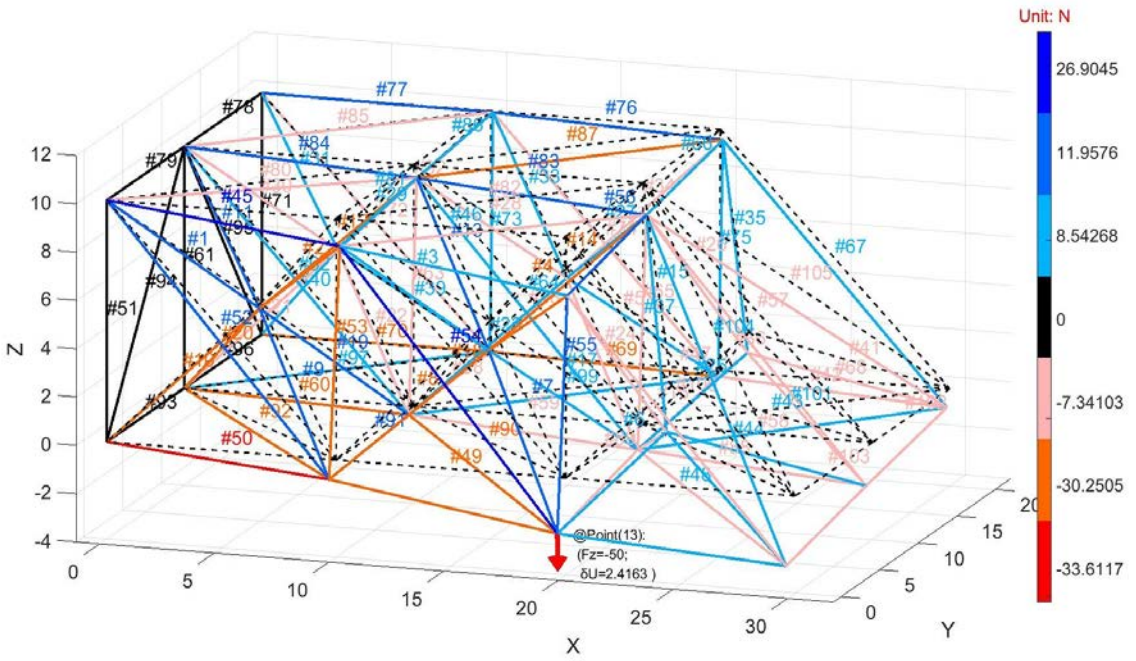

(a)

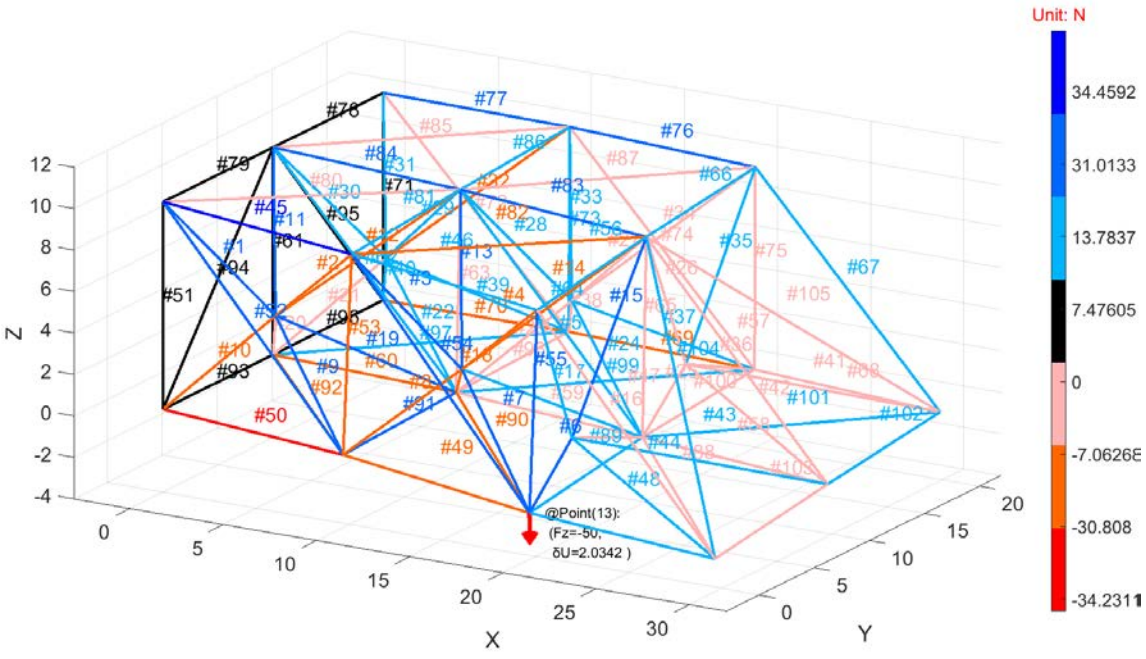

(b)

Figure 4.9. Displacements and force distribution in non-optimized (a) and optimized (b) trusses, example 3

Structural redistribution caused by tension changes reduced displacement to 2.1071 cm. The largest tension was transferred to bar #45, with the force increased to about 41 N. Overall, displacement was reduced by 12.80% and length increased by 1.86%, Table 4.6.

Table 4.6. Pre-and post-optimization displacements and bar lengths, example 3, load case 1

	Initial, pre-optimization	Optimized-case1	Δ
Applied load	50 N	50 N	
Displacement (cm)	2.4163	2.0342	-15.80%
Total bar length (cm)	1087.8	1108.1	1.86%

4.3.2. Example 3, regular interlacing, load case 2

Similar to example 2, better optimization can be expected by freeing contact points in specific directions, including points on the outline. Here, the movements enabled have no effect on part dimensions prior to loading; part envelope is unchanged.

Case 2 was based on the same load as case 1. All conditions were kept identical, except for allowing all boundary points in the middle plane 1 that extends parallel to the *y*-*z* plane to move along the *x* direction only, and for allowing all boundary points in the middle plane 2 that extends parallel to the *z*-*x* plane to move along the *y* direction only. Planes 1 and 2 are identified in Figure 4.8. After applying SA optimization for stiffness,

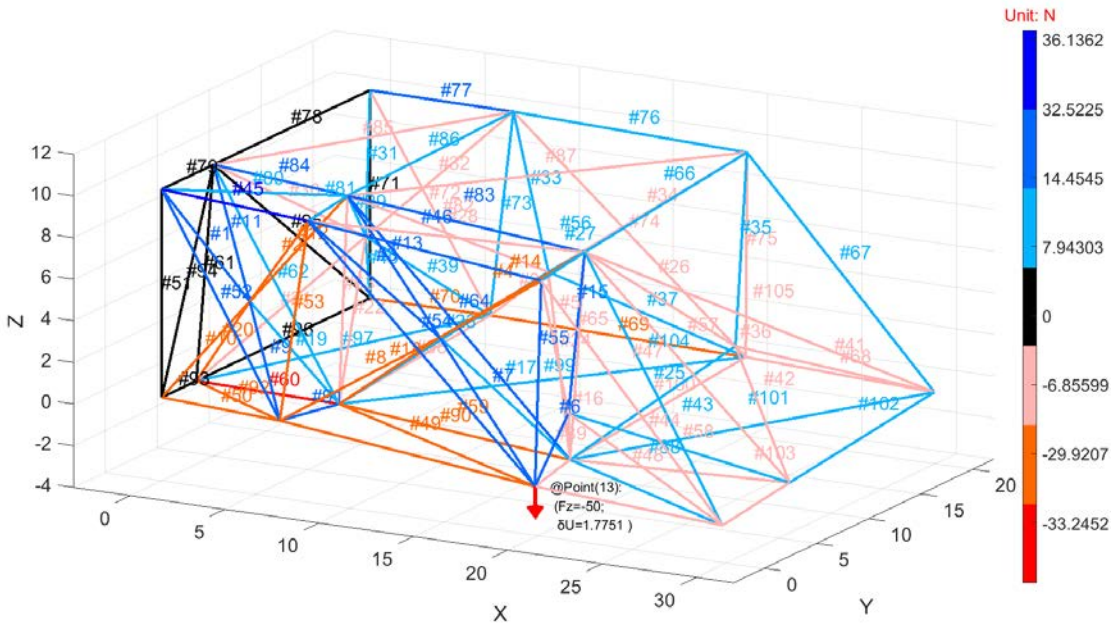

Figure 4.10. Displacements and force distribution in optimized trusses, example 3, case 2, load case 1

all yarn tensions were pushed to the maximum and minimum boundaries with a tension combination of 15 N, 15 N, 5 N, 5 N and 5 N respectively from yarns 1 to yarn 5, Figure 4.10. Displacement was reduced to 1.7751 cm, and the largest tension was found on bar #45, but the force had increased to about 36 N. Overall, displacement in the component was reduced by 26.54% and length increased by 2.47%, Table 4.7.

Table 4.7. Pre-and post-optimization displacements and bar lengths, example 3, load case 2

	Initial, pre-optimization	Optimized-case2	Δ
Applied load	50 N	50 N	
Displacement (cm)	2.4163	1.7751	-26.54%
Total bar length (cm)	1087.8	1114.7	2.47%

4.3.3. Example 3, regular interlacing, load case 3

As opposed to the regular component of case 2 where the loading point was (x = 20, y = 0), the loading point for case 3 was at location (x = 30, y = 0), Figure 4.11. Case 3 is also based on case 2, where the 6 boundary points on the top left y-z plane are anchored, marked by 6 red triangles. All conditions were kept the same, except for allowing all boundary points in middle plane 1 that extends parallel to the y-z plane to move along the x direction only and making all boundary points in middle plane 2 that extends parallel to the z-x plane to move along the y direction only. Planes 1 and 2 are identified in Figure 4.8. In comparison with the hinge-like part with arbitrary interlacing paths, the last case with the irregular patterns is introduced in the following as load case 4 and 5.

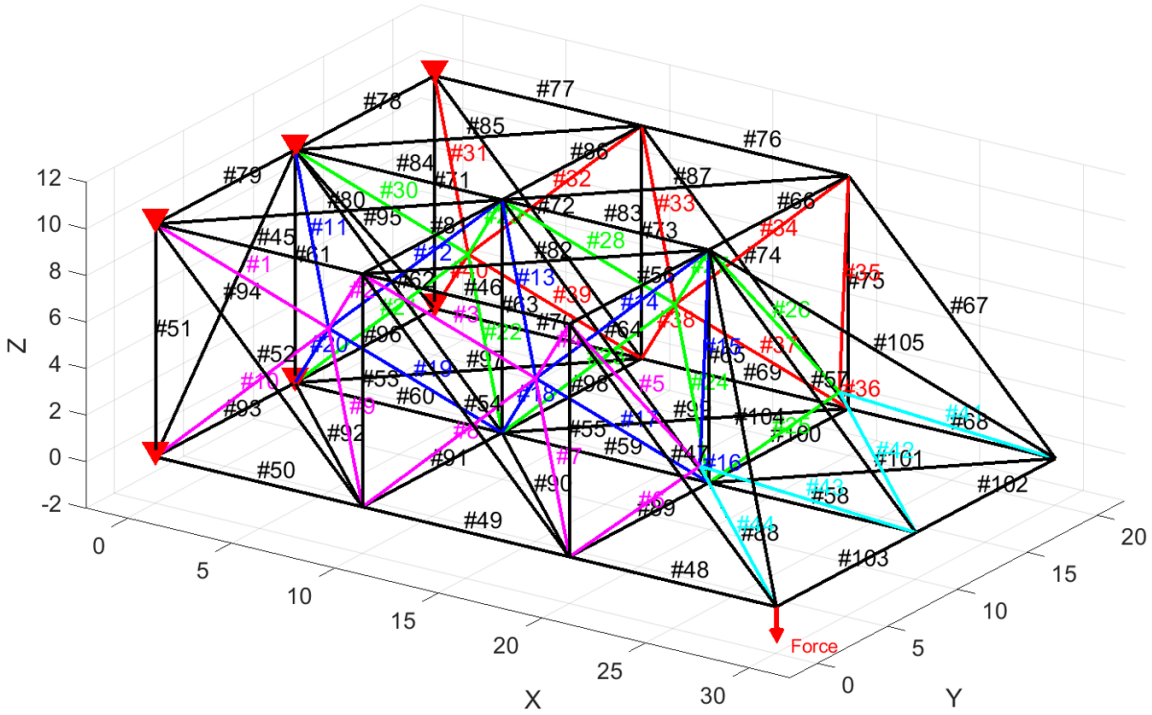

Figure 4.11. Interlacing diagram for pre-equilibrium 3D structure example 3 featuring 7 yarns and 6 interlacing points, load case 3

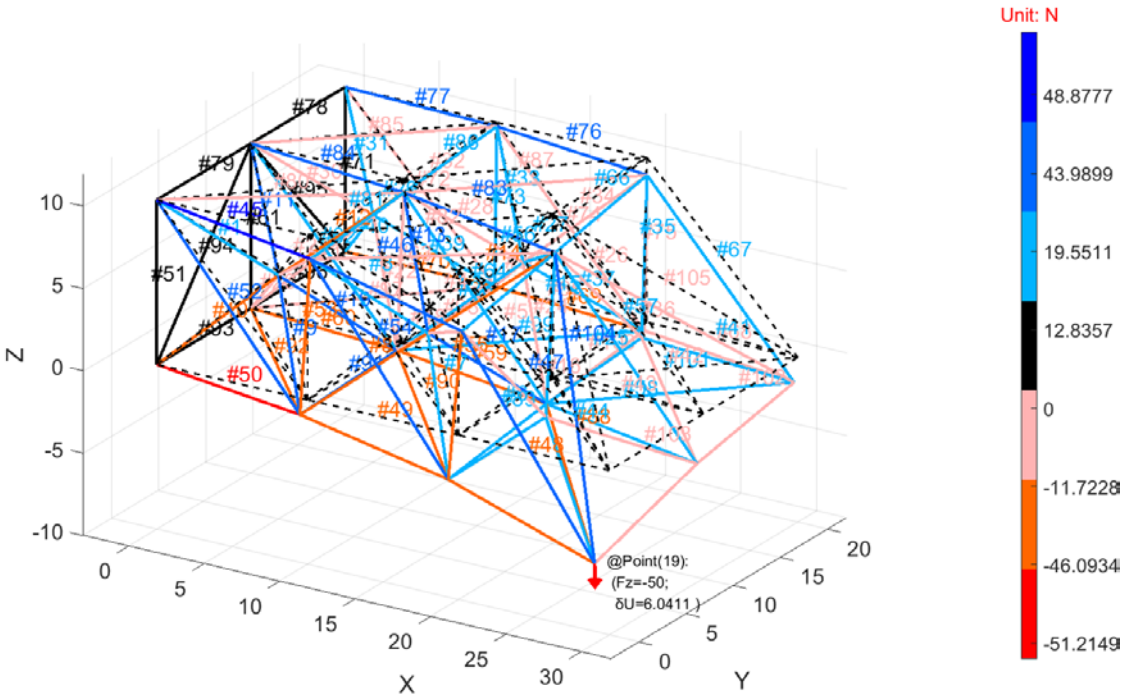

(a)

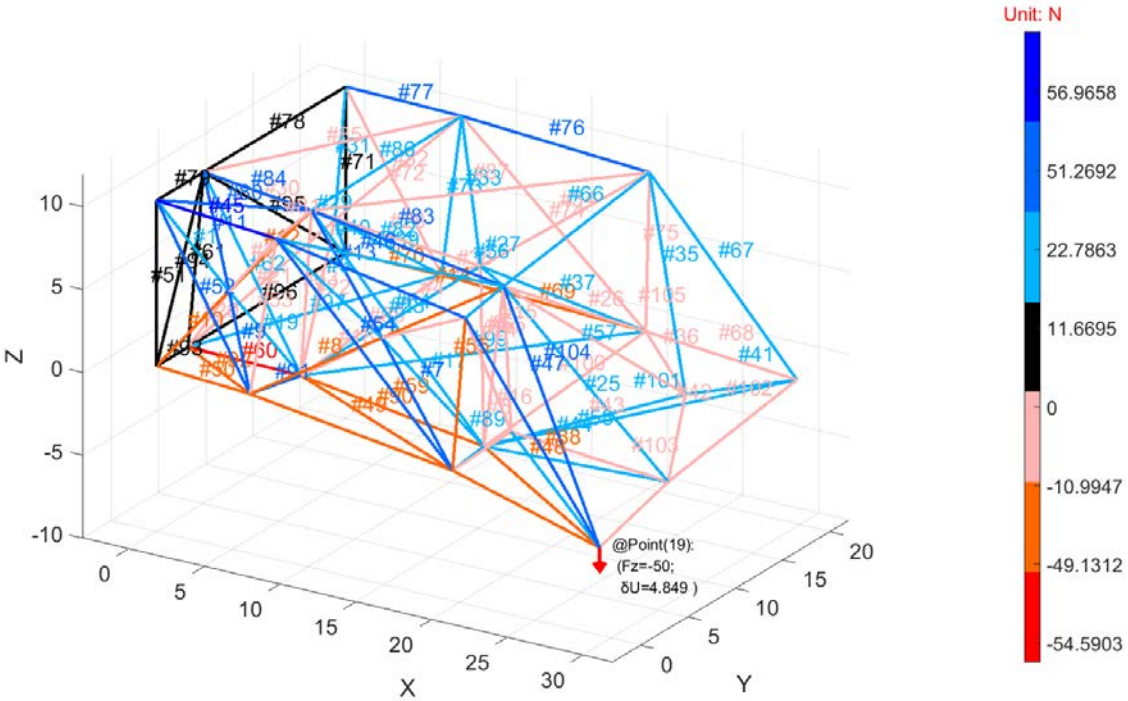

(b)

Figure 4.12. Displacements and force distribution in optimized trusses, example 3, case 3, load case 3

To compare with the arbitrary pattern, initial tensions in case 2 were all set to 10 N pre-optimization, leading the continuous yarns to make the interlacing points distributed in the centre of each cube, Figure 4.12 a). These positions are post-equilibrium but pre-optimization. The applied load lead to a pre-optimization vertical displacement of 6.0411 cm at the point of application of the force, and the largest tension in bar #45 reached approximately 49 N.

SA optimization for stiffness lead to tensions in yarns 1-5 equal to 15 N, 15 N, 5 N, 5 N and 15 N respectively; all yarn tensions reached the maximum and minimum imposed boundaries, Figure 4.12 b). Displacement was reduced to 4.849 cm and the largest tension was found on bar #45 whilst the force increased significantly to about 57 N. Displacement was reduced by 19.73% and length increased by 2.69%, Table 4.10.

Table 4.8. Pre-and post-optimization displacements and bar lengths, example 3, load case 3

	Initial, pre-optimization	Optimized-case3	Δ
Applied load	50 N	50 N	
Displacement (cm)	6.0411	4.849	-19.73%
Total bar length (cm)	1087.8	1117.1	2.69%

4.3.4. Example 3, arbitrary interlacing, load case 4

When compared with hinge-like parts with regular interlacing, the arbitrary pattern, Figure 4.11, makes the hinge-like component look more open. Case 4 of example

3 with arbitrary interlacing was defined within the same outer envelope as for regular interlacing. Dimensions are 30 cm along the *x* axis, 20 cm along the *y* axis and 10 cm along the *z* axis, as shown in Figure 4.13.

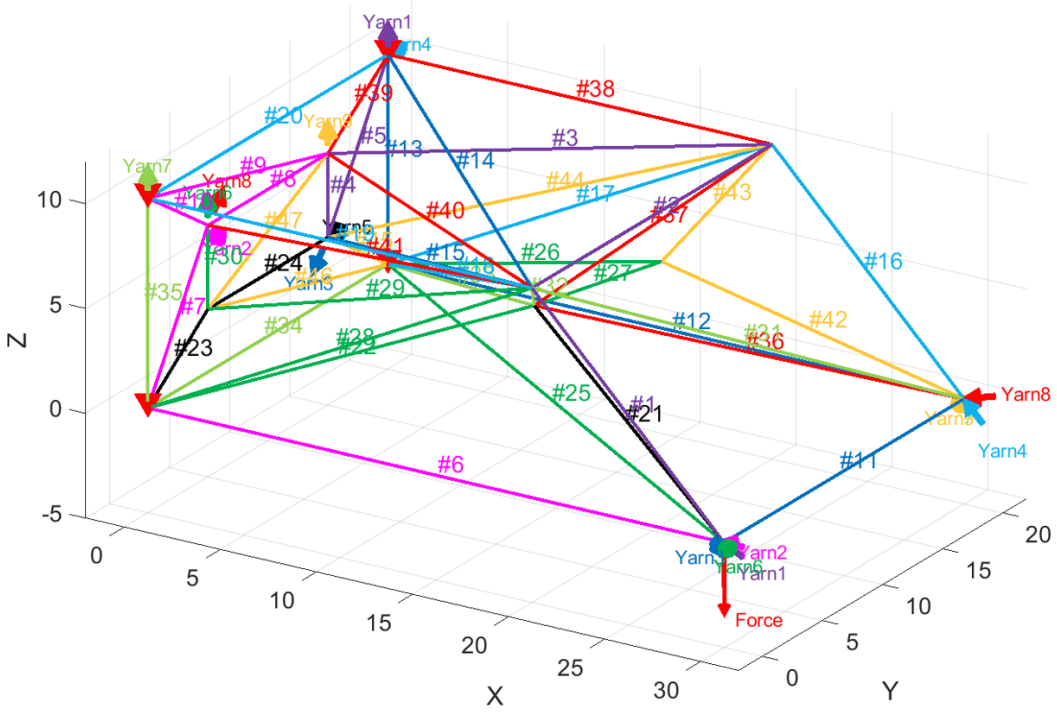

Figure 4.13. Interlacing diagram for pre-equilibrium 3D structure example 3 featuring 7 yarns and 6 interlacing points, load case 4

The structure is made from 9 continuous yarns shown in purple (yarn 1), magenta (yarn 2), blue (yarn 3), cyan (yarn 4), black (yarn 5), green (yarn 6), neon (yarn 7), red (yarn 8) as well as yellow (yarn 9). Corresponding to yarn sequence, bar segments #1-5, #6-10, #11-15, and #16-20 are for yarns 1-4 respectively, which are not connected with any interlacing point, and are merely used for connecting all points and for making up the outline of the entire volume. Segments #21-24, #25-31, #32-36, #37-42, and #43-48

are for yarn 5 to yarn 9 coordinately, which are used for determining the interlacing patterns through different combinations of tensions. The differences from example 3 with regular interlacing are as follows:

a) interlacing paths are arbitrarily determined, and overlap over 2 segments, where material properties were doubled.

b) the structure is delimited by 12 vertices and 2 interlacing points, whilst the structure with regular interlacing featured 21 vertices and 6 interlacing points.

Due to these differences, the component with arbitrary interlacing has significantly less yarn length. Also, the loading point on the arbitrary structure had to be moved to the right end tip ($x = 30$, $y = 0$) as shown in Figure 4.13. The case of the regular pattern of example 3 undergoing load case 3 will be used for making comparisons.

The 4 vertices in the top left *y*-*z* plane marked by 4 red triangles were anchored, and a vertical downward 50 N force was applied at the loading point. Bar stiffness and bar section were the same as in previous cases. Initial yarn tensions were all set to 10 N pre-optimization leading to central interlacing points distributed in each cube, Figure 4.14 a). The positions are post-equilibrium but pre-optimization. The applied load led to a pre-optimization vertical displacement of 9.9837 cm at the point of application of the force, with the largest tension in bar #19 reaching approximately 89 N.

SA optimization for stiffness lead to tensions in yarns 5-9 equal to 15 N, 15 N, 5 N, 5 N and 5 N respectively; all yarn tensions were pushed to the maximum and minimum imposed boundaries, Figure 4.14 b). Even though structural redistribution was made with different tensions, displacement reduced slightly to 9.5422 cm. The largest tension was

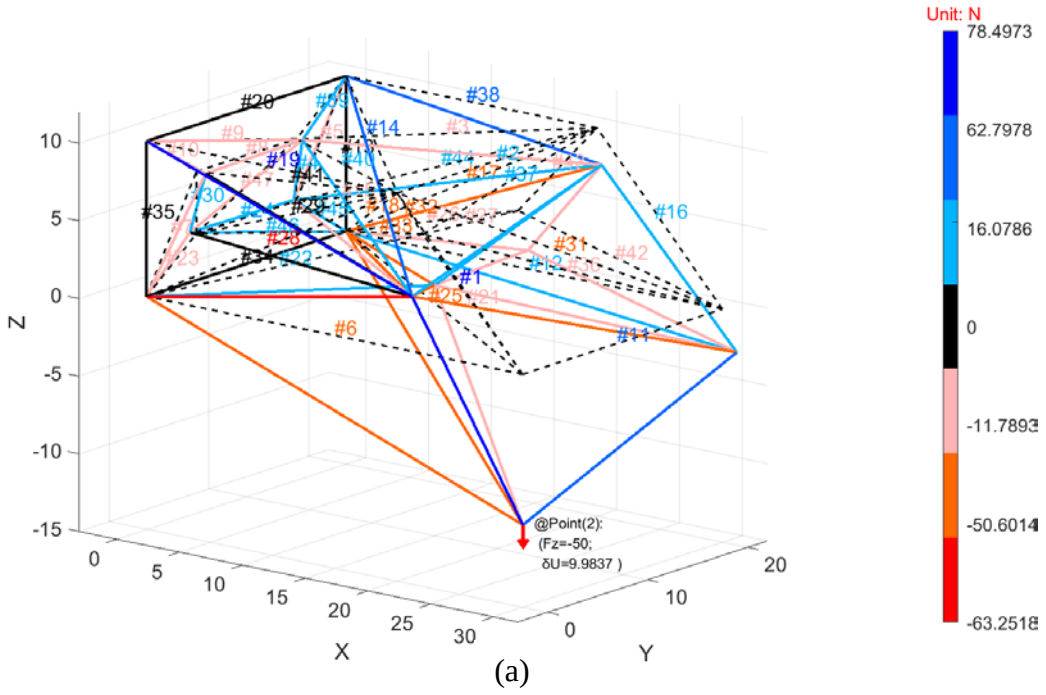

Figure 4.14. Displacements and force distribution in optimized trusses, example 3, case 3, load case 4

still on bar #19, with force slightly increased to 80 N. Overall, displacement was reduced by 4.42% and length was increased by 1.50%, Table 4.9.

Table 4.9. Pre-and post-optimization displacements and bar lengths, example 3, load case 4

	Initial, pre-optimization	Optimized-case4	Δ
Applied load	50 N	50 N	
Displacement (cm)	9.9837	9.5422	-4.42%
Total bar length (cm)	802.8	814.8	1.50%

Compared with previous cases, the hinge-like part with arbitrary patterns had fewer interlacing points as well as fewer boundary points to be freed in specific directions without influencing the initial overall dimensions of the volume envelope. The freest case 5 was based on the same case 4 of example 3. All conditions were kept the same, except for allowing all boundary points on the top left surface parallel to the *y*-*z* plane to move along the *y* and *z* directions, as shown in Figure 4.15.

Thus, in optimization case 5 for example 3, after applying SA optimization for stiffness, all yarn tensions were pushed to the maximum and minimum boundaries, with the tension combination as for case 4. Even though the structure and contact point locations moved with tension changes, displacement still showed little change, slightly reduced to 9.5104 cm, and the largest tension was still on bar #19, with force slightly increased to 80 N. Overall, displacement was reduced by 4.74% and length increased by 3.23%, Table 4.10.

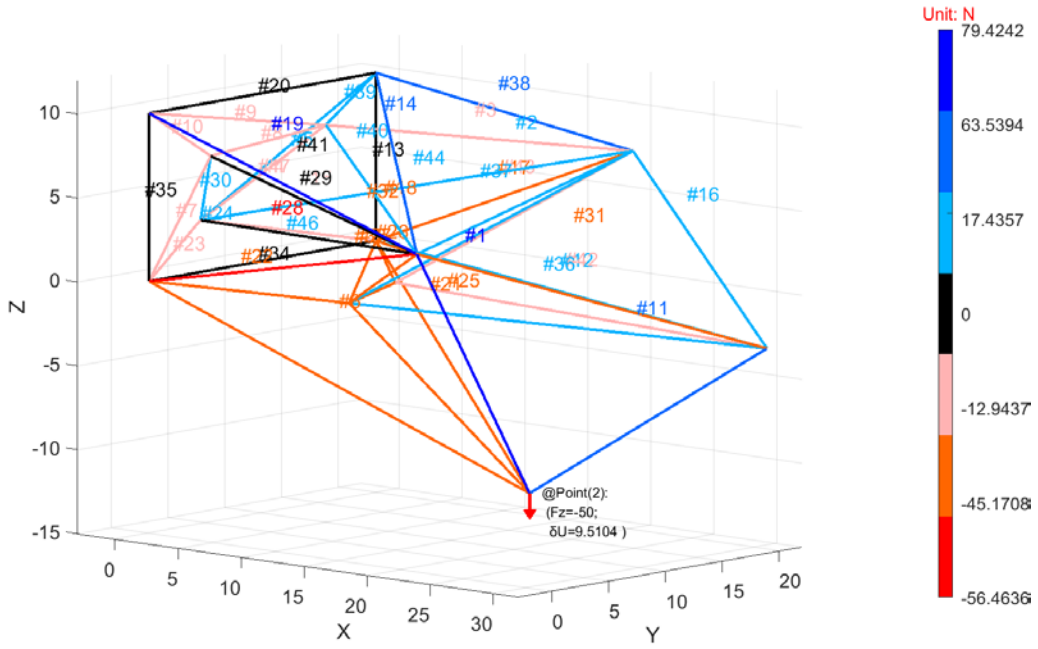

Figure 4.15. Displacements and force distribution in optimized trusses, example 3, case 3, load case 5

Table 4.10. Pre-and post-optimization displacements and bar lengths, example 3, load case 5

	Initial, pre-optimization	Optimized case 5	Δ
Applied load	50 N	50 N	
Displacement (cm)	9.9837	9.5104	-4.74%
Total bar length (cm)	802.8	828.7	3.23%

4.4. Chapter summary

After exploring 3 different open structures, from simply interlaced volumes to hinge-like parts featuring regular and arbitrary interlacing, the SA and FEA loops showed the ability to optimize structure stiffness under different loading cases, where

optimization reduced displacement from 2.47% (example 1, case 1) in the minimum to 26.54% (example 3, case 2) in the maximum. Moreover, by releasing some DOFs of boundary points, further optimization results with higher reductions in displacement were achieved, although some structures (case 3 and case 4, example 2) changed in dimensions whilst some (case 2 and case 3, example 3) did not.

Based on example 1, example 2 shows rather similar results because their interlacing patterns are very similar if observed separately in the single cube volume, whilst other settings remained the same. However, the example 2 can produce better optimized results as it enables some boundary points to be moveable, which are allowed to affect the structure in an optimization way.

At the same time, the difference between case 3 and case 4 in example 2 shows that more moveable DOFs do not guarantee better optimization results. This occurs because during SA calculation of interlacing patterns, more DOFs of boundary points could lead to many points to locating at the same position, causing structure collapse so that product dimensions cannot be maintained.

Apart from the directions, effects of increasing moveable points on optimization results can also be observed from the comparison of example 2 (9.49% in case 3 and 25.87% in case 4) and example 3 (26.54% in case 2 and 19.73% in case 3). With more points allowed to move, including interlacing points and contact points, example 3 can lead to better results without changing outline dimensions. For example 3, post-optimization results from the parts with regular interlacing (19.73% in case 3) and with arbitrary interlacing (4.42% in case 4 and 4.74% in case 5) also prove the point. However, a disadvantage of having more interlacing points is that more dry yarn is used. With the

same outline geometry in example 3, case 3 requires 1117.12 cm of yarn length in total, which is about 37.1% more than 814.83 cm in case 4 and about 34.8% more than 828.73 cm in case 5. The mass of the PMFRC parts will show similar increments.

Chapter 5. Manufacturing and Testing

5.1. Experimental validation of SA algorithm

After demonstrating usage of generalized strain energy (GSE) minimization for determining equilibrium positions of the interlacing points, the SA algorithm was deployed to search for these interlacing locations leading to minimal GSE. In this Chapter, coincidence between computational SA results and physical equilibrium locations was verified.

5.1.1. Introduction to generating weaving patterns

In order to validate the coincidence of computational SA results with manual measurement of positions in the physical space, a cubic volume with multiple openings organised in a grid was introduced, Figure 5.1. The holes allowed entry and exit of continuous interlaced yarns loaded with different combinations of tension.

The walls of the volume were made of general-purpose agglomerated wood fibre panels connected by utility plastic corner extrusions using nuts and bolts. The apparatus was sufficiently strong to withstand the small tensions imposed on dry wires and yarns, without significant displacements. Edge length was approximately 0.35 m, hence the inner volume measured approximately 0.043 m^3, providing enough space for coordinate measurements using means described below. The apparatus was also used for manufacturing initial prototype PMFRC parts.

Once the apparatus was available, yarns were positioned through the walls in order to be interlaced inside the working volume. As discovered, interlacing points should not be too close to each other for validation purposes, as increasing the distance

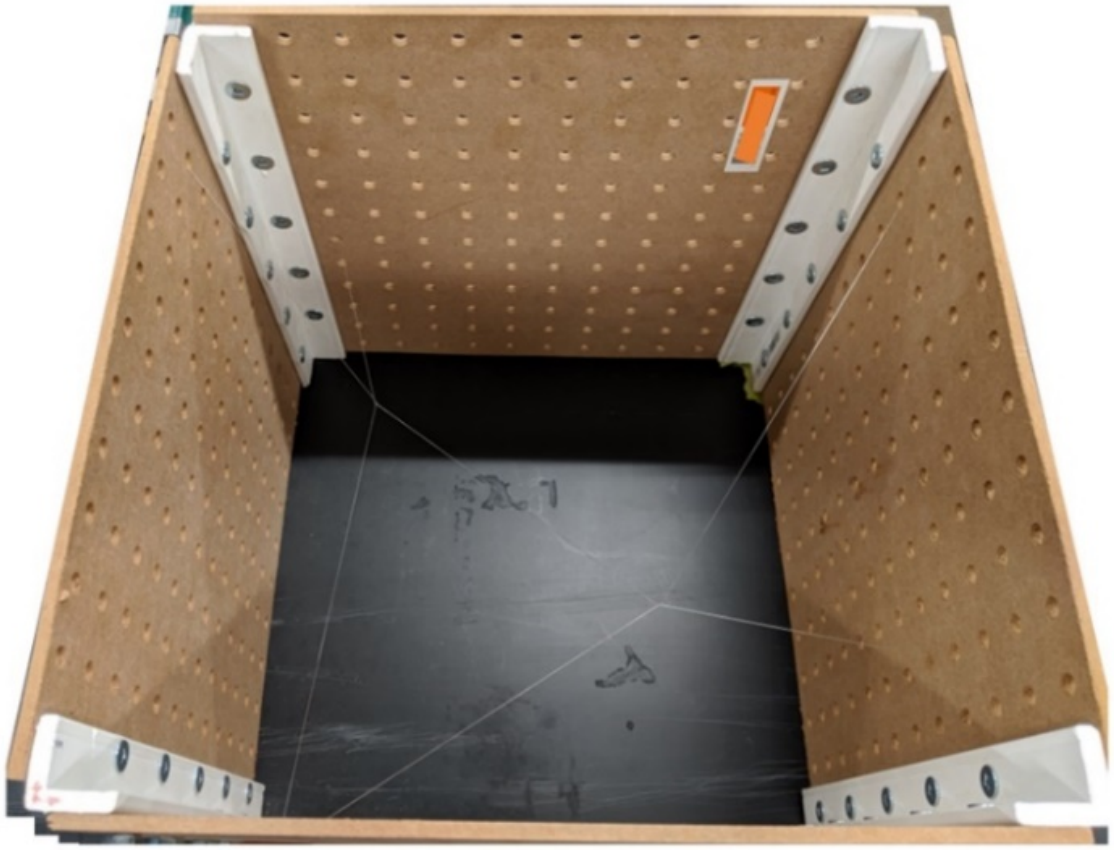

Figure 5.1. A designed cubic volume for generating early interlacing patterns

between them makes measurement easier and, most importantly, avoids subsequent deviations in positioning data.

A first interlacing pattern for validation was designed as shown in Figure 5.2. In the diagram, yarn 2 interlaces with yarn 1 at point a, and with yarn 3 at point b. Yarns 1-3 end in endpoints 1-6. Yarns were fixed at points 1, 3 and 5, and loaded under tension at points 2, 4 and 6 using known hanging masses. Reducing friction between interlaced yarns as well as between the yarns and apparatus would increase accuracy. Towards that

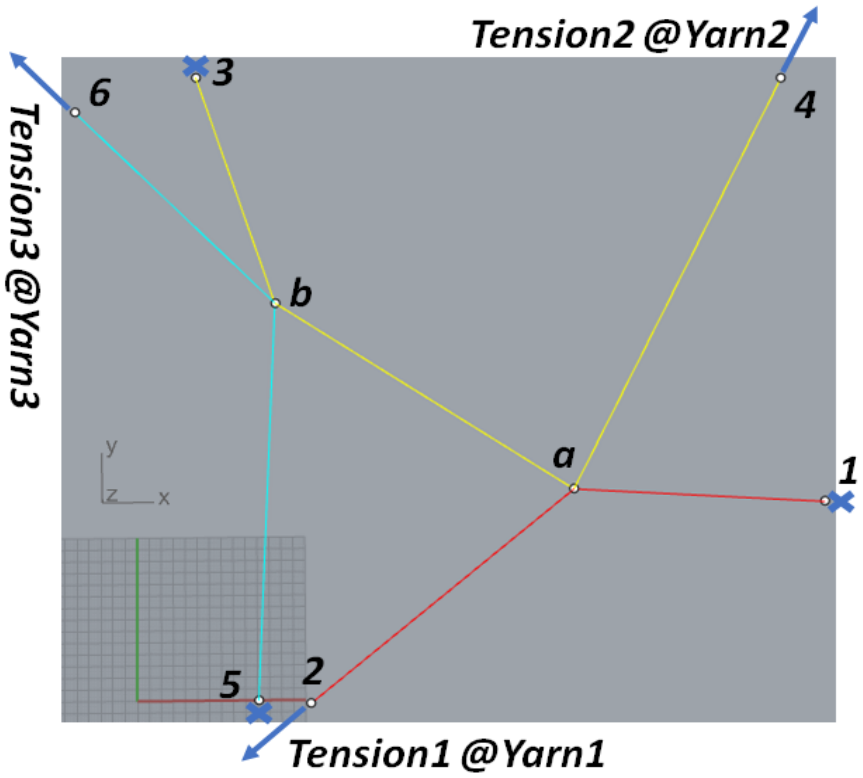

Figure 5.2. Schematic of interlacing yarns and points information

aim, a polyamide fishing line wire with smooth surfaces and small diameter was used in initial validation tests, instead of larger multifilament carbon yarns covered with sizing.

5.1.2. MicroScribe G2 and Rhino coordinate measurement software

After setting up different interlacing patterns, collecting the coordinate data of interlacing points was required. The contact coordinate measurement machine (CMM) MicroScribe G2, Figure 5.3, was employed for measuring these positions. Data was digitized through modeling software Rhino.

MicroScribe G2 is a contact 3D CMM device [121]. A mechanical arm with optical encoders at each of the five joints is used for moving a stylus within the 3D range. The stylus is held by hand to probe the object to be measured. Upon contact of the stylus tip with the object, a foot pedal is pressed by the operator. Once all points of interest for an interlacing pattern are selected, the data is transferred to the Rhino software application Rhino for decoding. Finally, the *x*, *y*, and *z* coordinates of the tip are calculated and drawn out. Microscribe quotes a precision of ±0.4 mm on coordinate positions for the G2 CMM device.

Figure 5.3. Diagram of MicroScribe G2 CMM device in home position

5.1.3. Validation results

During the validation process, two load cases were generated by hanging different masses to yarns 1-3 as listed in Table 5.1. The masses caused interlacing points to move to their equilibrium positions. Coordinates were measured thrice for each interlacing pattern; measurements for all SA experimental validations appear in Appendix A, Tables A.1, and A.2.

Table 5.1. Masses used for creating tension combinations for yarns 1-3

Load case	Tension 1	Tension 2	Tension 3
1	500 g	200 g	200 g
2	500 g	500 g	200 g

Average consistencies between measurements and calculation results using the SA algorithm are 95.4% (case 1) and 95.6% (case 2) at interlacing point a, and 98.3% (case 1) and 95.8% (case 2) at interlacing point b, Figure 5.4. Therefore, the SA algorithm for calculating the geometry information for interlacing points was verified.

5.2. Manufacture of prototypes

To create an open 3D structure, manufacturing consisted of inserting yarns inside the working volume through identified holes in the walls and according to a designed interlacing pattern, impregnating the yarns with resin by hand, and finally

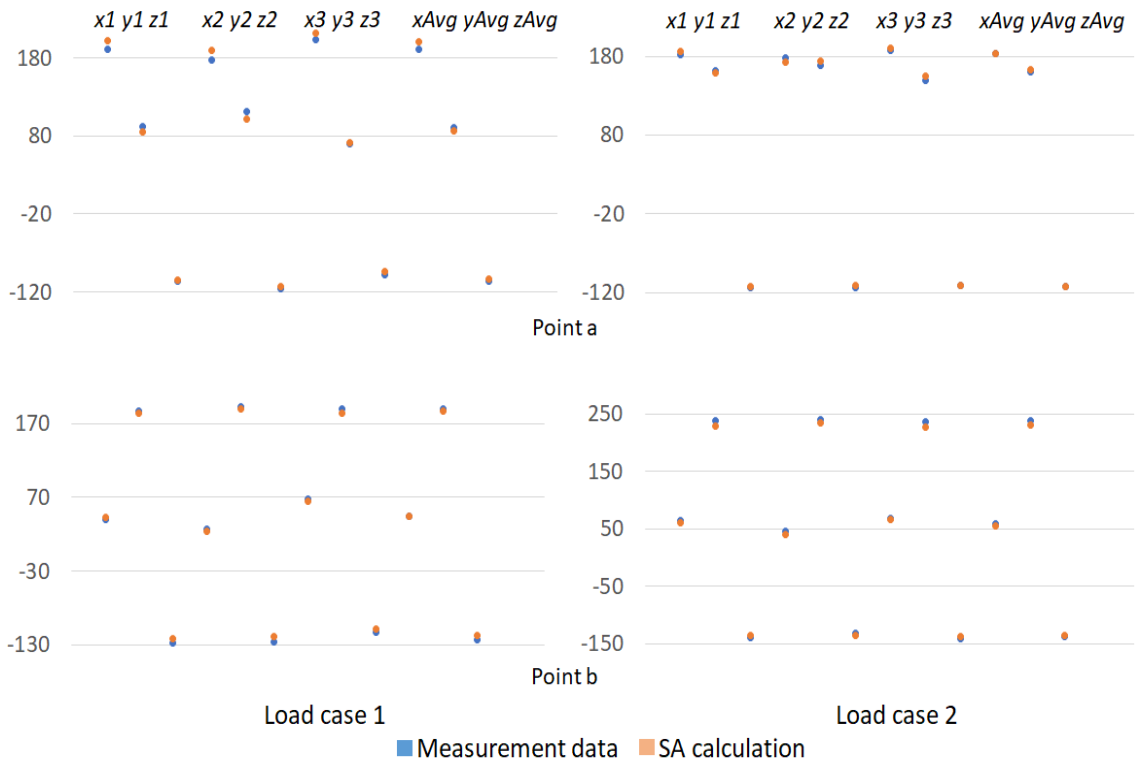

Figure 5.4. Data consistency at interlacing points a and b for load case 1 (left) and load case 2 (right)

taking the PMFRC structures out of the apparatus after cure. By installing open hooks in selected locations, the apparatus shown in Figure 5.1 was used for manufacturing a first prototype. After removing the structure along with the removable hooks, PMFRC parts were finished with necessary trimming.

The resin employed was the West System® epoxy 105/207, which possesses good fiberglass wet-out characteristics. The resin is typically used for laminating and also as a structural adhesive for boat building [122]. It cures rapidly with gel times around 60 minutes, 10 to 15 hours for cure to solid, and 4 to 7 days to reach maximum strength at minimum temperatures of 16 °C [123]. The cure process is notably exothermal; heat from impregnated yarns could be felt by hand during the manual impregnation process.

5.2.1. First-generation prototype 1

For exploring feasibility and requirements of open structure manufacturing and reducing waste of carbon fibers, yarns of natural wool were used as an alternative material to make prototype 1. After weaving, impregnating, and curing, prototype 1 was produced as example 1 in Chapter 4, Figure 5.5. Prototype 1 features 26 bars in total, 8 vertices and 1 interlacing point. Due to the geometry of the hooks, edges of the cube measured 15 cm. Prototype 1 featured the optimized geometry where the interlacing point was not in the centre of the cube.

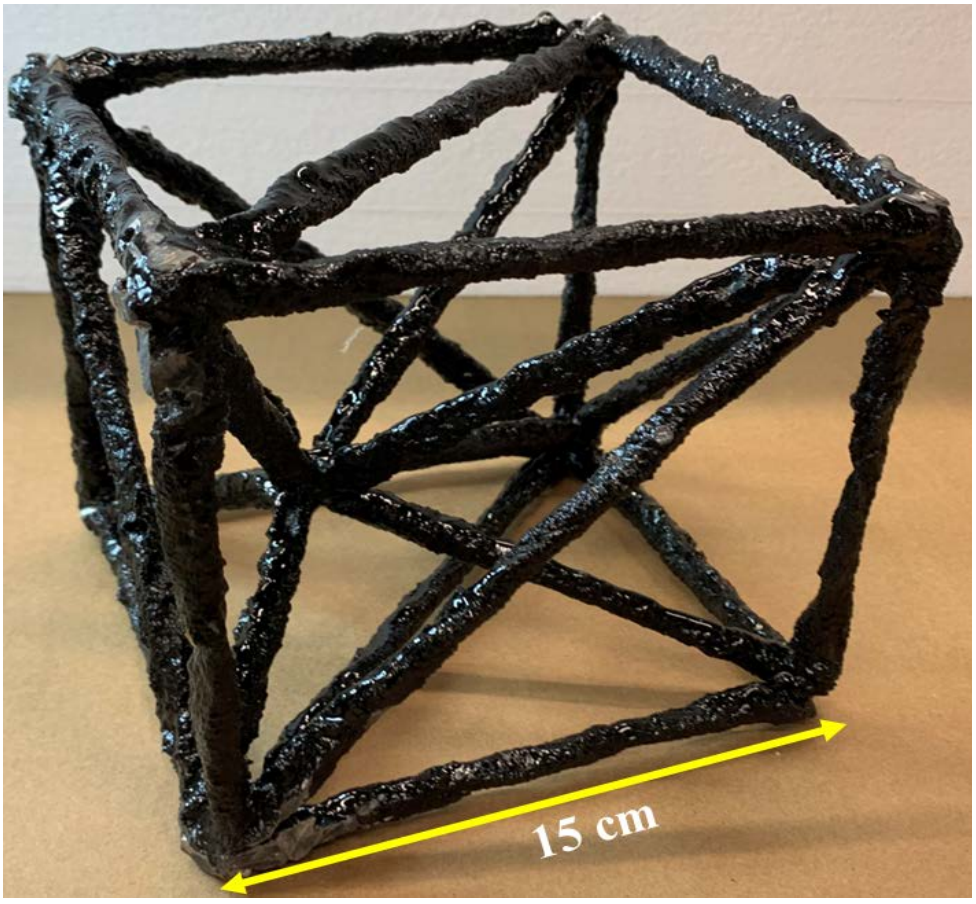

Figure 5.5. Prototype 1 with cubic structure, post-optimization

5.2.2. Second-generation prototypes

Successful fabrication of first-generation prototype 1 demonstrated the feasibility of manually wetting the resin into the material for the purpose of obtaining solid structures of geometries that are generally correct at a macroscopic level. It also provided an operation reference for second-generation prototypes. In manufacturing these prototypes, carbon fiber yarns were employed. The material used was TENAX®-J HTS40 E13 12K 800 tex yarns, with tensile strength and modulus suitable for structural composites [124]. Typical fibre properties appear in Table 5.2. The 0.462 mm² cross-section area of a single yarn is small for the production of bars for the prototypes, compared with a typical bar length of 15 cm. Combining 22 yarns through light twisting at approximately 10 turns/m increased total yarn cross-section and led to solid composite bars with a cross-section area approximately around 10 to 15 mm², although these dimensions were by no means precise.

Table 5.2. Typical properties of carbon yarn TENAX®-J: HTS40 E13 12K 800 tex

Strength:	4275 MPa
Modulus:	236 GPa
Density:	1.76 g/cc
Filament Diameter:	7 μm
Yarn Cross-Section:	0.462 mm²

With validated tensions and methods that were operational for the early purpose at hand, which was only to produce solid structures with generally accurate positioning

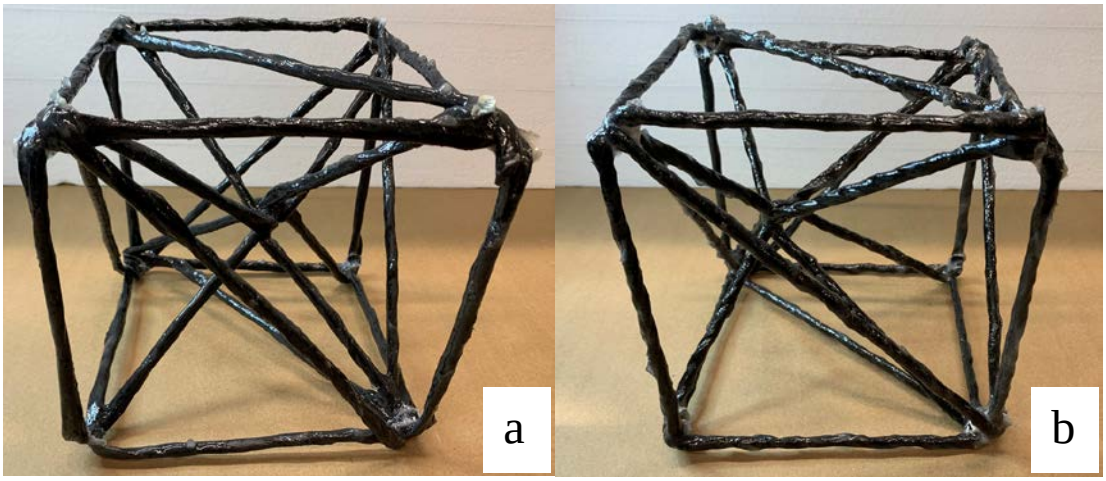

Figure 5.6. Second generation prototypes of cubic structures in pre-optimized (a) and post-optimized (b) configurations

of the interlacing points, two more composite parts made from twisted carbon yarns were produced, Figure 5.6. Overall dimensions were similar to those of prototype 1.

Prototype 2.1 shown on the left, Figure 5.6 a), was produced in the pre-optimization configuration of example 1, and prototype 2.2 shown on the right, Figure 5.6 b), was produced in the post-optimization configuration. As such, prototype 2.2 was an upgrade from prototype 1 in terms of the materials used. Prototypes 2.1 and 2.2 featured similar edge lengths, which were also similar to those of prototype 1, but differed in terms of their geometry. With hand-on experience of prototype 1, manufacturing process of prototypes 2.1 and 2.2 were smoothly controlled.

To address that geometrical disadvantage and produce a PMFRC structure that is less open hence more structural, the second-generation prototype 2.3 was manufactured as shown in Figure 5.7.

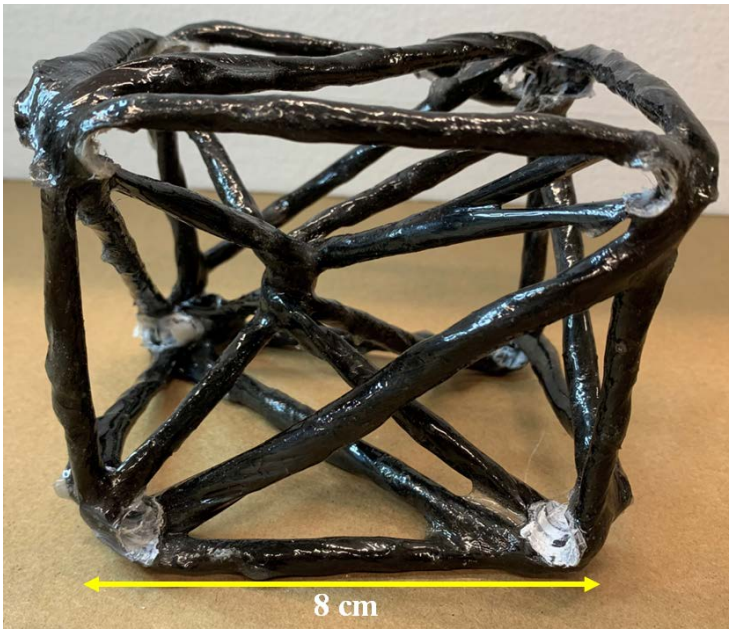

Figure 5.7. Prototype 2.3 with smaller cubic structure, post-optimization

Prototype 2.3 featured the same interlacing pattern as prototype 2.2 but with smaller side length of 8 cm. Despite imperfect geometries in overlapping areas, the optimized paths were fully featured. The side lengths of the PMFRC structural were set high, which resulted in largely open structures. Due to the small lengths, the dry textile structure was difficult to create and interlace, and the resulting PMFRC part was accurate due to the use of hooks and coarse twisted yarns. The main issues arose at the corners, caused by overlapping yarns and tooling. Advanced tooling and geometry leading to better interlacing will be recommended for future work, to address corner and other accuracy problems.

5.2.3. Third-generation prototypes

With the objective of exploring geometries beyond the simple unit cube with simplest interlacing pattern with 1 interlacing point, a hinge-like open truss was designed and manufactured using the same manufacturing process. The hinge-like truss features 105 bars, almost 4 times more than the cubic prototypes at 26, and its outline dimensions are around 30 cm in length, 20 cm in width and 10 cm in height, which entails much larger tooling volume requirements. To achieve this, another tooling frame made of stainless steel was introduced as shown in Figure 5.8 a). The resulting open structure PMFRC prototype 3 was manufactured in post-optimization configuration as shown in Figure 5.8 b).

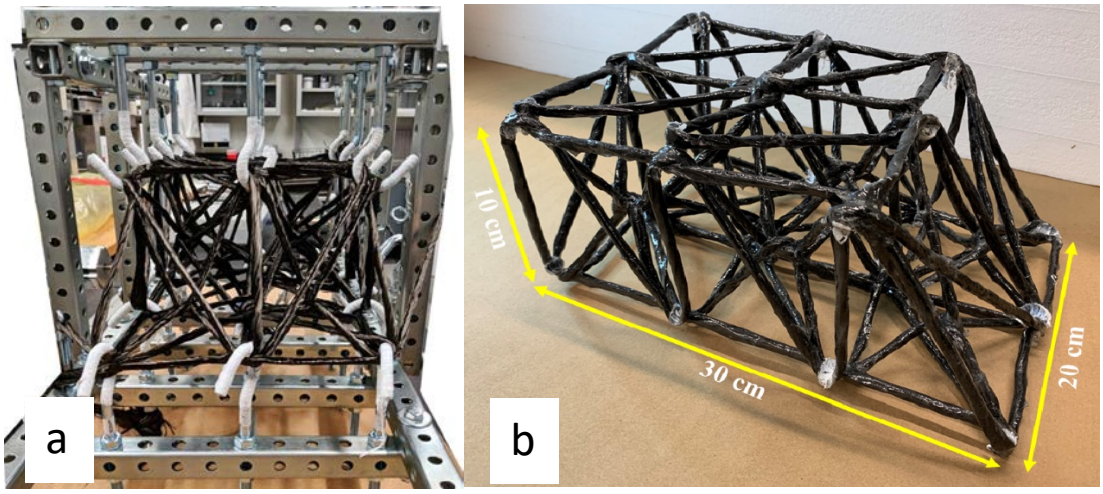

Figure 5.8. Tooling frame made of steel tubes (a) and prototype 3 of the hinge-like composite part in post-optimization configuration (b)

The steel tubes of the tooling frame provided a base for installing open hooks. Multiple tubes enabled the positioning of hook locations as required by design. Hinge-like prototype 3 featured 21 fixed vertices and 6 interlacing points inside the structure. Compared with procedures for producing the cubic prototypes 1 and 2 series, the relatively complex interlacing pattern, lengthy manual interlacing, and difficult manual impregnation process made hinge-like prototype much more complicated to manufacture, requiring about fourfold time despite cure time being the same.

At the same time, some endpoints in the final PMFRC open structure part were superimposed and/or twisted, causing significant dimension offsets due to yarn bundle overlaps at these points. Practice showed that manufacturing by manually interlacing and impregnating collimated and twisted yarns presented as rod-like bars resulted in bottlenecks caused by the complex structure, which was not conducive to a good standard of manufacturing structural PMFRC parts. However, SA optimization was demonstrated in the fabrication, and hand-on experience, such as dry yarn interlacing and resin impregnation, was gained towards making open structure composite products.

5.3. Testing results

Topology optimization through steepest ascent methods aimed at improving the mechanical performance of PMFRC open structure parts, namely their stiffness in the elastic domain. Therefore, testing on prototype parts was attempted, even as dimensions of the prototypes were marred by low accuracy, and stiffness improvements were limited for the simpler structures.

Non-destructive compression testing was performed, aiming at determining stiffness in pre-optimization and post-optimization configurations based on prototypes 2.1 and 2.2, as shown in Figure 5.9. A 100 N load cell was mounted in an Instron 4482 100 kN screw-driven universal testing frame, with a metallic pressing head installed on the load cell. Prototypes 2.1 and 2.2 were successively positioned on a flat aluminum base plate. Load was applied as a constant displacement speed of 1 mm/min, with a maximum load set to 20 N in light of the manual manufacturing process. The goal was to load sufficiently in order to observe a linear segment of the load-displacement curves, without damaging the imperfect PMFRC parts.

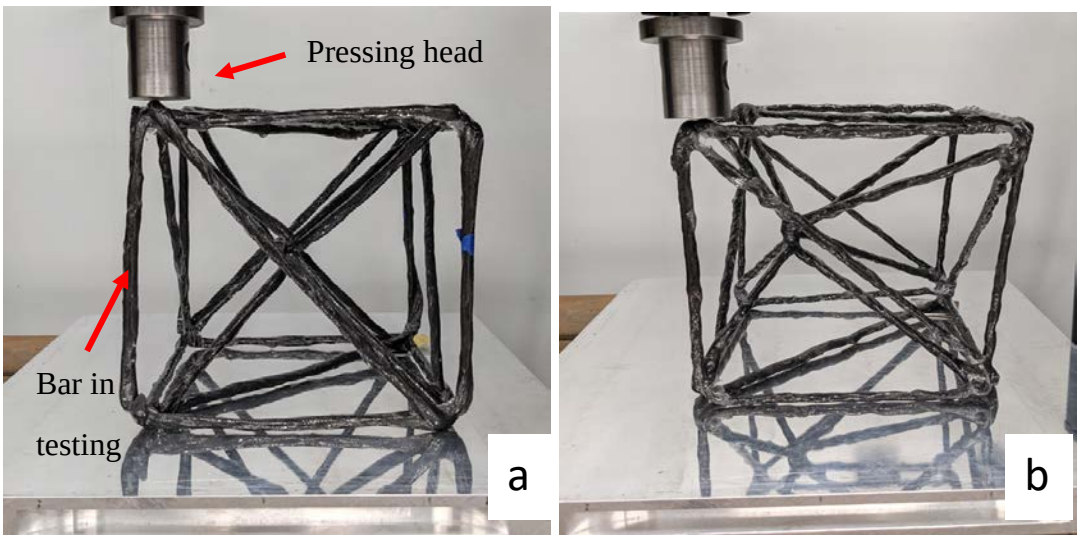

Figure 5.9. Compression testing setups for prototype 2.1 in pre-optimization configuration (a) and prototype 2.2 in post-optimization configuration (b)

According to calculations presented in Chapter 4, individual periphery bars making the outer geometry of the cubes were tested under compressive vertical loads as illustrated in Figure 5.9 (a), with the aim of identifying the largest, non-outlier but

hopefully relatively reproducible stiffness values. Non-optimized prototype 2.1 was tested along each of the 12 bars making the external cube, whilst optimized prototype 2.2 was tested along bars 1-4 extending in the plane closer to the optimized interlacing point, and bars 5-8 extending in the plane furthest from the optimized interlacing point.

In order to obtain the best possible data for the context, and to reduce experimental offset in testing, each bar mentioned above was tested 3 times. Residual initial displacements where force was essentially zero were removed from the raw data, and experimental compressive load-displacement curves were generated. However, due to the imperfect geometries of prototypes 2.1 and 2.2, relative displacements could possibly occur on the surface between the aluminum plate and the PMFRC structures, when the prototypes were under compressive loads. When this situation happened, experimental data would reflect as a sudden change in slope of the load-displacement curves, which would not be eligible for testing results as testing conditions had changed. Eventually, the slope of each individual curve was calculated, and identified with the ranges over which the calculation was done.

For example, Figure 5.10 illustrates 2 examples of load-displacement curves processed for testing bar-1 (a) and bar-2 (b) in optimized prototype 2.2. The test-1 curve for bar-1 in Figure 5.10 (a) showed a sudden change in the slope, which means this load-displacement curve was not produced in good testing conditions hence it was discarded. The final stiffness result of bar-1 was determined by the average slope of test-2 and test-3 curves within the ranges 10 N to 20 N. By contrast, the 3 tests of bar-2 in Figure 5.10 (b) were all in good testing conditions and used for calculating the average in that case, over the same range. Therefore, all 3 testing results for bar-2 were presented in Figure 5.11 while the test-1 value for bar-1 was not included. Other raw curves processed for

individual bars in both prototypes 2.1 and 2.2 are supplied in Appendix B, and their corresponding stiffness values appear in Table 5.3.

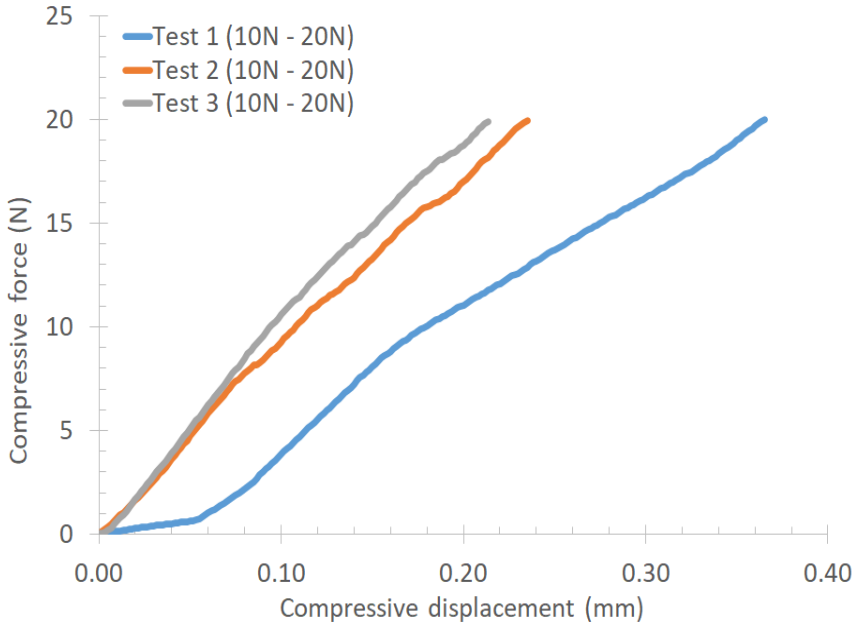

(a)

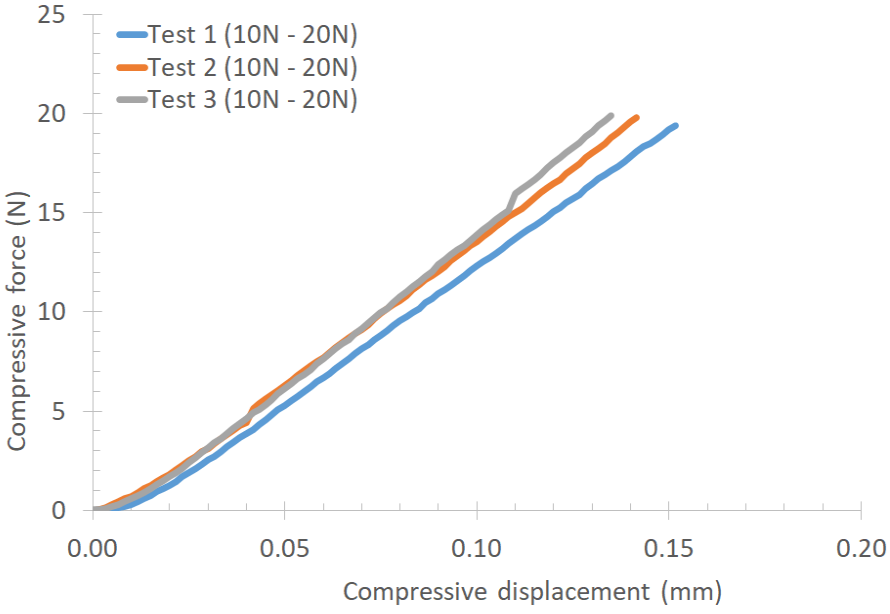

(b)

Figure 5.10. Load-displacement curves processed for tests along individuals bar-1 (a) and bar-2 (b) in post-optimized prototype 2.2

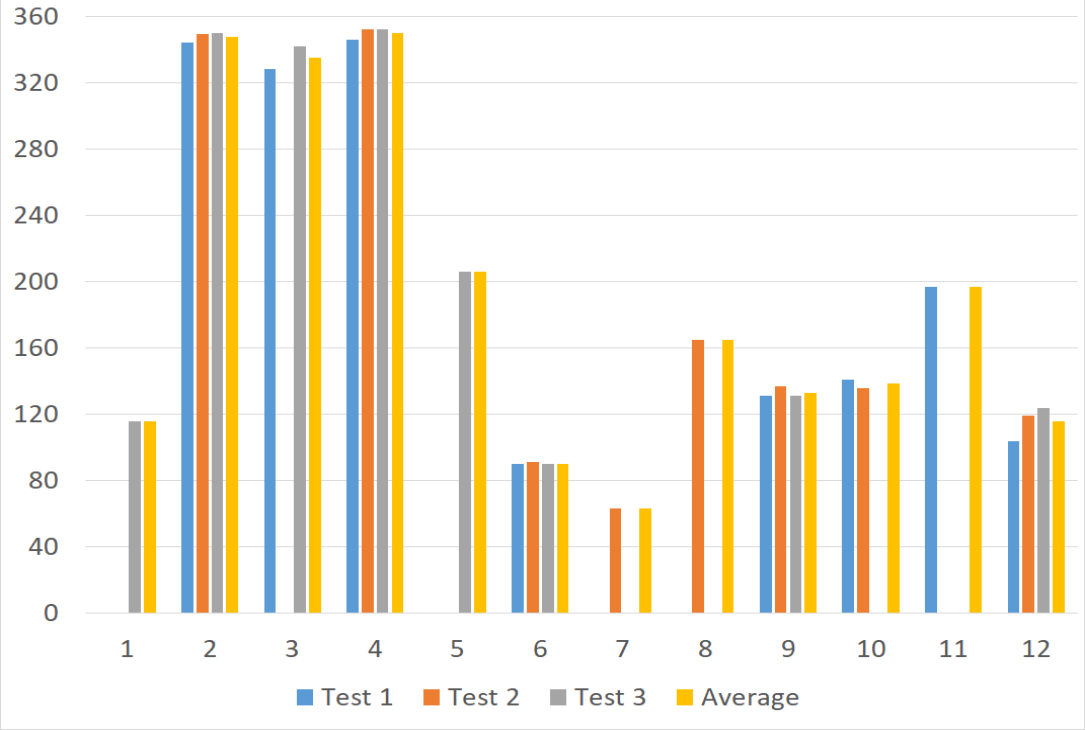

(a)

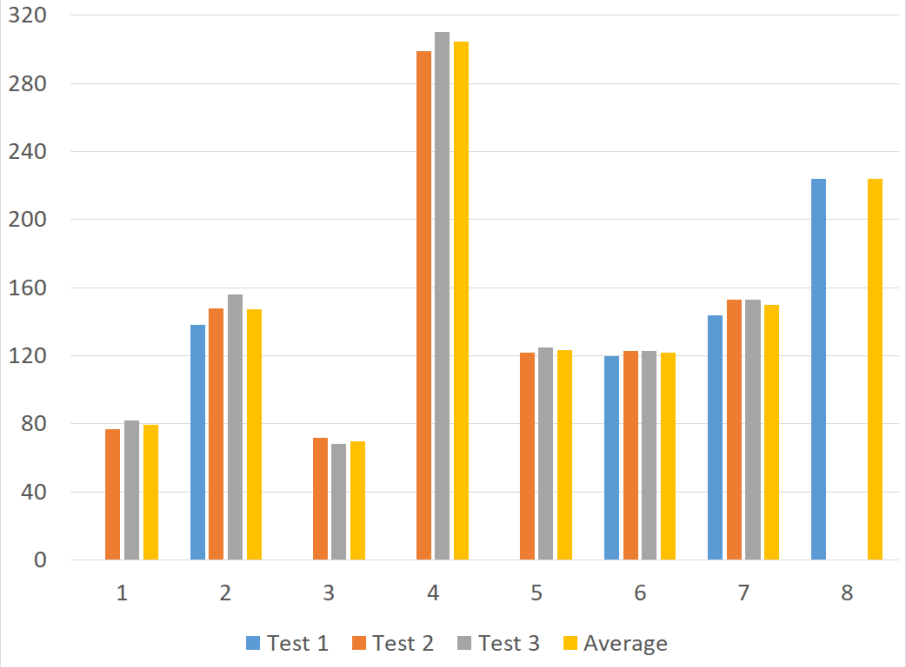

(b)

Figure 5.11. Stiffness results for individual bars in prototypes 2.1 (a) and 2.2 (b), (unit: MPa)

Table 5.3. Stiffness values for individual bars in prototypes 2.1 and 2.2

Sample	Bar	Stiffness (N/m)			
		Test 1	**Test 2**	**Test 3**	**Average**
Prototype 2.1	1	/	/	116344	116344
	2	344136	348731	350197	347688
	3	328295	/	342491	335393
	4	346006	351858	352378	350081
	5	/	/	206373	206373
	6	90440	91168	89879	90496
	7	/	62937	/	62937
	8	/	165483	/	165483
	9	131285	137103	131162	133183
	10	140663	135547	/	138105
	11	196595	/	/	196595
	12	104267	118698	124223	115729
Prototype 2.2	1	/	77331	82211	79771
	2	138002	148058	155917	147326
	3	/	72472	67700	70086
	4	/	299437	310447	304942
	5	/	122476	125332	123904
	6	119811	122547	123057	121805
	7	144448	152999	153088	150178
	8	223570	/	/	223570

From Table 5.3, stiffness values on both prototypes are highly scattered, which indicates that the tests are effectively invalid. The main reasons include irregular geometries in both samples, varied bar cross sections, and unstable contact between the pressing surface, PMFRC parts and tooling plate. Eventually, for the non-optimized structure of prototype 2.1, the 3 highest values (bars 2-4) were retained, and averaged at 334 387 N/m.

For the optimized structure of prototype 2.2, in bars 1-4 closer to the optimized side, the highest value of 304 942 N/m was found in the bar 4. Therefore, no higher stiffness value was seen in the post-optimized structure; the load-displacement curves for the original PMFRC structure showed a better average stiffness than the post-optimized one, which is inconclusive. However, for prototype 2.2, in the bars 5-8 further away from the optimized side, the highest value of 223 570 N/m was found in the bar 8, which is much lower than the highest value 304 942 N/m of the other side.

5.4. Chapter summary

In this Chapter, manufactured structures corresponding to simulated ones in Chapter 4 were presented. The validity of the SA algorithm was demonstrated, and two tooling frameworks were created. During the process, carbon yarns TENAX®-J: HTS40 E13 12K 800 tex were chosen for interlacing the open 3D dry reinforcement structures, and West System epoxy 207/105 was employed for consolidation. A first prototype was made of wool instead of carbon fibre to assess the manual process and accumulate experience. The second-generation prototypes were all produced on from the verified process settings. Upon manufacturing the hinge-like structure, the manual interlacing and

percolation methods introduced difficulties and limitations due to the complex structure built manually in the framework. More developments of the manufacturing process will be recommended as future work.

Chapter 6. Conclusion and Future Work

6.1. Conclusions

This thesis shows the introduction of an optimization method, using SA algorithm and FEA computations, for manufacturing 3D parts with optimized open structures. Optimization loops use SA algorithms to identify the structure geometry, and FEA to judge the best result under specific loading cases. Aiming at verifying the improvements resulting from simulations, the structures were produced manually with specifically created frameworks. After the testing the simpler cubic parts, results were compared with each other and theoretical data and proved, to some extent, the validity of equilibrium and stiffness optimization.

In conclusion, firstly, as tensions change both the stiffness and mass, the optimization algorithm must judge by them both instead of stiffness only. Generalized strain energy (GSE) is studied for optimizing stiffness because it enables the equilibrium to be determined, but the mass map as a function of interlacing positions only is different.

Secondly, the initial interlacing patterns is currently determined by hand, and the manufacturing process will affect the resulting stiffness or strength with load transferring at interlacing points. Because of the use of twisted collimated yarns, overlapping was observed at some vertices.

6.2. Future work and recommendations

Following from the points to be improved above, recommended future work for this technology is as follows:

For structural optimization, only tensile and compression properties were considered in the models. The next step consists in introducing bending and torsion in bars of more sophisticated geometry, for optimizing the PMFRC parts.

Part designs and interlacing paths should also be improved. For example, the twisted yarns and circular cross sections of bar elements should be replaced by more mature designs, and the small radius overlapped yarn bundles should be avoided. Besides, after interlacing and during optimization of geometry through tensions, yarns that were not previously in contact may touch one another and create new contact or interlacing points as opposed to simply get past one another, which is not physically possible. Therefore, yarn collision or interference during tension optimization ought to be detected.

As for limitations of the manufacturing process used for the first-generation and second-generation prototypes towards experimental validation, working on interlacing as well as impregnating has hit a ceiling with regards to the current tooling, which is difficult and time-consuming to use. Systematic methods and new tooling must be designed for rectifying that. Many manufacturing methods will have to be tested, including using thicker yarns with more fibers for interlacing; trying thermoplastic prepreg or commingled yarns, perhaps coupled with thermoplastic powder for compressing and consolidating; heating thermoset prepregs after interlacing; and so on.

References

[1] Amirhossein Lotfi et al., 'Natural Fiber–Reinforced Composites: A Review on Material, Manufacturing, and Machinability', Journal of Thermoplastic Composite Materials 34, no. 2 (February 2021): 238–84, https://doi.org/10.1177/0892705719844546.

[2] Amin Salehi-Khojin et al., "The Role of Temperature on Impact Properties of Kevlar/Fiberglass Composite Laminates," Composites Part B: Engineering 37, no. 7–8 (October 2006): 593–602, https://doi.org/10.1016/j.compositesb.2006.03.009.

[3] R.I. Haresceugh et al., "Aircraft and Aerospace Applications of Composites," in Concise Encyclopedia of Composite Materials (Elsevier, 1994), 1–31, https://doi.org/10.1016/B978-0-08-042300-5.50012-1.

[4] R.R. Boyer et al., "Materials Considerations for Aerospace Applications," MRS Bulletin 40, no. 12 (December 2015): 1055–66, https://doi.org/10.1557/mrs.2015.278.

[5] Zilina, Slovak Republic, Mrazova Maria, "Advanced Composite Materials of the Future in Aerospace Industry," *INCAS BULLETIN* 5, no. 3 (September 6, 2013): 139–50, https://doi.org/10.13111/2066-8201.2013.5.3.14.

[6] C.H. Zweben, "Composites: Overview," in *Encyclopedia of Condensed Matter Physics* (Elsevier, 2005), 192–208, https://doi.org/10.1016/B0-12-369401-9/00545-3.

[7] D. Dixit et al., 'Lightweight Composite Materials Processing', in Lightweight Ballistic Composites (Elsevier, 2016), 157–216, https://doi.org/10.1016/B978-0-08-100406-7.00006-4.

[8] Hom Nath Dhakal and Sikiru Oluwarotimi Ismail, ‘Design, Manufacturing Processes and Their Effects on Bio-Composite Properties’, in Sustainable Composites for Lightweight Applications (Elsevier, 2021), 121–77, https://doi.org/10.1016/B978-0-12-818316-8.00005-0.

[9] P.J. Halley, ‘Rheology of Thermosets: The Use of Chemorheology to Characterise and Model Thermoset Flow Behaviour’, in Thermosets (Elsevier, 2012), 92–117, https://doi.org/10.1533/9780857097637.1.92.

[10] D. Dixit et al., ‘Lightweight Composite Materials Processing’, in Lightweight Ballistic Composites (Elsevier, 2016), 157–216, https://doi.org/10.1016/B978-0-08-100406-7.00006-4.

[11] Francesco Flora et al., ‘Ultrasonic Consolidation (UC) Debulking of Thermosetting Prepreg for Autoclave Curing of Composite Laminates’, Materials Today: Proceedings 34 (2021): 106–12, https://doi.org/10.1016/j.matpr.2020.01.376.

[12] Kozaczuk, K., 2016. Automated fibre placement systems overview. Trans. Instit. Aviat. 245 (4),52e59.

[13] Asit Kumar Gain, Ebrahim Oromiehie, and B. Gangadhara Prusty, ‘Nanomechanical Characterisation of CF-PEEK Composites Manufactured Using Automated Fibre Placement (AFP)’, Composites Communications 31 (April 2022): 101109, https://doi.org/10.1016/j.coco.2022.101109.

[14] E. Oromiehie, et al., Structural health monitoring and processing of composites using photonic sensing technology, in: 20th International Conference on Composite Materials (ICCM 20). 19-24 July; Copenhagen, Denmark, 2015.

[15] J. Wang, P. Simacek, and S.G. Advani, ‘Use of Medial Axis to Find Optimal Channel Designs to Reduce Mold Filling Time in Resin Transfer Molding’, Composites Part A: Applied Science and Manufacturing 95 (April 2017): 161–72, https://doi.org/10.1016/j.compositesa.2017.01.003.

[16] Colin Gomez et al., ‘Resin Transfer Molding of High-Fluidity Polyamide-6 with Modified Glass-Fabric Preforms’, Composites Part A: Applied Science and Manufacturing 147 (August 2021): 106448, https://doi.org/10.1016/j.compositesa.2021.106448.

[17] Ahmed Ouezgan et al., ‘Articulated Compression Resin Transfer Molding with a Flexible Membrane’, Materials Today: Proceedings 51 (2022): 1404–9, https://doi.org/10.1016/j.matpr.2021.11.531.

[18] Hang Zusheng et al., ‘Resin Transfer Molding Process and Performance of Paraffin Based Energy Storage Composites Framed on Polyurethane Foam’, Materials Science for Energy Technologies 5 (2022): 252–61, https://doi.org/10.1016/j.mset.2022.03.002.

[19] Ajay Kumar and Deepak Kumar, ‘Vacuum Assisted Resin Transfer Moulding Process Review and Variability Analysis Using Taguchi Optimization Technique’, Materials Today: Proceedings 50 (2022): 1472–79, https://doi.org/10.1016/j.matpr.2021.09.055.

[20] Dominik Bender, Jens Schuster, and Dirk Heider, ‘Flow Rate Control during Vacuum-Assisted Resin Transfer Molding (VARTM) Processing’, Composites Science and Technology 66, no. 13 (October 2006): 2265–71, https://doi.org/10.1016/j.compscitech.2005.12.008.

[21] Fengky Satria Yoresta et al., 'Enhancing Buckling Capacity of Angle Steel Using Unbonded CFRP Laminates Processed by Vacuum-Assisted Resin Transfer Molding (VaRTM)', Structures 41 (July 2022): 173–89, https://doi.org/10.1016/j.istruc.2022.05.011.

[22] Jae-In Kim et al., 'Prediction of the Vacuum Assisted Resin Transfer Molding (VARTM) Process Considering the Directional Permeability of Sheared Woven Fabric', Composite Structures 211 (March 2019): 236–43, https://doi.org/10.1016/j.compstruct.2018.12.043.

[23] Byron Blakey-Milner et al., "Metal Additive Manufacturing in Aerospace: A Review," *Materials & Design* 209 (November 2021): 110008, https://doi.org/10.1016/j.matdes.2021.110008.

[24] John O. Milewski, Additive Manufacturing of Metals, vol. 258, Springer Series in Materials Science (Cham: Springer International Publishing, 2017), https://doi.org/10.1007/978-3-319-58205-4.

[25] Zheng Qiu et al., 'Concurrent Topology and Fiber Orientation Optimization Method for Fiber-Reinforced Composites Based on Composite Additive Manufacturing', *Computer Methods in Applied Mechanics and Engineering* 395 (May 2022): 114962, https://doi.org/10.1016/j.cma.2022.114962.

[26] Thomas Gereke and Chokri Cherif, "A Review of Numerical Models for 3D Woven Composite Reinforcements," Composite Structures 209 (February 2019): 60–66, https://doi.org/10.1016/j.compstruct.2018.10.085.

[27] A.L.R. Prathyusha and G. Raghu Babu, "A Review on Additive Manufacturing and Topology Optimization Process for Weight Reduction Studies in Various Industrial

Applications," *Materials Today: Proceedings*, March 2022, S2214785322010525, https://doi.org/10.1016/j.matpr.2022.02.604.

[28] Sattar Mohammadi Esfarjani, Ali Dadashi, and Mohammad Azadi, "Topology Optimization of Additive-Manufactured Metamaterial Structures: A Review Focused on Multi-Material Types," Forces in Mechanics 7 (May 2022): 100100, https://doi.org/10.1016/j.finmec.2022.100100.

[29] Dirk Herzog et al., "Additive Manufacturing of Metals," *Acta Materialia* 117 (September 2016): 371–92, https://doi.org/10.1016/j.actamat.2016.07.019.

[30] Dirk Herzog et al., "Additive Manufacturing of Metals," Acta Materialia 117 (September 2016): 371–92, https://doi.org/10.1016/j.actamat.2016.07.019.

[31] János Plocher and Ajit Panesar, "Review on Design and Structural Optimisation in Additive Manufacturing: Towards next-Generation Lightweight Structures," Materials & Design 183 (December 2019): 108164, https://doi.org/10.1016/j.matdes.2019.108164.

[32] Jihong Zhu et al., "A Review of Topology Optimization for Additive Manufacturing: Status and Challenges," Chinese Journal of Aeronautics 34, no. 1 (January 2021): 91–110, https://doi.org/10.1016/j.cja.2020.09.020.

[33] L. Sorrentino et al., "Manufacture of High Performance Isogrid Structure by Robotic Filament Winding," Composite Structures 164 (March 2017): 43–50, https://doi.org/10.1016/j.compstruct.2016.12.061.

[34] Ke Dong et al., "3D Printing of Continuous Fiber Reinforced Diamond Cellular Structural Composites and Tensile Properties," Composite Structures 250 (October 2020): 112610, https://doi.org/10.1016/j.compstruct.2020.112610.

[35] “3D Printing Composites with Markforged”, [online], https://markforged.com/resources/learn/design-for-additive-manufacturing-plastics-composites/3d-printing-composites-introduction/3d-printing-composites-with-markforged

[36] Thomas Jared Weaver and David W. Jensen, “Mechanical Characterization of a Graphite/Epoxy IsoTruss,” Journal of Aerospace Engineering 13, no. 1 (January 2000): 23–35, https://doi.org/10.1061/(ASCE)0893-1321(2000)13:1(23).

[37] Changliang Lai et al., “A Flexible Tooling and Local Consolidation Process to Manufacture 1D Lattice Truss Composite Structure,” Composites Science and Technology 113 (June 2015): 63–70, https://doi.org/10.1016/j.compscitech.2015.03.018.

[38] Recep M. Gorguluarslan et al., “An Improved Lattice Structure Design Optimization Framework Considering Additive Manufacturing Constraints,” Rapid Prototyping Journal 23, no. 2 (March 20, 2017): 305–19, https://doi.org/10.1108/RPJ-10-2015-0139.

[39] A V Azarov, V A Kolesnikov, and A R Khaziev, “Development of Equipment for Composite 3D Printing of Structural Elements for Aerospace Applications,” IOP Conference Series: Materials Science and Engineering 934, no. 1 (September 1, 2020): 012049, https://doi.org/10.1088/1757-899X/934/1/012049.

[40] Christopher J. Hunt et al., “A Review of Composite Lattice Structures,” *Composite Structures* 284 (March 2022): 115120, https://doi.org/10.1016/j.compstruct.2021.115120.

[41] A. Fadavian et al., “A Comparative Review Study on the Manufacturing Processes of Composite Grid Structures,” Metallurgical and Materials Engineering 21, no. 2 (June 30, 2015): 79–88, https://doi.org/10.30544/98.

[42] Yuguo Sun and Liang Gao, ‘Structural Responses of All-Composite Improved-Pyramidal Truss Sandwich Cores’, Materials & Design 43 (January 2013): 50–58, https://doi.org/10.1016/j.matdes.2012.06.033.

[43] R Umer et al., ‘Analysis of the Compression Behaviour of Different Composite Lattice Designs’, Journal of Composite Materials 52, no. 6 (March 2018): 715–29, https://doi.org/10.1177/0021998317714531.

[44] Qianqian Sui, Changliang Lai, and Hualin Fan, “Fundamental Frequency of IsoTruss Tubular Composite Structures,” Archive of Applied Mechanics 87, no. 12 (December 2017): 2011–24, https://doi.org/10.1007/s00419-017-1308-z.

[45] Du Plessis, Anton & Yadroitsava, Ina & Yadroitsev, Igor. (2018). Ti6Al4V lightweight lattice structures manufactured by laser powder bed fusion for load-bearing applications. Optics & Laser Technology. 108. 521-528. 10.1016/j.optlastec.2018.07.050.

[46] Elliott W. Jost, David G. Moore, and Christopher Saldana, “Evolution of Global and Local Deformation in Additively Manufactured Octet Truss Lattice Structures,” Additive Manufacturing Letters 1 (December 2021): 100010, https://doi.org/10.1016/j.addlet.2021.100010.

[47] O Fashanu et al., “Mechanical Performance of Sandwich Composites with Additively Manufactured Triply Periodic Minimal Surface Cellular Structured Core,”

Journal of Sandwich Structures & Materials 24, no. 2 (February 2022): 1133–51, https://doi.org/10.1177/10996362211037012.

[48] Joon-Hyung Byun and Tsu-Wei Chou, 'Mechanics of Textile Composites', in Comprehensive Composite Materials (Elsevier, 2000), 719–61, https://doi.org/10.1016/B0-08-042993-9/00059-0.

[49] A.P. Mouritz, 'Three-Dimensional (3D) Fiber Reinforcements for Composites', in Composite Reinforcements for Optimum Performance (Elsevier, 2011), 159–97, https://doi.org/10.1016/B978-0-12-819005-0.00006-X.

[50] Kadir Bilisik et al., 'Three-Dimensional Fully Interlaced Woven Preforms for Composites', Textile Research Journal 83, no. 19 (November 2013): 2060–84, https://doi.org/10.1177/0040517513487791.

[51] B. Kumar and J. Hu, 'Woven Fabric Structures and Properties', in Engineering of High-Performance Textiles (Elsevier, 2018), 133–51, https://doi.org/10.1016/B978-0-08-101273-4.00004-4.

[52] C. Pastore and Y. Gowayed, 'Structure and Mechanics of 2D and 3D Textile Composites', in Structure and Mechanics of Textile Fibre Assemblies (Elsevier, 2008), 141–89, https://doi.org/10.1533/9781845695231.141.

[53] M. Linke et al., "Automating Textile Preforming Technology for Mass Production of Fibre-Reinforced Polymer (FRP) Composites," in The Global Textile and Clothing Industry (Elsevier, 2012), 171–95, https://doi.org/10.1533/9780857095626.171.

[54] Mohsen Attaran, “The Rise of 3-D Printing: The Advantages of Additive Manufacturing over Traditional Manufacturing,” Business Horizons 60, no. 5 (September 2017): 677–88, https://doi.org/10.1016/j.bushor.2017.05.011.

[55] Joanna Izdebska-Podsiadły, ‘Classification of 3D Printing Methods’, in Polymers for 3D Printing (Elsevier, 2022), 23–34, https://doi.org/10.1016/B978-0-12-818311-3.00009-4.

[56] F42 Committee, ‘Terminology for Additive Manufacturing Technologies’, (ASTM International), accessed 13 August 2022, https://doi.org/10.1520/F2792-12A.

[57] M. D. Monzón et al., ‘Standardization in Additive Manufacturing: Activities Carried out by International Organizations and Projects’, The International Journal of Advanced Manufacturing Technology 76, no. 5–8 (February 2015): 1111–21, https://doi.org/10.1007/s00170-014-6334-1.

[58] S. Anand Kumar and R.V.S. Prasad, ‘Basic Principles of Additive Manufacturing: Different Additive Manufacturing Technologies’, in Additive Manufacturing (Elsevier, 2021), 17–35, https://doi.org/10.1016/B978-0-12-822056-6.00012-6.

[59] Kaufui V. Wong and Aldo Hernandez, ‘A Review of Additive Manufacturing’, ISRN Mechanical Engineering 2012 (16 August 2012): 1–10, https://doi.org/10.5402/2012/208760.

[60] Joel C. Najmon, Sajjad Raeisi, and Andres Tovar, ‘Review of Additive Manufacturing Technologies and Applications in the Aerospace Industry’, in Additive Manufacturing for the Aerospace Industry (Elsevier, 2019), 7–31, https://doi.org/10.1016/B978-0-12-814062-8.00002-9.

[61] Jorge Lino Alves, Leonardo Santana, and Edwin M. Ocaña Garzón, 'Binder Jetting', in Polymers for 3D Printing (Elsevier, 2022), 113–25, https://doi.org/10.1016/B978-0-12-818311-3.00010-0.

[62] Chandrika Pal and Anand Krishnamoorthy, 'Direct Energy Deposition', in Polymers for 3D Printing (Elsevier, 2022), 137–42, https://doi.org/10.1016/B978-0-12-818311-3.00004-5.

[63] S.L. Sing et al., '3D Printing of Metals in Rapid Prototyping of Biomaterials: Techniques in Additive Manufacturing', in Rapid Prototyping of Biomaterials (Elsevier, 2020), 17–40, https://doi.org/10.1016/B978-0-08-102663-2.00002-2.

[64] Maciej Cader and Wojciech Kiński, 'Material Extrusion', in Polymers for 3D Printing (Elsevier, 2022), 75–89, https://doi.org/10.1016/B978-0-12-818311-3.00015-X.

[65] Yu-an Jin et al., 'Quantitative Analysis of Surface Profile in Fused Deposition Modelling', Additive Manufacturing 8 (October 2015): 142–48, https://doi.org/10.1016/j.addma.2015.10.001.

[66] Katarzyna Piłczyńska, 'Material Jetting', in Polymers for 3D Printing (Elsevier, 2022), 91–103, https://doi.org/10.1016/B978-0-12-818311-3.00022-7.

[67] S.L. Sing et al., '3D Printing of Metals in Rapid Prototyping of Biomaterials: Techniques in Additive Manufacturing', in Rapid Prototyping of Biomaterials (Elsevier, 2020), 17–40, https://doi.org/10.1016/B978-0-08-102663-2.00002-2.

[68] Dominik Wyszynski and Marcin Grabowski, 'Powder Bed Fusion', in Polymers for 3D Printing (Elsevier, 2022), 105–12, https://doi.org/10.1016/B978-0-12-818311-3.00001-X.

[69] Ana Pilipović, ‘Sheet Lamination’, in Polymers for 3D Printing (Elsevier, 2022), 127–36, https://doi.org/10.1016/B978-0-12-818311-3.00008-2;

[70] Gojko Vladić et al., ‘Vat Photopolymerization’, in Polymers for 3D Printing (Elsevier, 2022), 65–74, https://doi.org/10.1016/B978-0-12-818311-3.00018-5.

[71] Jia An, ‘Polymer Materials for Additive Manufacturing’, in Digital Manufacturing (Elsevier, 2022), 221–45, https://doi.org/10.1016/B978-0-323-95062-6.00011-5.

[72] Zefeng Xiao et al., ‘Evaluation of Topology-Optimized Lattice Structures Manufactured via Selective Laser Melting’, Materials & Design 143 (April 2018): 27–37, https://doi.org/10.1016/j.matdes.2018.01.023.

[73] M. Heidari-Rarani, M. Rafiee-Afarani, and A.M. Zahedi, “Mechanical Characterization of FDM 3D Printing of Continuous Carbon Fiber Reinforced PLA Composites,” Composites Part B: Engineering 175 (October 2019): 107147, https://doi.org/10.1016/j.compositesb.2019.107147.

[74] Ben Wang et al., “Fabrication of Triangular Corrugated Structure Using 3D Printed Continuous Carbon Fiber-Reinforced Thermosetting Epoxy Composites,” Polymer Testing 106 (February 2022): 107469, https://doi.org/10.1016/j.polymertesting.2021.107469.

[75] Piergiorgio Valentino et al., “Mechanical Characterization of Basalt Woven Fabric Composites: Numerical and Experimental Investigation,” Frattura Ed Integrità Strutturale 8, no. 28 (March 31, 2014): 1–11, https://doi.org/10.3221/IGF-ESIS.28.01.

[76] Yong Xie et al., ‘Grain Boundary Discontinuity and Performance Improvement Mechanism of Wire Arc Additive Manufactured Ti–6Al–4V’, Journal of Alloys and Compounds 869 (July 2021): 159287, https://doi.org/10.1016/j.jallcom.2021.159287.

[77] Amir Mostafaei et al., ‘Defects and Anomalies in Powder Bed Fusion Metal Additive Manufacturing’, Current Opinion in Solid State and Materials Science 26, no. 2 (April 2022): 100974, https://doi.org/10.1016/j.cossms.2021.100974.

[78] Mehdi Hamid et al., ‘Modeling of Porosity and Grain Size Effects on Mechanical Behavior of Additively Manufactured Structures’, Additive Manufacturing 38 (February 2021): 101833, https://doi.org/10.1016/j.addma.2020.101833.

[79] Ben Wang et al., ‘Fabrication of Triangular Corrugated Structure Using 3D Printed Continuous Carbon Fiber-Reinforced Thermosetting Epoxy Composites’, Polymer Testing 106 (February 2022): 107469, https://doi.org/10.1016/j.polymertesting.2021.107469.

[80] Keqiang Zhang et al., ‘Quantitative Characterization of Defects in Stereolithographic Additive Manufactured Ceramic Using X-Ray Computed Tomography’, Journal of Materials Science & Technology 118 (August 2022): 144–57, https://doi.org/10.1016/j.jmst.2021.11.060.

[81] H. Montazerian et al., “A Frameless Picture Frame Test with Embedded Sensor: Mitigation of Imperfections in Shear Characterization of Woven Fabrics,” Composite Structures 211 (March 2019): 112–24, https://doi.org/10.1016/j.compstruct.2018.11.096.

[82] Mehdi Ghazimoradi et al., “Experimental Measurements and Numerical Modelling of the Mechanical Behaviour of a Glass Plain Weave Composite Reinforcement,” Journal

of Reinforced Plastics and Composites 39, no. 1–2 (January 2020): 45–59, https://doi.org/10.1177/0731684419868846.

[83] Qingsong Wei et al., "Numerical and Experimental Investigation on 3D Angle Interlock Woven Fabric under Ballistic Impact," Composite Structures 266 (June 2021): 113778, https://doi.org/10.1016/j.compstruct.2021.113778.

[84] Liuxiang Guan, Jialu Li, and Ya'nan Jiao, "The Influence of Yarn Fineness and Number of Yarn Layers on In-Plane Shear Properties of 3-D Woven Fabric," Advanced Composites Letters 29 (January 1, 2020): 2633366X1989792, https://doi.org/10.1177/2633366X19897921.

[85] Philip Harrison, Marcos Fernandez Alvarez, and Drew Anderson, "Towards Comprehensive Characterisation and Modelling of the Forming and Wrinkling Mechanics of Engineering Fabrics," *International Journal of Solids and Structures* 154 (December 2018): 2–18, https://doi.org/10.1016/j.ijsolstr.2016.11.008.

[86] Shohreh Minapoor, Saeed Ajeli, and Mahdi Salmani Tehrani, "Investigation into Tensile Strength of Noncrimp Three-Dimensional Orthogonal Woven Structure," Journal of Industrial Textiles 49, no. 2 (August 2019): 200–218, https://doi.org/10.1177/1528083718775980.

[87] Mehmet Korkmaz et al., "Investigation of the Mechanical and Forming Behaviour of 3D Warp Interlock Carbon Woven Fabrics for Complex Shape of Composite Material," Journal of Industrial Textiles, January 11, 2021, 152808372098410, https://doi.org/10.1177/1528083720984100.

[88] Chan Hui, Peng Wang, and Xavier Legrand, "Improvement of Tufting Mechanism during the Advanced 3-Dimensional Tufted Composites Manufacturing: To the

Optimisation of Tufting Threads Degradation," Composite Structures 220 (July 2019): 423–30, https://doi.org/10.1016/j.compstruct.2019.04.019.

[89] J.C. de Kruijk, "Automated composite manufacturing using robotics lowers cost, lead-time and scrap rate," Amsterdam: Netherlands Aerospace Centre; April 2018. Tech. Rep. NLR-TP-2018-143. [Google Scholar]

[90] John Summerscales, "Resin Infusion Under Flexible Tooling (RIFT)," in Wiley Encyclopedia of Composites, by Luigi Nicolais (Hoboken, NJ, USA: John Wiley & Sons, Inc., 2012), weoc216, https://doi.org/10.1002/9781118097298.weoc216.

[91] Spiridon Konstantopoulos et al., "Liquid Composite Molding Reproducibility in Real-World Production of Fiber Reinforced Polymeric Composites: A Review of Challenges and Solutions," Advanced Manufacturing: Polymer & Composites Science 5, no. 3 (July 3, 2019): 85–99, https://doi.org/10.1080/20550340.2019.1635778.

[92] Jaime Juan et al., "Design of a Prototype for the In Situ Forming of a Liquid-Infused Preform Process," Journal of Mechanical Design 142, no. 1 (January 1, 2020): 015001, https://doi.org/10.1115/1.4044107.

[93] Ricarda Riedel et al., "Managing Knowledge and Parameter Dependencies with MBSE in Textile Product Development Processes," Procedia CIRP 91 (2020): 170–75, https://doi.org/10.1016/j.procir.2020.01.138.

[94] Milad Saeedifar and Dimitrios Zarouchas, "Damage Characterization of Laminated Composites Using Acoustic Emission: A Review," Composites Part B: Engineering 195 (August 2020): 108039, https://doi.org/10.1016/j.compositesb.2020.108039.

[95] Jiangtao Wang et al., “Compression Performances and Failure Maps of Sandwich Cylinders with Pyramidal Truss Cores Obtained through Geometric Mapping and Snap-Fit Method,” Composite Structures 226 (October 2019): 111212, https://doi.org/10.1016/j.compstruct.2019.111212.

[96] J. Xiong et al., “Bending Behavior of Lightweight Sandwich-Walled Shells with Pyramidal Truss Cores,” Composite Structures 116 (September 2014): 793–804, https://doi.org/10.1016/j.compstruct.2014.06.006.

[97] Qianqian Wu et al., “A Novel Strengthening Method for Carbon Fiber Composite Lattice Truss Structures,” Composite Structures 153 (October 2016): 585–92, https://doi.org/10.1016/j.compstruct.2016.06.060.

[98] Christopher J. Hunt, Michael R. Wisnom, and Benjamin K.S. Woods, “WrapToR Composite Truss Structures: Improved Process and Structural Efficiency,” Composite Structures 230 (December 2019): 111467, https://doi.org/10.1016/j.compstruct.2019.111467.

[99] Christopher J. Hunt et al., “WrapToR Composite Truss Structures: Measurement and Modelling of Mechanical Response,” Composite Structures 254 (December 2020): 112834, https://doi.org/10.1016/j.compstruct.2020.112834.

[100] Sha Yin, Linzhi Wu, and Steven Nutt, “Stretch–Bend-Hybrid Hierarchical Composite Pyramidal Lattice Cores,” Composite Structures 98 (April 2013): 153–59, https://doi.org/10.1016/j.compstruct.2012.11.004.

[101] Zheng Shi et al., “Structural Analysis of Composite Sandwich Plates with Enhanced Pyramid Lattice Core Using VAM-Based Reduced-Order Equivalent Model,”

Composite Structures 290 (June 2022): 115480, https://doi.org/10.1016/j.compstruct.2022.115480.

[102] Jiakang Gan, E Ji, and Bing Li, “Investigation on Impact Resistance of Hierarchical Lightweight Lattice Structure,” Journal of Physics: Conference Series 2252, no. 1 (April 1, 2022): 012028, https://doi.org/10.1088/1742-6596/2252/1/012028.

[103] Xiaodong Li et al., “Effect of Temperature on the Compressive Behavior of Carbon Fiber Composite Pyramidal Truss Cores Sandwich Panels with Reinforced Frames,” Theoretical and Applied Mechanics Letters 6, no. 2 (March 2016): 76–80, https://doi.org/10.1016/j.taml.2016.02.002.

[104] Tidong Zhao et al., “Review of Carbon Fiber-Reinforced Sandwich Structures,” Polymers and Polymer Composites 30 (January 2022): 096739112210987, https://doi.org/10.1177/09673911221098729.

[105] L. Sorrentino et al., “Manufacture of High Performance Isogrid Structure by Robotic Filament Winding,” Composite Structures 164 (March 2017): 43–50, https://doi.org/10.1016/j.compstruct.2016.12.061.

[106] Shu Jiang et al., “Interlocking Orthogrid: An Efficient Way to Construct Lightweight Lattice-Core Sandwich Composite Structure,” Composite Structures 176 (September 2017): 55–71, https://doi.org/10.1016/j.compstruct.2017.05.029.

[107] Thomas Jared Weaver and David W. Jensen, “Mechanical Characterization of a Graphite/Epoxy IsoTruss,” Journal of Aerospace Engineering 13, no. 1 (January 2000): 23–35, https://doi.org/10.1061/(ASCE)0893-1321(2000)13:1(23).

[108] Benjamin K.S. Woods, Ioan Hill, and Michael I. Friswell, “Ultra-Efficient Wound Composite Truss Structures,” Composites Part A: Applied Science and Manufacturing 90 (November 2016): 111–24, https://doi.org/10.1016/j.compositesa.2016.06.022.

[109] Qianqian Sui, Changliang Lai, and Hualin Fan, “Buckling Failure Modes of One-Dimensional Lattice Truss Composite Structures,” Proceedings of the Institution of Mechanical Engineers, Part G: Journal of Aerospace Engineering 232, no. 13 (October 2018): 2565–83, https://doi.org/10.1177/0954410017716194.

[110] Austin Gurley et al., “The Design of Optimal Lattice Structures Manufactured by Maypole Braiding,” Journal of Mechanical Design 137, no. 10 (October 1, 2015): 101401, https://doi.org/10.1115/1.4031122.

[111] Ju et al., “Flexural Properties of Lightweight FRP Composite Truss Structures,” Journal of Composite Materials 45, no. 19 (September 2011): 1921–30, https://doi.org/10.1177/0021998311410237.

[112] Ju et al., “Multi-Parameter Optimization of Lightweight Composite Triangular Truss Structure Based on Response Surface Methodology,” Composite Structures 97 (March 2013): 107–16, https://doi.org/10.1016/j.compstruct.2012.10.025.

[113] Richard G. Brereton, “Optimisation: Steepest Ascent, Steepest Descent and Gradient Methods,” in Comprehensive Chemometrics (Elsevier, 2020), 573–83, https://doi.org/10.1016/B978-0-12-409547-2.14835-8.

[114] E.J.HEARNPh.D., B.Sc. (Eng.) Hons., C.Eng., F.I.Mech.E., F.I.Prod.E., F.I.Diag.E., “An Introduction to the Mechanics of Elastic and Plastic Deformation of Solids and Structural Materials,” 1997, Pages 254-296, https://doi.org/10.1016/B978-075063265-2/50012-8

[115] Changjun Chen et al., “Efficiently Finding the Minimum Free Energy Path from Steepest Descent Path,” The Journal of Chemical Physics 138, no. 16 (April 28, 2013): 164122, https://doi.org/10.1063/1.4799236.

[116] Jasbir S.Arora, "Introduction to Optimum Design (Second Edition)," 2004, Pages 191-258, https://doi.org/10.1016/B978-012064155-0/50006-9

[117] Jasbir S.Arora, "Introduction to Optimum Design (Second Edition)," 2004, Pages 305-337, https://doi.org/10.1016/B978-012064155-0/50009-4

[118] Andreas Endruweit et al., “Influence of Stochastic Fibre Angle Variations on the Permeability of Bi-Directional Textile Fabrics,” Composites Part A: Applied Science and Manufacturing 37, no. 1 (January 2006): 122–32, https://doi.org/10.1016/j.compositesa.2005.04.014.

[119] Yue El-Hage, Simon Hind, and François Robitaille, “Thermal Conductivity of Textile Reinforcements for Composites,” Journal of Textiles and Fibrous Materials 1 (January 1, 2018): 251522111775115, https://doi.org/10.1177/2515221117751154.

[120] Saswat Kumar Samal et al., ‘3D-Printed Satellite Brackets: Materials, Manufacturing and Applications’, Crystals 12, no. 8 (15 August 2022): 1148, https://doi.org/10.3390/cryst12081148.

[121] “MicroScribe G2 with Rhino: a spatial measuring tool”, [online], available from http://www.remtek.com/remtek/microscribe_rhino.htm

[122] “WEST SYSTEM®: 207 Special Clear Hardener”, [online], available from https://www.westsystem.com/207-special-clear-hardener/

[123] “WEST SYSTEM®: 105/207 Technical Data Sheet”, [online], https://www.westsystem.com/wp-content/uploads/105-207-Epoxy-Resin-1.pdf

[124] “TENAX®-J: HTS40 E13 12K 800tex”, [online], https://www.swiss-composite.ch/pdf/t-Tenax-Datenblatt.pdf

Appendix

Appendix A. Measurement data for SA experimental validations

Table A.1. Measure data for SA verifications 1)5:2:2 grams unit:millimeter

Points No.		1	2	3	4	5	6	*a*	*b*	*SAC_a*	*SAC_b*
Measure 1	*X*	310.4	68.0	6.9	289.3	39.3	-35.1	191.0	40.1	202.0	42.6
	Y	85.0	-8.3	313.5	288.9	-12.0	268.6	92.1	186.6	85.7	184.7
	Z	-116.8	-84.2	-183.5	-88.2	-157.5	-55.2	-106.6	-128.0	-104.3	-121.9
Measure 2	*X*	297.8	64.5	-22.8	267.9	31.6	-54.6	178.1	27.6	189.3	24.1
	Y	107.9	1.5	317.5	310.8	-6.2	266.7	111.0	192.3	101.5	190.1
	Z	-131.2	-91.1	-175.2	-92.3	-159.4	-47.2	-115.9	-126.2	-113.3	-119.3
Measure 3	*X*	320.7	69.9	45.2	322.7	42.3	-7.4	204.2	67.4	211.5	64.8
	Y	59.9	-7.9	320.7	263.8	-6.5	271.5	69.7	189.9	70.9	184.4
	Z	-103.9	-85.3	-163.6	-56.3	-157.0	-38.6	-97.5	-112.9	-94.1	-109.1
Average	*X*	309.6	67.5	9.8	293.3	37.7	-32.4	191.1	45.1	200.8	43.9
	Y	84.2	-4.9	317.2	287.8	-8.2	268.9	90.9	189.6	86.0	186.4
	Z	-117.3	-86.9	-174.1	-78.9	-158.0	-47.0	-106.7	-122.4	-103.9	-116.8

Table A.2. Measure data for SA verifications 2)5:5:2 grams unit:millimeter

Points No.		1	2	3	4	5	6	*a*	*b*	*SAC_a*	*SAC_b*
Measure 1	*X*	305.3	68.5	-0.5	285.7	37.3	-40.3	182.2	63.4	186.3	60.7
	Y	92.8	-2.1	316.6	296.0	-10.1	267.7	161.1	238.3	158.4	228.6
	Z	-126.2	-89.7	-177.7	-87.4	-160.7	-49.5	-113.4	-138.9	-112.4	-135.6
Measure 2	*X*	297.0	67.1	-27.7	260.1	38.4	-61.6	178.3	45.2	172.7	40.1
	Y	119.2	3.6	314.6	318.0	-4.8s	265.2	168.8	239.3	174.2	233.9
	Z	-125.1	-89.6	-177.9	-87.2	-161.4	-51.2	-113.6	-132.6	-111.5	-135.8
Measure 3	*X*	308.2	68.4	6.4	291.0	37.0	-37.4	187.9	67.9	189.8	65.1
	Y	88.2	-3.8	314.7	291.1	-11.0	267.1	149.7	236.1	155.1	226.6
	Z	-121.2	-88.4	-181.3	-84.2	-161.6	-52.2	-111.1	-141.1	-110.4	-137.1
Average	*X*	303.5	68.0	-7.3	278.9	37.6	-46.4	182.8	58.8	183.0	55.3
	Y	100.1	-0.8	315.3	301.7	-8.6	266.7	159.9	237.9	162.6	229.7
	Z	-124.2	-89.2	-179.0	-86.2	-161.2	-50.9	-112.7	-137.5	-111.7	-136.2

Appendix B. Load-displacement curves for bars in prototypes 2.1, 2.2

bar 3

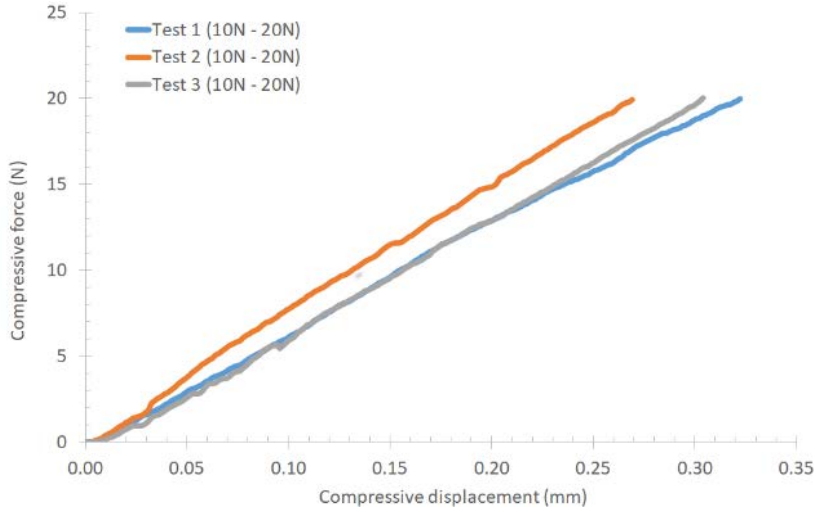

bar 4

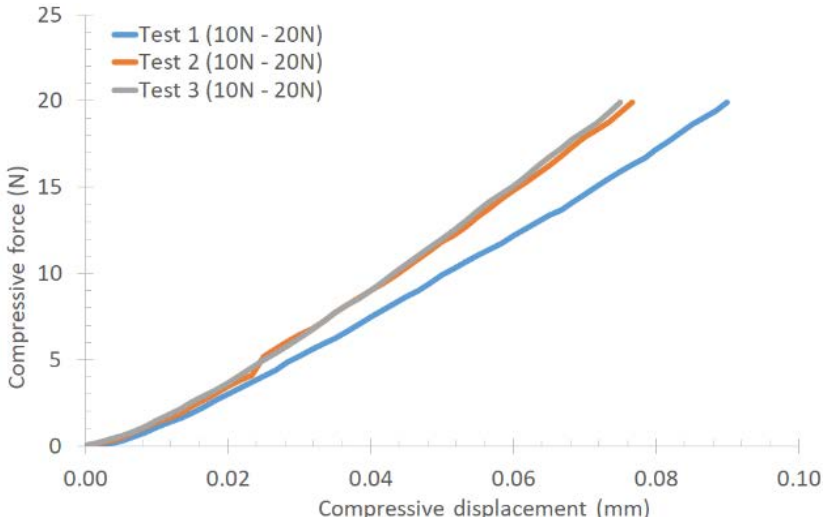

bar 5

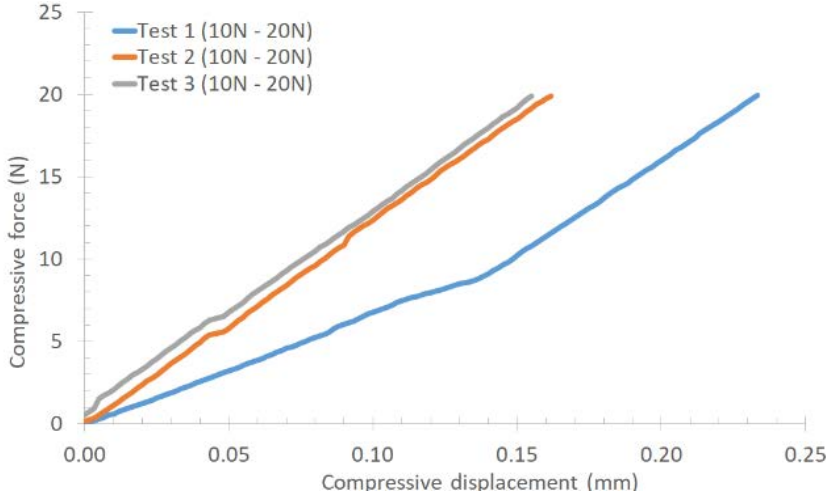

bar 6

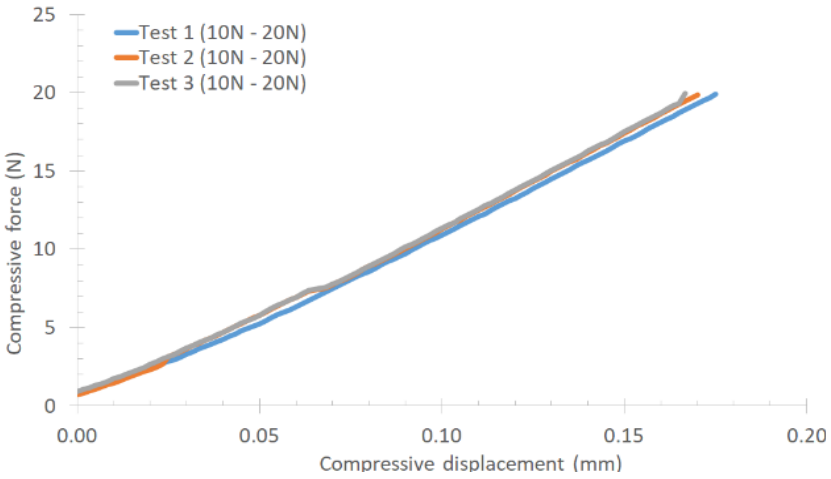

bar 7

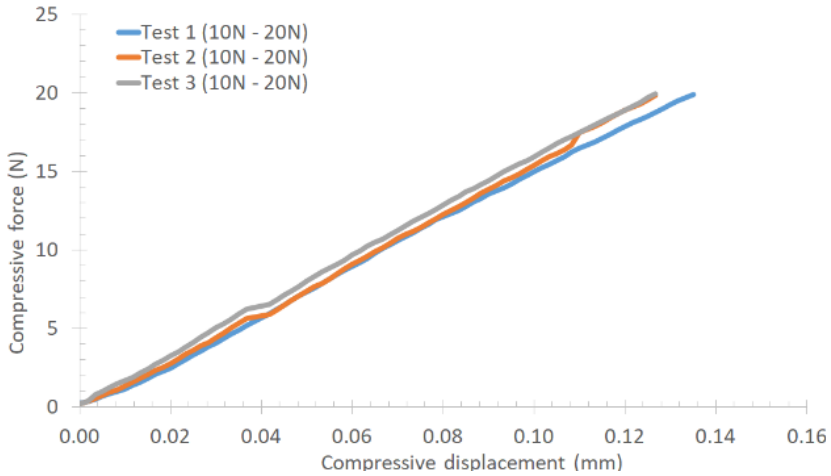

bar 8

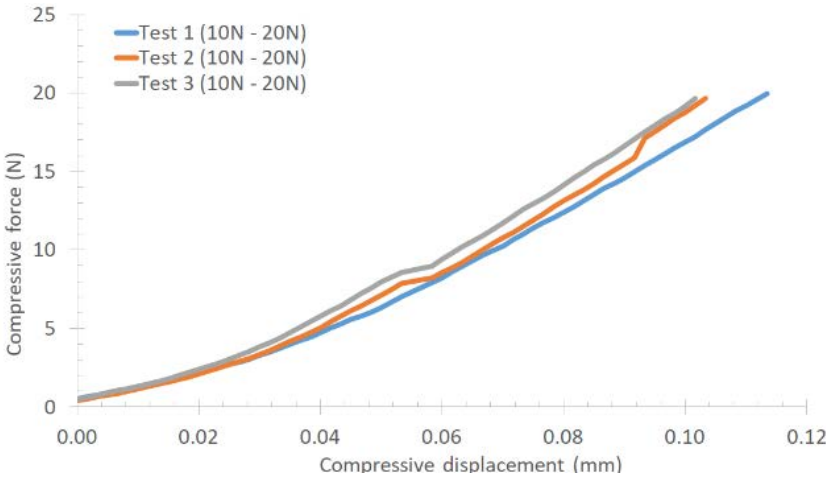

Figure B.1. Load-displacement curves processed for bars 3-8 in post-optimized prototype 2.2

bar 1

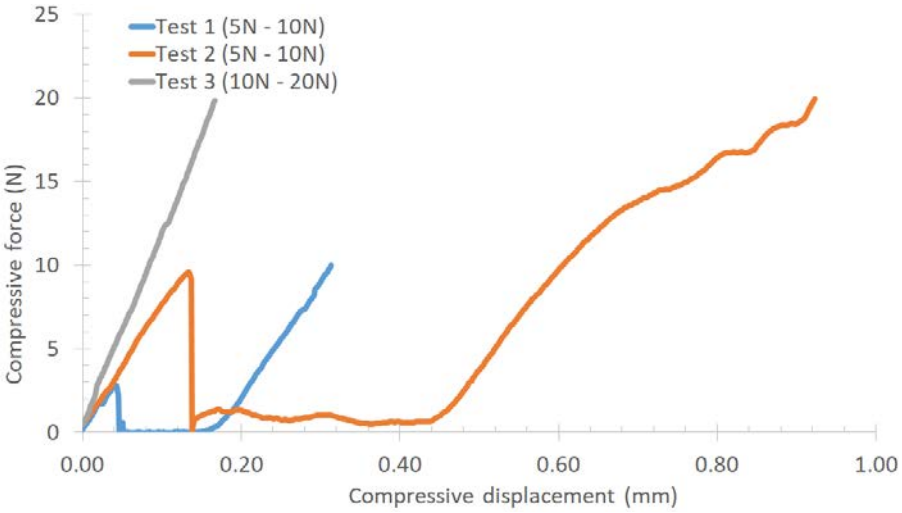

bar 2

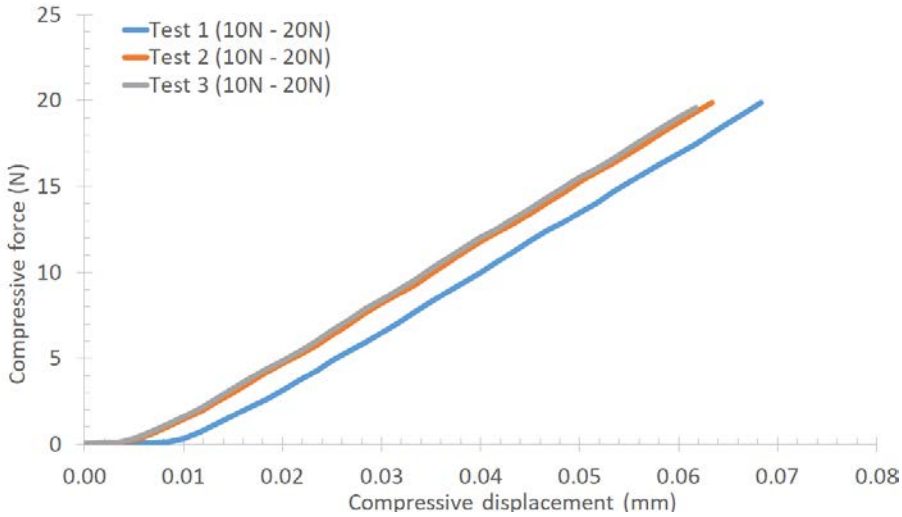

bar 3

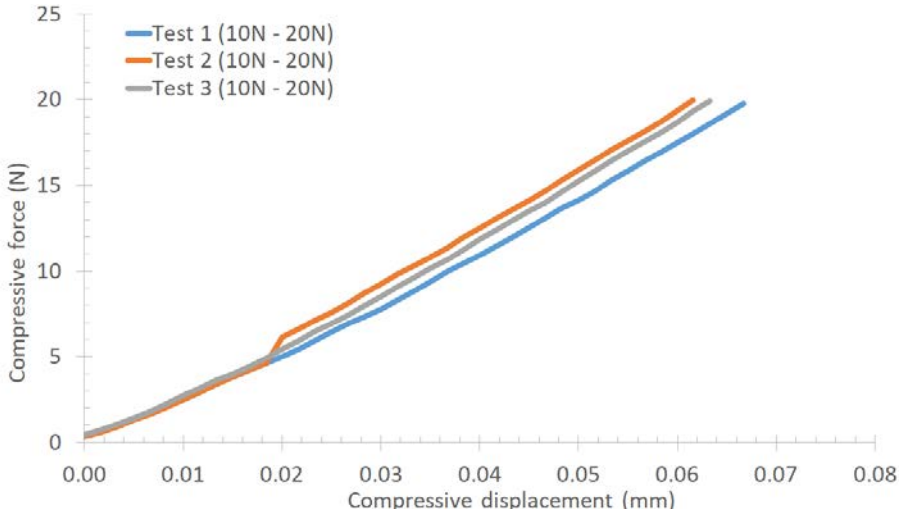

bar 4

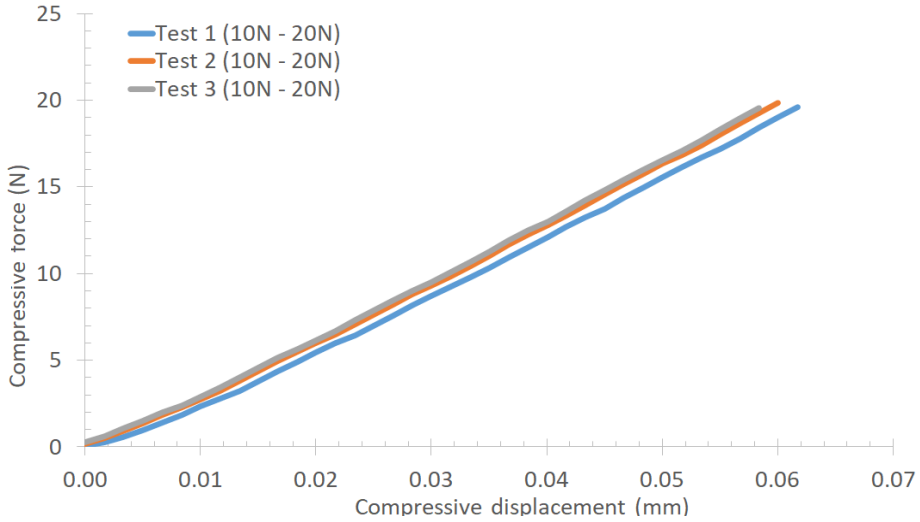

bar 5

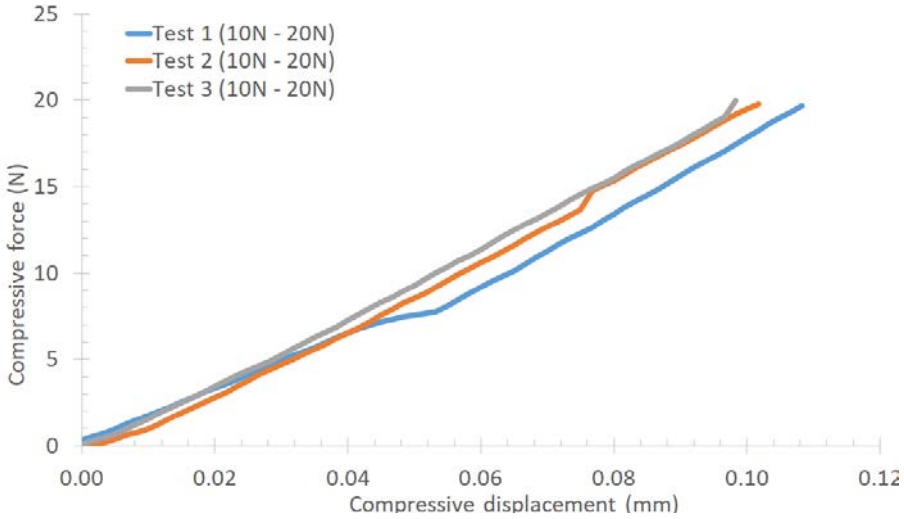

bar 6

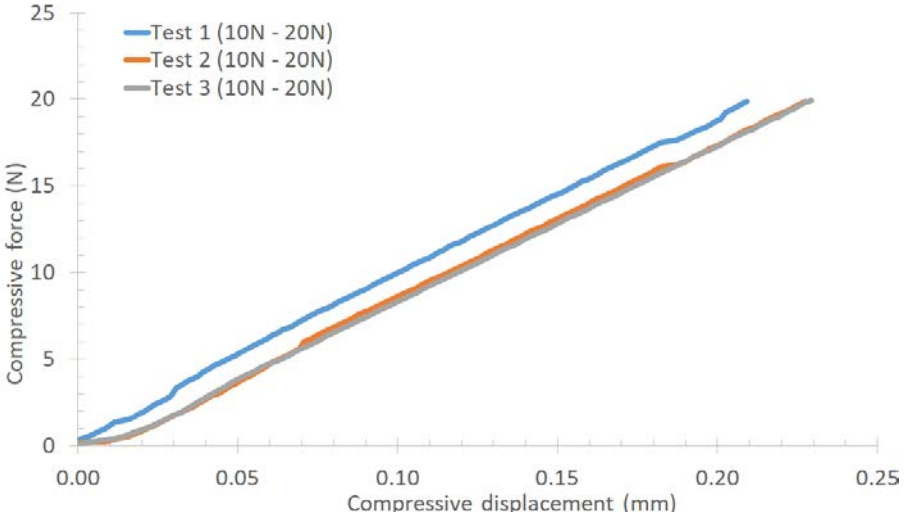

bar 7

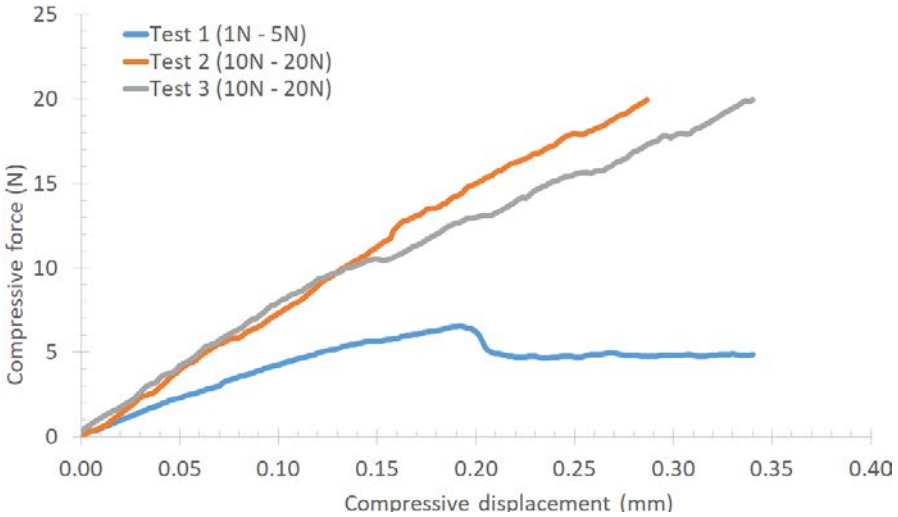

bar 8

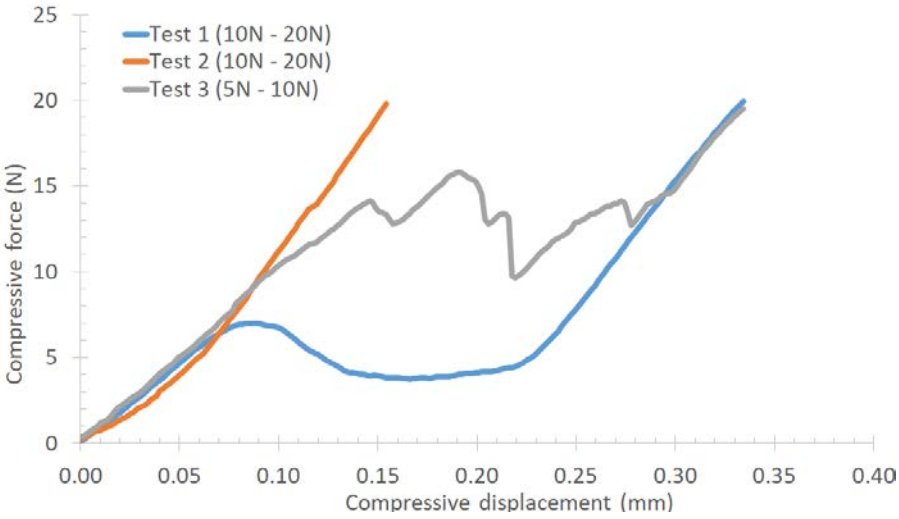

bar 9

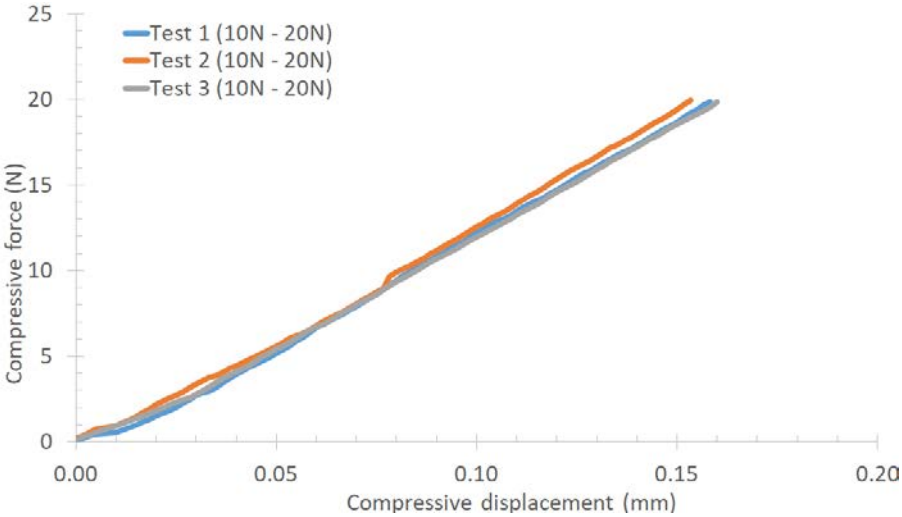

bar 10

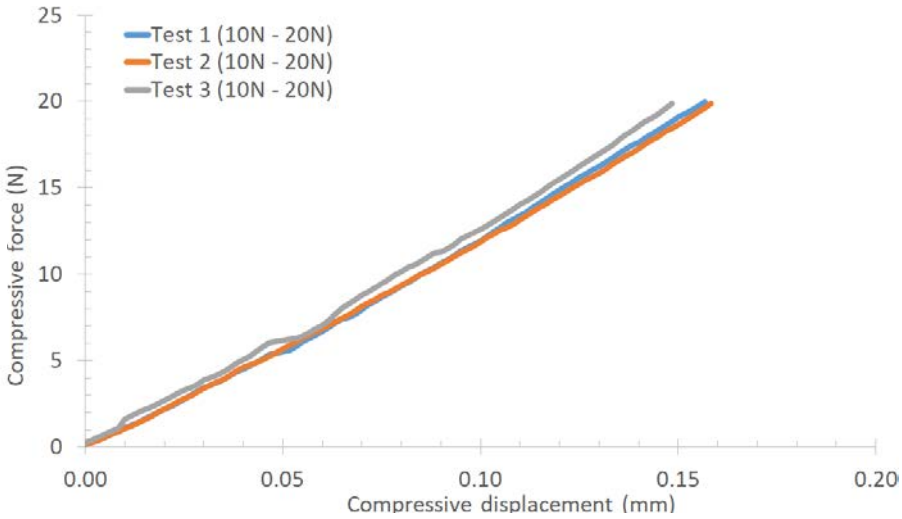

bar 11

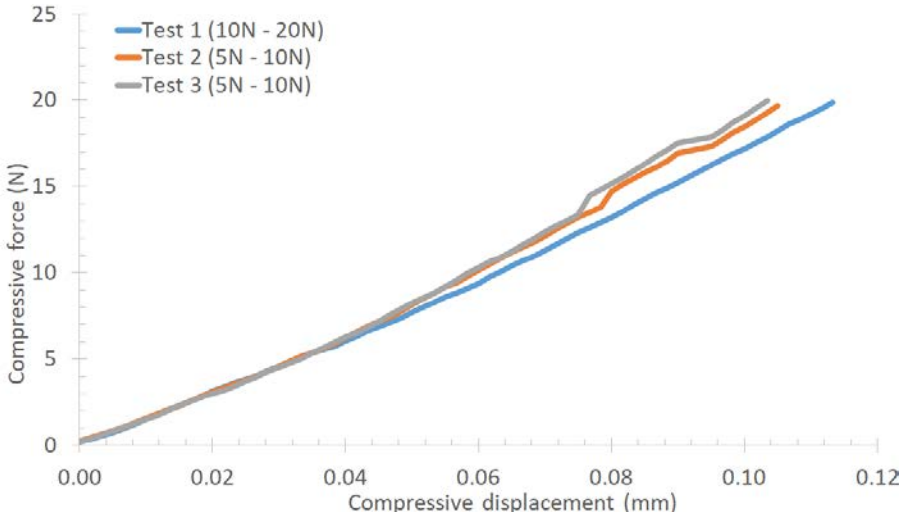

bar 12

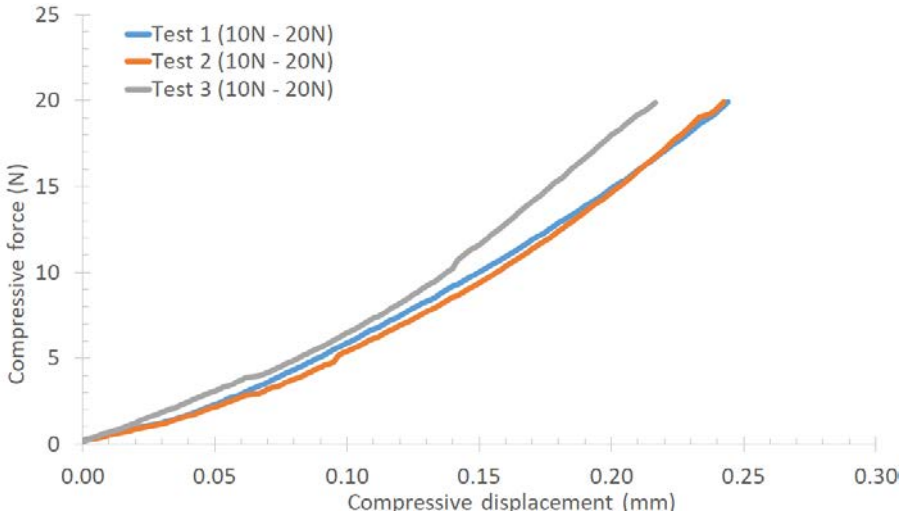

Figure B.2. Load-displacement curves processed for bars 1-12 in non-optimized prototype 2.1